Urban Climate at Street Scale

Analysis and Adaptation

Schrijvers, P.J.C.

DOI
10.4233/uuid:6d00bdc4-f985-4b3a-9238-38be68cb3f2f

Publication date
2020

Document Version
Final published version

Citation (APA)
Schrijvers, P. J. C. (2020). *Urban Climate at Street Scale: Analysis and Adaptation*. [Dissertation (TU Delft), Delft University of Technology]. https://doi.org/10.4233/uuid:6d00bdc4-f985-4b3a-9238-38be68cb3f2f

URBAN CLIMATE AT STREET SCALE: ANALYSIS AND ADAPTATION

Proefschrift

ter verkrijging van de graad van doctor
aan de Technische Universiteit Delft,
op gezag van de Rector Magnificus prof.dr.ir. T.H.J.J. van der Hagen,
voorzitter van het College voor Promoties,
in het openbaar te verdedigen op vrijdag, 2 oktober 2020 om 12:30 uur

door

Patricius Johannes Cornelis SCHRIJVERS

Ingenieur in de werktuigbouwkunde, Technische Universiteit Delft,
Nederland
geboren te Buren

Dit proefschrift is goedgekeurd door de promotor:
Prof. dr. H.J.J. Jonker

Samenstelling promotiecommissie betaat uit:

Rector Magnificus,	voorzitter
Prof. dr. H.J.J. Jonker,	Technische Universiteit Delft, promotor
Prof. dr. ing. S. Kenjereš,	Technische Universiteit Delft, promotor
Dr. S.R. de Roode,	Technische Universiteit Delft, co-promotor
onafhankelijke leden:	
Dr. ir. M. van Reeuwijk,	Imperial college
Prof. dr. J. Vila-Guerau de Arellano,	Wageningen Universiteit
Prof. dr. ir. H.W.J. Russchenberg,	Technische Universiteit Delft
Prof. dr. ir. B.J.H van de Wiel,	Technische Universiteit Delft

ISBN: 978-94-6332-656-8
Ontwerp omslag: Liselotte van Zaanen
Drukwerk: GVO drukkers & vormgevers BV, Ede, the Netherlands

Contents

Summary **vi**

1 Introduction **1**
1.1 Introducing the problem 1
1.2 The Dutch Climate Proof Cities research program 3
1.3 The urban street canyon 5
1.4 Numerical modelling 8
1.5 Research questions 9
1.6 Outline 14

2 Breakdown of the night time urban heat island energy budget **17**
2.1 Introduction 18
2.2 Methods and case set-up 19
2.3 Results 30
2.4 Model assumptions 41
2.5 Corrigendum to the original submission 43
2.6 Conclusions 46
2.7 Acknowledgment 47

3 On the daytime micro-climatic conditions inside an idealized 2D urban canyon **49**
3.1 Introduction 50
3.2 Methods and case set-up 53
3.3 Results 62
3.4 Discussion 75
3.5 Conclusions 78
3.6 Acknowledgment 79

4 The effect of using a high-albedo material on the Universal Temperature Climate Index within a street canyon **81**

4.1 Introduction 81
4.2 Methodology and used data 84
4.3 Uniform canyon properties 90
4.4 Sensitivity studies 99
4.5 Discussion 105
4.6 Conclusions 107
4.7 Acknowledgement 108

5 Comparing a large-scale urban parametrisation scheme and micro-scale model 109
5.1 Introduction 109
5.2 Radiative transfer 112
5.3 Canyon wind speed 119
5.4 Sensible heat flux 121
5.5 Concluding remarks and future work 128

6 Concluding remarks and future work 131
6.1 Concluding remarks 131
6.2 Future work 133

Acknowledgements 149

About the author 151

List of journal publications 154

Summary

Urban climate at street scale: Analysis and adaptation

It is well known that the urban environment changes local climate inside the city. This change of the local climate manifests itself mainly through differences in air temperature, where cities remain warmer than the rural environment during the night. This phenomenon is called the Urban Heat Island (UHI) effect, and is defined as difference in air temperature between the urban and rural environment. The UHI effect is found in many cities of different sizes around the world, and ranges between 1 and 10°C during the night. The combination of the increasing urbanisation, global warming and the impact of increasing temperature on human health makes the urban heat island a topic that is gaining more and more attention.

This thesis focusses on the urban micro-climate, which treats indivicual buildings and their direct surroundings. A numerical modelling approach is used in this thesis, such that the local urban climate can be investigated and perturbed in a systematic way. The developed 2D model, called URBSIM, combines computation of radiative transfer by a Monte-Carlo model, conduction of energy into the urban material and a Computational Fluid Dynamics (CFD) model to compute air flow and air temperature.

With this model, it is shown that the main source of energy to the urban heat budget is due to radiative transfer. During the night, the long wave trapping effect (defined in this theses as radiation emitted by one surface and absorbed by an other) and absorbed long wave radiation emitted from the sky are of the same order of magnitude for a building height (H) over street width (W) ratio of H/W=0.5. With increasing building height, longwave trapping becomes the main source of energy to the urban energy budget.

During the day time, absorbed shortwave radiation is the main source of energy, followed by the long wave trapping effect. The relative contribution of these radiative components is decreasing with increasing building height,

and the conductive heat flux becomes more important.

The large impact of radiation sparked the question which high albedo adaptation measure (white surfaces) is best suited to reduce the Urban Heat Island effect. This thesis shows that there is a clear distinction between the atmospheric UHI (air temperature) and pedestrian heat stress. Lower air temperatures can be achieved by using high albedo materials, whereas thermal comfort at street level can be improved by using low albedo materials. By using a low albedo material, less radiation is reflected back inside the canyon, thereby reducing the mean radiant temperature. The lowest pedestrian heat stress is found by using a vertical albedo gradient from high albedo at the bottom part to a low albedo at the top part of the wall for H/W=1.0. This study indicated that using a high albedo material can decrease the UHI effect, but increases pedestrian heat stress, which might not be the desired effect.

The developed micro-scale model is also compared to a large-scale urban parametrisation scheme that is used in meso-scale models. In this parametrisation, a 2D geometry is used to compute the fluxes of the 3D environment. Results indicate that radiative transfer is well captured in the parametrisation. Canyon wind speeds and the sensible heat flux showed much larger differences between the two models, which is most likely due to the 2D geometry that is used as a basis for the parametrisation. It is very likely that these parametrisations are adapted to better represent the 3D urban environment.

The result of this thesis is an advanced numerical model that includes most processes relevant to the urban environment. Despite the fact that the model is limited to 2D cases, the studies presented in this thesis have aided the understanding of the elementary processes that control urban air temperature, the feedback processes and interactions between the different mechanisms in the urban surface energy balance.

Chapter 1

Introduction

Hot town, summer in the city
Back of my neck getting dirty and pritty
Been down, isn't it a pity
Doesn't seem to be a shadow in the city

All around people looking half dead
Walking on the side walk, hotter than a match head

But at night it's a different world
Go out and find a girl
Come-on come-on and dance all night
Despite the heat it'll be all right

Lyrics from: The Loving Spoonful - Summer In The City (1966)

1.1 Introducing the problem

About half of the world's population lived in urban areas in 2005 and this number is projected to increase further to 60% in 2030 (Golden, 2004) and 70% in 2050 (World Health Organisation, 2014). Over the same time period, global warming is expected to result in at least a 2°C rise in air temperature in 2050 compared to current day climate (IPCC, 2013). The temperature increase caused by climate change has a pressing effect in densely populated urbanized areas. It is well known that the urban environment changes the local climate inside the city (Arnfield, 2003). This change of the local climate manifests itself mainly through differences in air temperature, where cities remain warmer than the rural environment during the night. This phenomenon is called the Urban Heat Island (UHI) effect, and is defined as

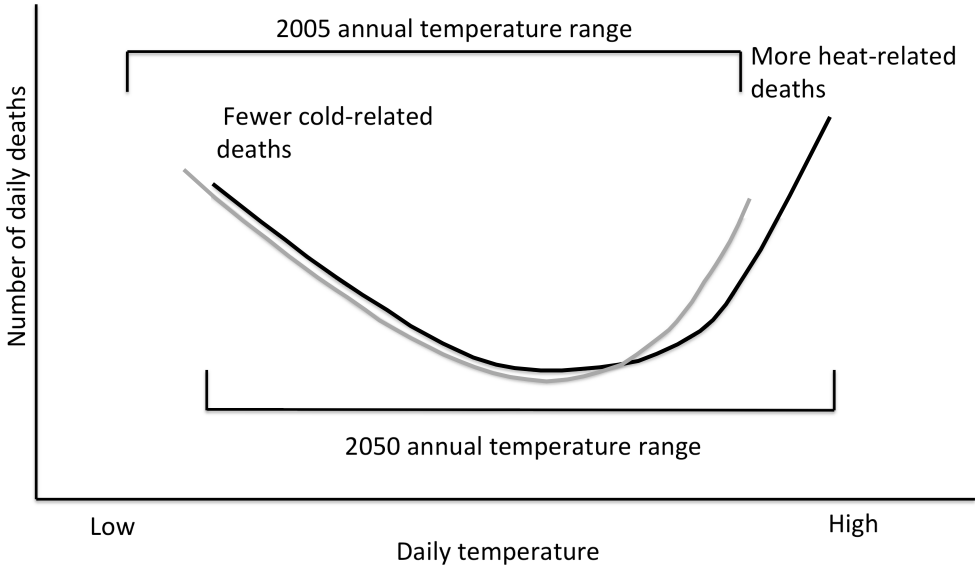

Fig. 1.1: Schematic picture of the number of daily deaths as a function of daily temperature for current climate (gray line) and future warmer climate (black line). Figure adapted from McMichael et al. (2006).

the difference in air temperature between the urban and rural environment. The first report on the UHI dates back to the time of Luke Howard, who documented the effect of London already in 1833 (Howard, 1833). Since then, this finding has been confirmed by many other studies, indicating a nighttime UHI effect between 1°C and 10°C in cities of different size around the world (Oke, 1981; Klysik and Fortuniak, 1999; Kim and Baik, 2004; Grimmond, 2007; Steeneveld et al., 2011; Theeuwes et al., 2014).

The increase in urban air temperature during the night compared to the rural area has a large impact on human health during extreme temperature events (heat waves). Several studies (Whitman et al., 1997; Vandentorren et al., 2001; Baccini et al., 2008) have reported a relation between ambient air temperature and the number of heat related deaths. A schematic figure of this temperature-mortality relation is shown in Fig. 1.1. Note that this is a simple schematic conveying the general idea. It shows the number of deaths as a function of temperature for the climate of 2005 (gray line) and the expected climate of 2050 (black line). The depicted relation varies greatly by latitude and climatic zone. In the Netherlands, the annual number of cold-related deaths exceed the number of heat-related deaths at the moment. However, each degree of air temperature increase will lead to an excess number of

deaths. In the future climate, there will be fewer cold-related deaths (top left corner), but the number of heat related deaths increases at a much higher rate (box in the top right corner). The numbers of excess deaths due to heat are significant: estimates indicate that an additional 70,000 people died in the European heat wave of 2003 (Robine et al., 2008).

In addition to the changes of the local climatic conditions inside the city, the urban environment also influences the urban boundary layer (Barlow et al., 2015), the surrounding rural environment due to (for instance) the urban plume (Masson, 2006) and can change the precipitation in the wake of a city (Baik et al., 2001). With the tendency to run weather forecast models at increasingly finer horizontal resolution, the urban environment cannot be neglected in these models. This forces large-scale weather forecast models to take the urban characteristics into account, and its net effect on the exchange of heat, temperature and momentum between the surface and atmosphere.

An overview of the different urban scales, and the link between them, is shown in Fig. 1.2. On the top, the meso-scale is shown, which includes the urban boundary layer and the urban plume. When taking a close-up (bottom left), the local scale is observed, which typically includes small towns or neighbourhoods. The focus of this thesis is the urban micro-scale, which is depicted on the bottom right of Fig. 1.2. This regime includes the effect of individual buildings on the air flow.

The combination of the increasing urbanisation, global warming and the impact of increasing temperature on human health makes the urban heat island a topic that is gaining more attention. Especially when it is considered that adapting the urban environment is a slow process, with time-scales in the order of decades. This is partly due to the slow decision making process (governance) and partly due to the long planning and construction times.

1.2 The Dutch Climate Proof Cities research program

One of the first studies on the UHI effect in a Dutch city has been conducted by Conrads (1975). From measurements in the city of Utrecht, it was found that the summer nighttime air temperature was (on average) 2.7°C warmer than the rural environment, with local peak values of 8°C. The city of Rotterdam has been studied by Roodenburg (1983), where similar temperature differences were found between the urban and rural environment.

Since then, the number of studies regarding air temperature in Dutch cities remained limited. It was believed that the relative small city size in combination with the moderate climate would not lead to large problems

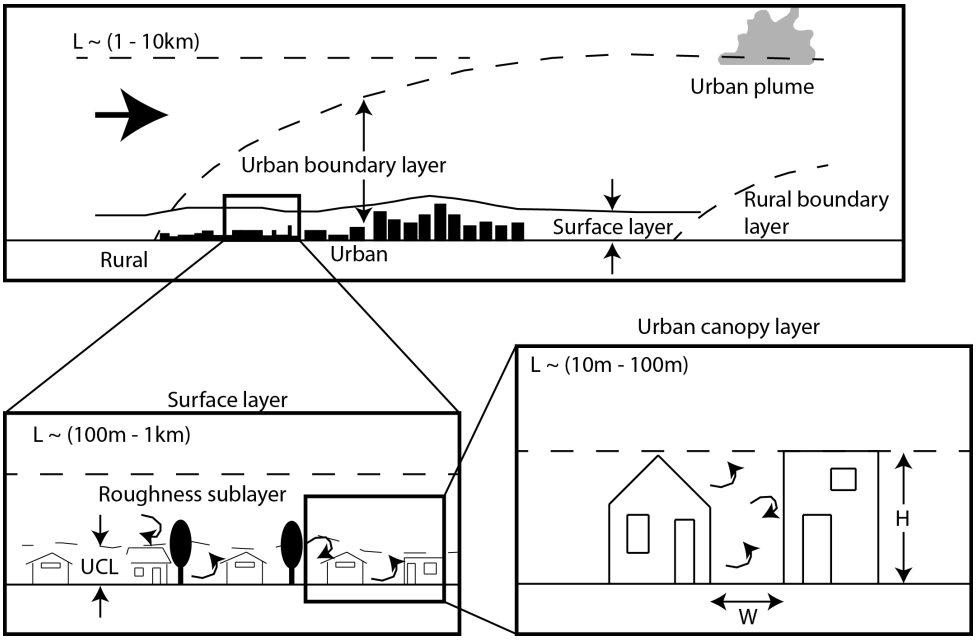

Fig. 1.2: Overview of the different urban scales

concerning human health. However, the heat waves that struck Europe in 2003 and 2006 led to an estimated excess number of heat related deaths between 1000 and 2200 in the Netherlands, a relatively high number when compared to other European countries (European Environment Agency, 2008). This sparked the question whether the UHI effect could be of importance in the Netherlands.

In 2004, the Dutch research consortium "Klimaat Voor Ruimte" ("Climate Changes Spatial Planning Program") started. The mission of the program was to introduce climate change and climate variability as one of the guiding principles for spatial planning in the Netherlands. Exploratory measurements were undertaken in the urban environment in this program, which confirmed the findings by Conrads and Roodenburg (Steeneveld et al., 2011). When the follow-up program "Kennis Voor Klimaat" (Knowledge For Climate) started in 2010, a program particularly dedicated to the urban environment was initiated: Climate Proof Cities. This PhD study has been conducted as a part of that research program.

The goal of the Climate Proof Cities consortium is to answer the following questions:

- What are the most important processes governing the urban climate in

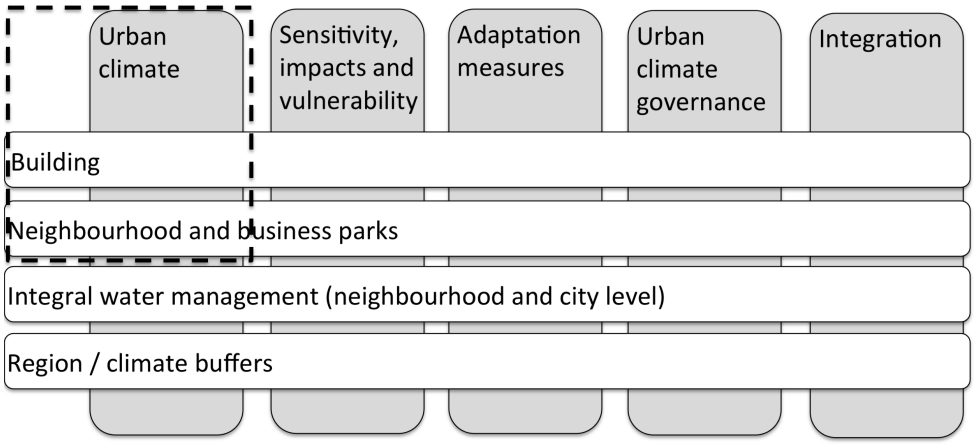

Fig. 1.3: Schematic overview of the Climate Proof Cities program. Vertical blocks are different work-packages, horizontal blocks are different scales that are studied. The subject of this thesis is located in the dashed block.

Dutch cities?

- How vulnerable are Dutch cities to the effects of climate change?
- Which measures can be taken in order to better adapt cities to a future climate?
- How can these measures be implemented in urban areas?
- What is the cost-benefit balance of the adaptation measures?

To answer these research questions, the consortium is split in different work-packages, which have their own field of research. The different work-packages are linked through the scale on which they act (see Fig. 1.3 for a schematic overview of the work-packages and scales).

This PhD-thesis is part of work-package 'Urban climate', in which the main focus is on understanding the local climate. The scale considered in this research is that of individual buildings and the urban street canyon (shown in the most top left of Fig. 1.3).

1.3 The urban street canyon

This thesis focusses on the urban micro-climate, which treats individual buildings and their direct surroundings. It is considered the smallest scale

on which the outdoor urban environment can be studied. The micro-climate discussed here is not a long-period mean value, but the instantaneous climatic conditions consisting of radiation, temperature and wind. The most basic form of buildings and street on the micro-scale is that of the urban canyon (or street canyon). The canyon is represented by two buildings with height H, which are spaced apart by a street with width W (see Fig. 1.4). When the buildings are assumed to be infinitely long, this creates a 2D representation of the urban area. The building height over street width (H/W) ratio is the main governing dimensionless number.

The first studies of the urban canyon were mainly concerned with air flow. Oke (1988) suggested that there are, in principle, three types of air flow as a function of the H/W ratio for a 2D environment. These are depicted in Fig. 1.4. When buildings are spaced far apart, there is no interaction between the obstacles (isolated roughness flow). With intermediate H/W ratios, there is interaction between the wake of the first building and the stagnation zone in front of the second building. There are high levels of mixing due to the complex interplay between these regions (wake interaction flow). For large H/W ratios, there is a skimming flow. This indicates 'closed' vortices inside the canyon, capped by a free stream flow over the buildings. There is little mixing of ambient air inside the canyon, which can trap exhaust gasses and warm air. In further studies, this classification of air flow inside the urban canyon is extended by heating of different surfaces (Kim and Baik, 2001; Bohnenstengel et al., 2004) or the effect of the H/W ratio on pollutant dispersion (Sini et al., 1996; Xie et al., 2005).

In addition to air flow and pollutant dispersion, the elementary 2D shape has also been used for studies on radiation, where different components play an important role. A numerical modelling study by Fortuniak (2008) showed that the effective albedo (the amount of radiation that is reflected back to the atmosphere) decreases with increasing building height. In addition to shortwave radiation, longwave radiation is important in the urban canyon. Especially the longwave trapping effect (radiation emitted at a surface and absorbed at another surface) can increase the urban surface temperature. These compensating radiative effects are studied in Theeuwes et al. (2014) and show a maximum urban heat island effect for a height to width ratio of H/W=1.0.

These different processes can be captured in the surface energy balance (Wallace and Hobbs, 2006), which is a balance between absorbed shortwave and longwave radiation, the sensible heat flux (heating of air) H, latent heat flux (evaporation of water) Le, and the transient conductive heat flux (heat storage as a function of time) G. Note that the conductive heat flux, which

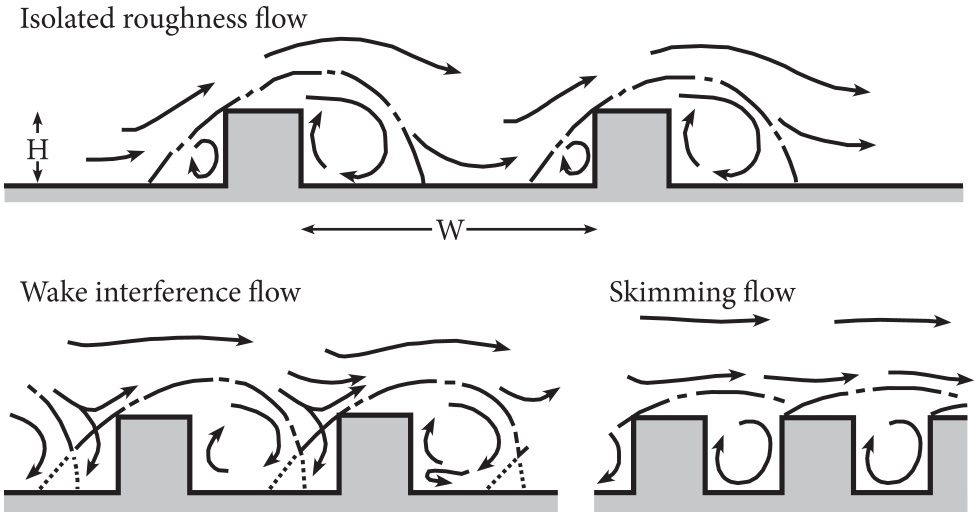

Fig. 1.4: Schematic overview of the urban canyon and the different flow regimes. Adapted from Oke (1988).

represents energy transfer into or away from the ground, is time dependent. Therefore, it acts as a heat buffer, and it is also called the storage flux. Surface temperature is determined by the magnitude of each component in the surface energy balance.

$$\overbrace{SW\downarrow - SW\uparrow + LW\downarrow - LW\uparrow}^{\text{Radiation}} = \overbrace{H + Le}^{\text{Convection}} + \overbrace{G}^{\text{Conduction}} \tag{1.1}$$

Several studies have been performed concerning the urban canyon and urban surface energy balance. This is either done by measuring or numerically investigating the above mentioned processes (Nunez and Oke, 1977; Oke, 1982, 1988; Ryu and Baik, 2012). However, the governing processes in the urban environment as a function of building aspect ratio are still uncertain.

In addition to air temperature and surface temperature, there is a third temperature which is essential, especially during daytime (even though it also present during the nighttime): the apparent temperature. This temperature is indicative of the human thermal comfort. The apparent temperature studied in this thesis is the Universal Temperature Climate Index UTCI (Fiala et al., 2012). It combines information on air temperature, wind speed, mean radiant temperature (amount of absorbed radiation by a standing person), humidity and the human metabolism. These different temperatures are linked through convective and radiative processes, which are a function

of the urban geometry, where a great amount of interaction between the different processes is present.

1.4 Numerical modelling

To study the local urban climate in a systematic way, a modelling approach is used in this thesis. Existing numerical models that focus on the urban micro-scale can be roughly filed in two groups.

One group of models is called urban parametrisation schemes. A nice overview of different urban energy models is provided in the International Urban Energy Model intercomparison (Grimmond et al., 2010, 2011). In Chapter 5 of this thesis, the model of Kusaka et al. (2001) is discussed in more detail. These urban parametrisation models are typically used in larger scale (weather) models. The goal of the urban parametrisation scheme is to represent the urban environment and the interaction on the atmosphere above, without explicitly taking into account the detailed urban geometry. These models often represent the urban geometry by a two-dimensional, symmetrical street canyon with infinite length. From the elementary 2D geometry, radiative transfer, the conductive heat flux and the transport of convective heat are computed for a 3D environment. These schemes employ tile-based parametrisations, which allow for vegetation, water and urban environment within a single grid box. Even though different a grid box can consist of different tiles, the implicit assumption made for the urban environment is that the urban geometry within a grid box behaves as a street canyon where variations in building heights, street widths and canyon orientations are not taken into account.

The second group of models is called micro-scale models. The first type of micro-scale models solves radiative transport accurately. Examples are for instance SOLWEIG (Lindberg et al., 2008) and RayMan (Matzarakis, 2000). These models simplify the surface energy balance by making assumptions on the convective heat fluxes (ventilation effects) and the conductive heat flux (energy transfer into buildings and ground). The TUF3D model developed by Krayenhoff and Voogt (2007) is an intermediate model in which only the convective heat flux is parametrised, thereby computing the heat storage inside buildings as a function of radiation in a more accurate manner.

The second type of micro-scale models aim at accurately describing air flow through the urban environment by using Computational Fluid Dynamics (CFD) modelling. These models often specify the surface temperature. This can be seen as a highly simplified surface energy balance, since radiative and conductive heat fluxes are typically not taken into account.

The model developed for this thesis (called URBSIM) is a micro-scale model, where CFD, radiative transport and the surface energy balance are coupled and refined, such that there is less need for modelling of contributions to the urban heat budget. In this way, a tool is obtained that is suited to investigate the way different processes interact. The CFD model used in this thesis is solving the Reynolds Averaged Navier-Stokes equations (RANS), which gives an accurate representation of the urban environment within reasonable computation times.

While developing the combined model, there was only one model reported in literature that combines the different processes similarly to the developed model in this thesis: ENVI-met (Bruse, 1999). This model focusses on practical applications, for instance aiding in urban planning (Taleghani et al., 2015; Kleerekoper et al., 2015), with the benefit of small computation times and a relatively easy to use interface. As a result of these choices, physical processes are parametrized and the domain size that can be investigated is limited (to reduce memory-requirements and computation time). In this thesis, it is decided to develop a new model. The focus is on representing the different processes as accurately as possible, where long computation times are accepted. Furthermore, a high degree of flexibility is required in the processes that are taken into account or neglected, in order to systematically study the urban environment. By developing different modelling approaches, information is also obtained on the level of accuracy required, which can help future models concerning the urban micro-climate.

During this PhD work, mutiple other models similar as presented in this thesis have been developing. One example is the Palm4U model, where multiple universities and research institutes developed a building resolving urban model used for scientific research and applied urban planning (Maronga et al., 2019). The Palm4U model is based on an existing Large Eddy Simulation model, and includes the urban environment, vegetation and chemistry modelling.

Another example is the PhD thesis of Suter (2019), who uses the work by Tomas et al. (2016), and extended this with radiation and the surface energy balance.

1.5 Research questions

From the start of this project, the focus has been on practical research questions, since the Climate Proof Cities consortium is partly funded by different city councils in the Netherlands.

Therefore this research started with simulations of air flow through the cities of Arnhem, Amsterdam and Rotterdam. The different neighbourhoods are converted to a Digital Elevation Model (DEM), which displays the location of buildings and the color of a building is used to indicate the height. An example for the Van Muijlwijkstraat in Arnhem is shown in Fig. 1.5. From this DEM, the buildings can be converted into a mesh, which is used for the CFD simulations. The CFD model that has been used (Kenjeres and Hanjalic, 1999, 2006, 2009; Kenjeres and ter Kuile, 2013; Kenjeres et al., 2015) only works with hexagonal grids, which means that building blocks that do not fit the square grid cells are not allowed. Therefore, all buildings are converted to square blocks, resulting into staircase like blocks which is shown for a close-up in Fig. 1.5b. The mesh is then used as input for the CFD model. These steps have been automated, such that large areas can quickly be meshed, and results can be obtained within a relatively short time frame. A typical steady RANS CFD result is shown in Fig. 1.5c, which shows the air flow (colors) and stream traces (black lines, which trace the path of an individual air packet). Ambient air flow is entering with 2 ms^{-1} from the bottom of the figure. The air flow is largely disturbed by the urban environment. There is acceleration of air through the large open roadways, flow as depicted in 1.4 when the building blocks are perpendicular to the air flow and large areas of wake interaction. The complex 3D situation makes it hard to make generic comments on the air flow pattern, since these are highly dominated by local geometric parameters. Simulations for this neighbourhood also showed transient effects, where vortex shedding from building corners is present. There is not only a large spatial variation, but also a time variation in these realistic urban environments.

In addition to simulations in Arnhem, the neighbourhood Plein '40-'45 in Amsterdam is studied, which has completely different characteristics in terms of plan area density, orientation and H/W ratio. Fig. 1.6a shows the contours of air flow and streamlines at average building height in that neighbourhood, obtained with the same method from DEM to mesh and CFD simulations as discussed in Fig. 1.5. Free stream air is entering from the left with 2 ms^{-1} and is largely disturbed by the complex urban geometry. Wind speeds inside the neighbourhood are higher compared to the neighbourhood in Arnhem, due to the large open streets that are aligned with the flow in the Amsterdam neighbourhood. However, also in this neighbourhood, the local wind speed and wind direction is largely controlled by the 3D building geometry.

As a next step, temperature effects were added in a simplified and rather crude manner, where surface temperature is only determined using sun or

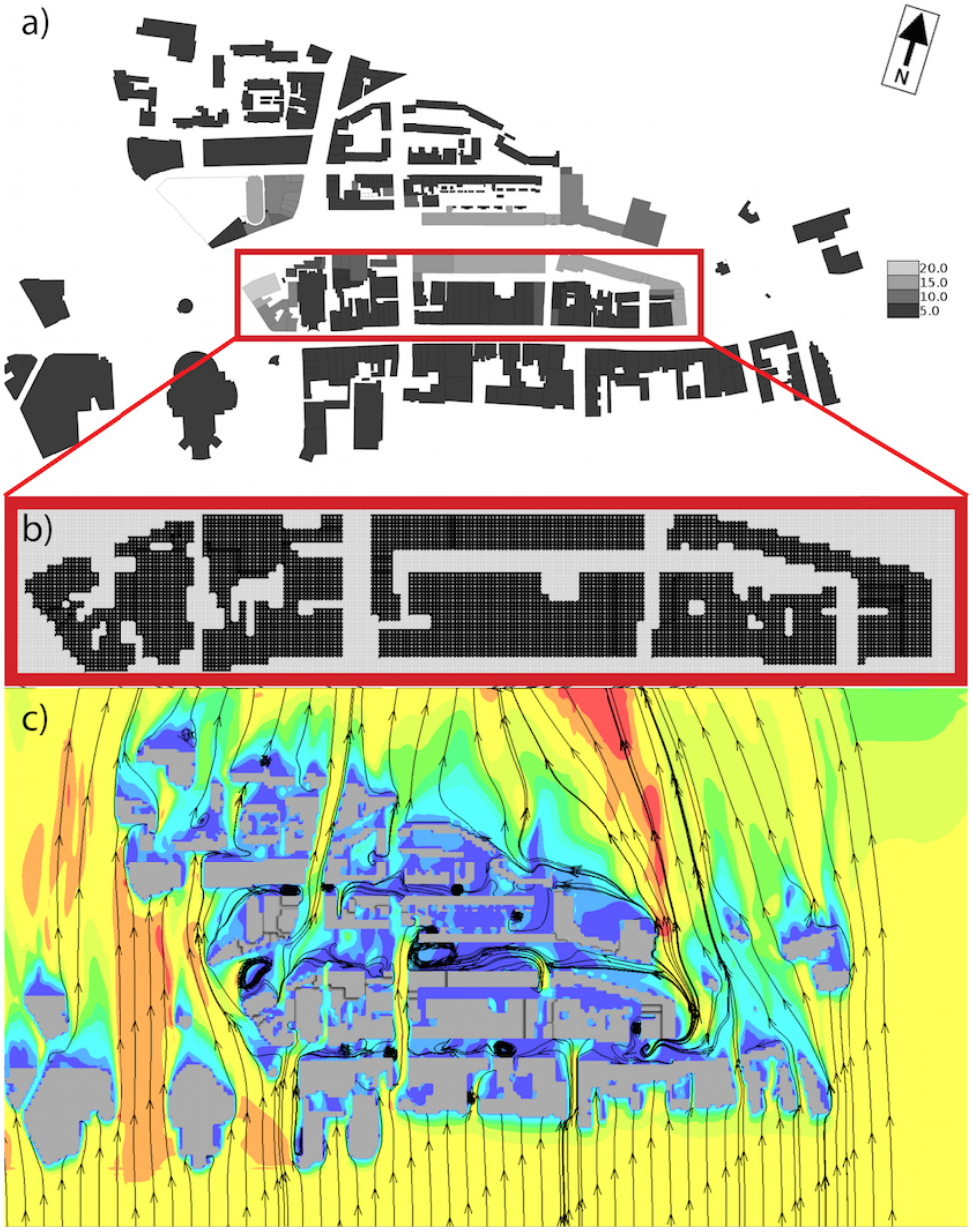

Fig. 1.5: a): digital elevation model of the neighbourhood surrounding the Van Muijlwijkstraat, Arnhem. The building height is depicted as a color, which is indicated in the legend on the right. b): Close-up of the mesh generated from the DEM. c): Velocity contours and stream traces at average building height, as calculated from the steady RANS CFD model. The mesh consists of 500 x 272 x 34 cells and 973 obstacles.

shadow locations, neglecting multiple reflections. Results for such a study are shown in Fig. 1.6b for the neighbourhood in Amsterdam which shows air temperature at average building height in combination with the stream traces which are identical to Fig. 1.6a. Free stream air has a temperature of 20°C, while surfaces that are directly sunlit have a surface temperature of 30°C and shaded areas are set to a surface temperature of 20°C. The range of air temperatures is relatively modest with air temperature differences of up to 1°C in the simulation domain. One can visually identify the link between the tunnelling of air from the stream traces and air temperature, where locations with high wind speeds are generally colder. Especially in the wake of obstacles, where wind speeds are low, air temperature is higher compared to their surroundings. This is despite the fact that these locations are often shaded, and therefore have a lower surface temperature, implying that advection of warm air plays an important role.

In reality, the surface temperature is a result of the interaction of many processes through the surface energy balance discussed in Section 1.3. These processes include multiple reflections of shortwave radiation, longwave radiation absorbed from the sky, absorption of longwave radiation that is emitted by neighbouring buildings (trapping) conductive heat flux and sensible heat flux. Even though the shortwave radiation can be modelled using a simple ray tracer (neglecting multiple reflections), the complex interaction between the processes in the surface energy balance cannot be simplified. Therefore, it was believed that the surface energy balance should be solved in high detail, to obtain realistic surface temperatures. Therefore, a radiative transfer model for the urban environment has been developed, and later a conductive heat transfer model to compute the energy transfer from the surface to the underlying material. The developed model computes the most important processes involved in the urban heat budget, but also comes with additional complexity and feedback mechanisms.

As depicted above, the amount of information obtained from the 3D CFD simulations already demonstrate a large spatial and temporal variability, without the additional complexity of the surface energy balance. Since the goal of this PhD thesis was to gain understanding in the processes governing the urban heat island, it was felt that simplifying the problem to more generic urban geometries would be better suited to increase the understanding of individual processes. Therefore, the 3D environment was abandoned in favour of the most elementary urban form: the 2D street canyon. From this basic 2D geometry, the importance of different processes and feedback mechanisms can be studied in an idealized manner, without being overwhelmed by the complexity of the 3D environment. This aids a deeper understanding of the

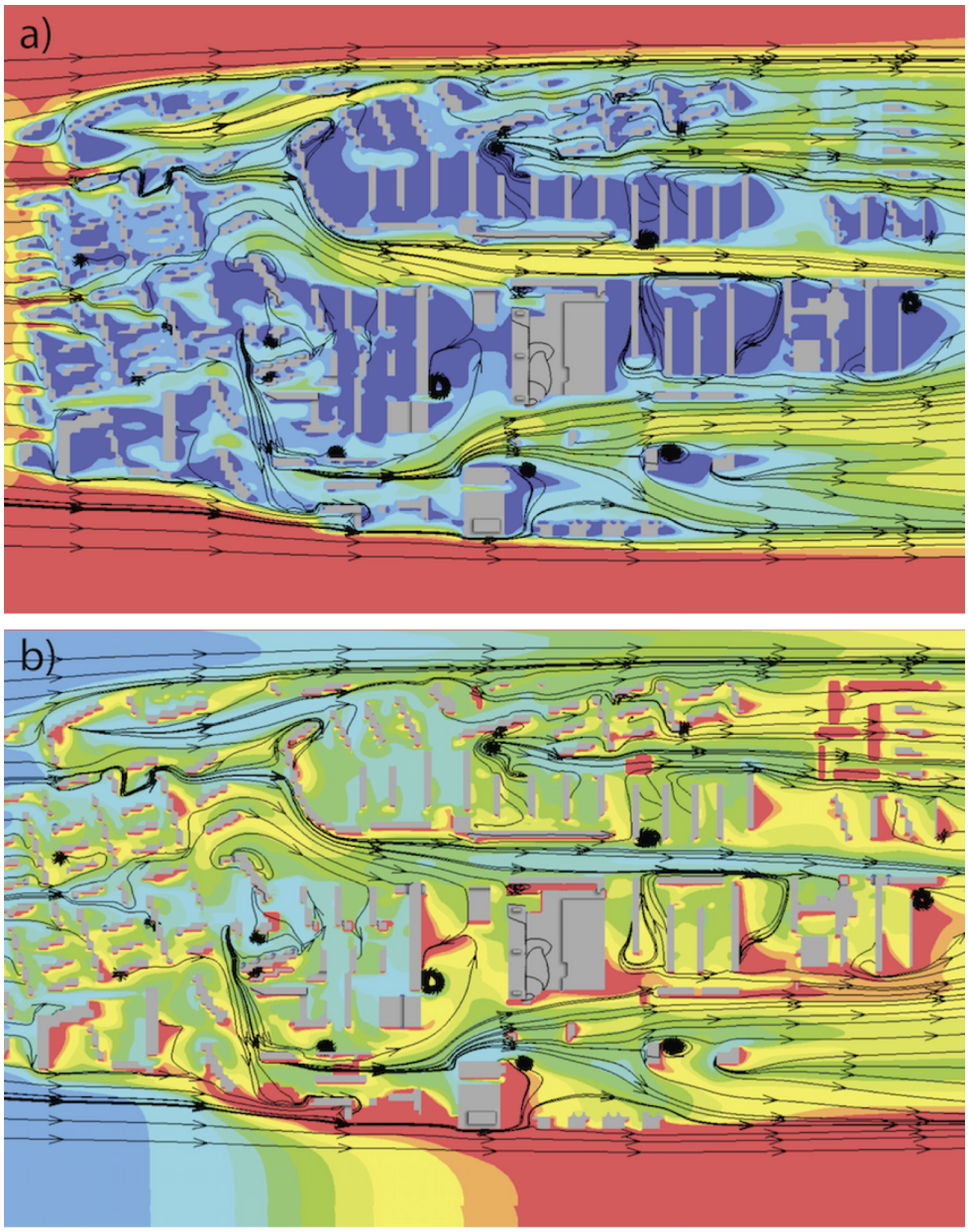

Fig. 1.6: Contours of velocity (a) and air temperature (b) and stream traces of the velocity at average building height for the neighbourhood Plein '40-'45, Amsterdam, as calculated from the steady RANS CFD model including buoyancy effects. The simulation consists of 1232 obstacles, with 404 x 218 x 55 (length, width, height) cells in the domain.

problem, that can be applied later to real-life 3D environments. In order to already provide information on the 3D environment, the developed micro-scale model is compared to urban parametrisation schemes.

Therefore, the research questions could be summarized as

- Which processes dominate the urban energy budget during day and night, and how is the budget impacted by varying the height to width ratio?
- What is the effect of different adaptation measures on air temperature, surface temperature and apparent temperature?
- How do large-scale urban parametrisations compare against the developed micro-scale model?

1.6 Outline

Within this thesis, each question will be discussed individually in a chapter. Each chapter can be read individually, as Chapters 2-4 are (based on) articles that have been published in peer reviewed journals.

Chapter 2 focusses on the nighttime energy budget of the urban environment, and is based on the publication Schrijvers et al. (2015). The developed micro-scale model is discussed in detail, and a range of H/W ratios and mechanisms are considered in order to identify the factors that have the largest influence on the urban environment.

Chapter 3 is in the same reign as Chapter 2, but focusses on the daytime situation. Besides air and surface temperature, mean radiant temperature is also considered. The mean radiant temperature is the temperature that a standing person is feeling as a function of the amount absorbed radiation, and is used in the computation of apparent temperatures like the Physiological Equivalent Temperature (PET, Höppe (1999)) and the Universal Temperature Climate Index (UTCI, Fiala et al. (2012)). The PET and UTCI can be used to determine the level of heat stress that person would perceive while standing at a location in the street, which directly related to human comfort and health.

High albedo materials (white surfaces) are often advocated as a way to mitigate the urban heat island. Chapter 4 studies the impact of these different high albedo adaptation strategies on surface temperature, air temperature and the UTCI for a single street canyon. In addition to using a uniform albedo, there are also cases where the albedo of the north and south facing

wall are varied independently and a case with an albedo gradient along the vertical walls.

Chapter 5 focusses on an urban parametrisation scheme used in meso-scale models like WRF (Weather and Research Forecast model, Skamarock et al. (2005)) where the urban environment is simplified to a 2D street canyon. In this chapter, a parametrisation scheme by Kusaka et al. (2001) is discussed and compared to the developed micro-scale model. Based on these findings, possible improvements of these parametrisation assumptions are discussed.

The thesis ends with concluding remarks and an outlook to possible future research.

Chapter 2

Breakdown of the night time urban heat island energy budget

Abstract[1]

This conceptual study aims at identifying the dominant factors involved in the nighttime urban heat island energy budget at building level for an idealized 2D urban geometry. For this purpose a simulation model has been developed which combines radiative transfer, conductive heat transfer and convective heat transport by Computational Fluid Dynamics modelling at a uniform 1 meter spatial resolution. A wide range of building height (H) to street width (W) ratios are considered. Starting from radiative equilibrium, complexity is added with each next test case, adding the longwave trapping effect, heat transfer by conduction and finally by convective transport of sensible heat. It is found that the longwave trapping effect is the main mechanism controlling the surface temperature. For H/W=0.5, canyon averaged longwave trapping and absorbed longwave radiation from the sky are similar in magnitude, but for deeper canyons longwave trapping is the main source of energy to the urban energy budget. The conductive heat flux is decreasing relative to the absorbed radiation. The sensible heat flux process is similar in magnitude to the conductive heat flux. Air temperature inside the canyon is higher then air above roof level for H/W=0.5 and H/W=2.0. Small air temperature differences are present inside the canyon.

[1]This chapter is based on the article published in Building and Environment (2015) **83** and the corrigendum published in Building and Environment (2020) **174** with H.J.J. Jonker, S.R. de Roode, S. Kenjereš

2.1 Introduction

The Urban Heat Island (UHI) is a well documented effect of anthropogenic changes to the environment (Arnfield, 2003). Several studies have shown a reduced decrease of nighttime air temperature of the urban environment in the range of 1 to 10 Kelvin (Grimmond, 2007; Klysik and Fortuniak, 1999; Kim and Baik, 2004; Oke, 1981; Steeneveld et al., 2011), and several causes for the temperature difference between the urban and rural environment have been proposed.

In principle, the urban heat island effect could be due to (Grimmond, 2007; Oke, 1982; Rizwam et al., 2008; Nunez and Oke, 1977; Oke, 1988) 1) reduced ventilation, 2) reduced evaporation, 3) enhanced release of stored heat from the urban material, 4) trapping of longwave radiation, 5) anthropogenic heat emissions, 6) enhanced absorption of shortwave radiation, 7) increased longwave radiation from the sky, and any combination of these factors. It is unclear which effect is dominant.

Several studies have been performed to find the influence of the urban environment on air temperature. Nunez and Oke (1977) performed measurements in a specially instrumented street canyon with a building height (H) to street width (W) ratio (H/W) of 0.7 in Vancouver, Canada. They found that during the night, the radiative deficit is almost entirely compensated by the release of subsurface heat storage showing the importance of canyon material.

Oke (1988) suggested the seven above mentioned causes of the urban heat island, and eliminates five of them based on observations. The two remaining causes are: decreased longwave radiation loss (longwave trapping) and an increased release of heat stored in the urban material. The relevant parameters governing the differences in air temperature were found to be the radiative geometry and the surface thermal properties. Anthropogenic heat was discarded in Oke (1988) as a source of the UHI, since the UHI is strongest in summer, whereas the peak anthropogenic heat is emitted during the winter.

The conclusion on anthropogenic heat was opposed by Ryu and Baik (2012), who performed a systematic study of different physical processes with the meso-scale WRF (Weather and Research Forecasting) model, which works on a larger scale and the urban environment is parametrized. Three main causative factors were identified: anthropogenic heat, impervious surfaces and 3D urban geometry. Their study indicated that during nighttime, the anthropogenic heat contributes most to the urban heat island, followed by the impervious surface factor (reduction in surface moisture availability and

increased thermal inertia) and the 3D urban geometry (additional heat stored in vertical walls, radiation trapping and reduction of ventilation).

In this study, performed within the Climate Proof Cities consortium (Albers et al., 2015), the line of Ryu and Baik (2012) is continued, but on a smaller scale: the scale of the urban street canyon. For this purpose a new simulation model has been developed in the line of Krayenhoff and Voogt (2007) and Krayenhoff (2010), which combines radiative transfer, heat conduction into the ground and obstacles, and Computational Fluid Dynamics (CFD) calculations for turbulent transport of sensible heat. The model and its validation is discussed in section 2.2. This section also includes the case set-up. Instead of looking at all the different processes acting together, the present study chose to start from the simplest case with only radiative transfer, and add physical processes step by step. In this way insight is gained in the different mechanisms that play a role in the urban heat island without losing the physical interpretation of the cases. The results of the simulations can be found in section 2.3. Model assumptions and limitations of the model are discussed in section 2.4, after which conclusions are drawn. Our goal is to quantify the contribution of the factors controlling the urban heat island. Therefore this study does not only add complexity in the processes that we consider, but we also consider a range of H/W ratios (0.0, 0.5, 1.0 and 2.0) in order to study the importance of building geometry.

2.2 Methods and case set-up

To perform this study, a new transient 2D simulation model has been developed which couples three different energy transport phenomena: radiative transfer, conduction and ventilation. Radiative transfer is computed with a Monte-Carlo radiation model, whereas ventilation is modelled using a CFD model. The surface energy balance is computed, which involves a 1D heat conduction equation for the conductive heat flux in the urban material. Transient simulations are performed where the diurnal cycle is taken into account. This is necessary for the computation of the conductive heat flux, which is dependent on the daytime conditions. All sub-models will be discussed and validated separately in this section.

2.2.1 Radiative transfer

A Monte-Carlo radiation model is developed to compute the radiative transfer in a complex urban geometry. The Monte-Carlo model computes photon paths for direct and diffuse shortwave radiation and longwave radiation emitted by the sky and by walls. Direct and diffuse splitting of shortwave

radiation is based on Skartveit et al. (1998).

Used variables in Skartveit et al. (1998) are (see table 2.2): I the solar constant, d_{n} the Julian date, latitude and longitude, T_{L} the Linke turbidity factor (Kasten, 1996) and γ the solar zenith angle, which is computed based on Iqbal (1983). Only clear skies are considered, which results in a maximum incoming direct shortwave radiative flux at the top of the domain of 833.1 Wm^{-2} and a maximum incoming downward diffuse shortwave radiative flux of 84.2 Wm^{-2} at mid-day.

For longwave radiation, the Stefan-Boltzmann law ($E = \epsilon\sigma T_{\mathrm{s}}^4$) is assumed, where Kirchoff's law is applied, i.e. the same value of the emission of longwave radiation (ϵ) is used for the absorption ($\alpha = \epsilon$). If a surface is hit, reflected photon packets require a new direction based on the Lambertian cosine law. The same assumption is made for diffuse emitted photon packets emitted at the top of the domain, such that the angle distribution is cosine weighted. The amount of longwave radiation emitted by the sky is taken as $LW_{\mathrm{sky}} = \epsilon_{\mathrm{sky}}\sigma T_{\mathrm{a}}^4$, where the emissivity of the sky is computed following Prata (1996) as

$$\epsilon_{\mathrm{sky}} = 1 - \left(1 + c\frac{e_{\mathrm{a}}}{T_{\mathrm{a}}}\right) \times \exp\left[-\sqrt{1.2 + 3.0 \times c\frac{e_{\mathrm{a}}}{T_{\mathrm{a}}}}\right] \tag{2.1}$$

where e_{a} is the water vapour pressure (in hPa) which uses the relative humidity which is set to 75% in this study, T_{a} the free stream air temperature (in K) and $c = 46.5$ K/hPa is constant based on typical values for the water vapour scale height and temperature lapse rate (Prata, 1996).

Photon paths are tracked using step sizes from one grid cell face to another. If a surface is hit, a fraction of the energy ζ is absorbed (based on material albedo or emissivity), while the remainder travels in a random direction based on the Lambertian cosine law with a fraction $(1 - \zeta)$ energy left. Horizontal periodic boundary conditions are applied, such that a photon packet can only leave the domain through the top boundary. To reduce computation time, photon packets with less than 0.5% of the initial energy are discarded in an unbiased manner.

All diffuse radiative components (diffuse shortwave radiation, longwave radiation emitted by the sky and longwave radiation emitted by surfaces) are computed once, after which the photon distribution is stored. Longwave radiation emitted by the sky and the diffuse shortwave component can be scaled, since these are only a function of the building geometry, and not on time of the day. For the longwave radiation emitted by the surface, the

surface temperature determines the amount of emitted longwave radiation. Therefore the spatial photon distribution is stored per grid cell. Not only the amount of emitted energy is stored, but also the emitted radiation that is absorbed at another surface (longwave trapping). Direct shortwave radiation is computed each time step, since the solar zenith angle changes with time.

The number of photon packets emitted is dependent on the covered area and the size of the obstacles. $N = 10^5$ photons per m^2 are taken into account per radiation component, which proved to be sufficient to get convergent statistics.

Validation longwave radiation: 2D infinite canyon

The first validation case consists of two infinite parallel walls, where longwave radiation is emitted and absorbed. The surface temperature depends on the radiative transfer and on the fixed inner wall temperature (T_b) that is given at a distance Δx from the surface. The set-up is shown in the inset of Fig. 2.1, where the dashed line is the surface and the solid line is the depth at which the inner wall temperature is fixed. An analytical solution for this case exists (Mills, 1999), which takes into account 4 components: 1) conductive heat flux, 2) emitted radiation by surface 1, 3) radiation emitted by surface 1, reflected by surface 2 and then absorbed by surface 1 and 4) radiation emitted by surface 2 and absorbed by surface 1. In formula form, this takes the form of

$$-k\frac{T_1 - T_{\mathrm{b},1}}{\Delta x_1} - \epsilon_1\sigma T_1^4 + \frac{\epsilon_1\sigma T_1^4(1-\epsilon_2)\epsilon_1}{1-(1-\epsilon_1)(1-\epsilon_2)} + \frac{\epsilon_2\sigma T_2^4\epsilon_1}{1-(1-\epsilon_1)(1-\epsilon_2)} = 0 \tag{2.2}$$

where T_1 is the surface temperature of surface 1, $T_{\mathrm{b},1}$ is the corresponding inner wall temperature, Δx_1 the depth at which the inner wall temperature is specified (1 meter in this case) and ϵ_1 the emissivity of wall 1. The same formula holds for surface 2, which allows to solve both T_1 and T_2.

Fig. 2.1-left shows the results for the case where the fixed inner wall temperature of surface 2 is varied from 293.15 to 273.15K, while surface 1 has an inner wall temperature of 293.15K. The emissivity ϵ is constant and set to 0.95 for both walls. The surface temperature is a function of the conductive heat flux and the radiative transfer between the two surfaces. With a lower inner wall temperature, the surface temperature will decrease, thereby decreasing the amount of emitted longwave radiation. This will affect the other wall due to a reduced radiative transfer and will therefore also start

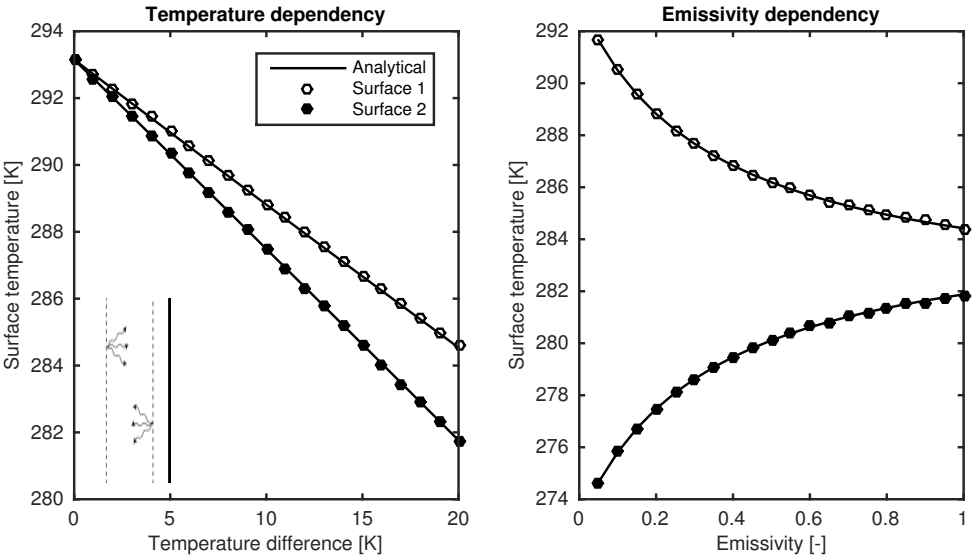

Fig. 2.1: Validation of longwave radiative transfer with analytical results (Mills, 1999) for two infinite parallel walls. The left panel shows surface temperature as a function of inner wall temperature difference between surface 1 and 2, with ϵ_1=ϵ_2=0.95. The right panel shows the dependency of surface temperature on the emissivity where ϵ_1=ϵ_2, $T_{\mathrm{b},1}$=293.15K and $T_{\mathrm{b},2}$=273.15K.

to cool. Since infinite plates are assumed, there will be a balance between conductive heat flux, emitted radiation and absorbed radiation. Results show a linear decrease of surface temperature for both walls with decreasing inner wall temperature of surface 2, and good agreement between the analytical and Monte-Carlo results. The maximum difference in surface temperature that is found is 0.04K without systematic errors.

Fig 2.1-right shows the surface temperature where the emissivity is varied from 0 to 1. The inner wall temperature of surface 1 is fixed at 293.15K, the inner wall temperature of surface 2 is set to 273.15K while the emissivity is the same for both walls (ϵ_1=ϵ_2). With lower emissivity values, there is more reflection and thus less radiative energy transfer between the surfaces. This leads to higher temperature differences between the two walls. In the case of ϵ=0, the surface temperature is equal to the inner wall temperature. The maximum error between analytical and Monte-Carlo results is 0.03K.

Validation shortwave radiation: Aida test case

Validation for shortwave radiation is conducted by comparing simulation result to the effective albedo measurements by Aida (1982). The albedo is a material property, but the effective albedo is the amount of radiation reflected from a system, in this case a street canyon. Although a variety of geometries are used in Aida (1982), only the 3D grid geometry (see inset Fig. 2.2) is used here. This case consists of cubic concrete blocks of 0.15m, which are spaced 0.15m apart (H/W=1.0). The material albedo of the blocks is 0.41. The experiment was conducted on the top of a building in the campus of Yokohama National University (35° 28' N, 139° 35' E) over a diurnal cycle in summer and wintertime. Although the albedo of the concrete is 0.41, the effective albedo is lower in both cases due to the multiple reflections, which increase the shortwave absorption within the block geometry.

Results of the Monte-Carlo simulations are shown in Fig. 2.2, where the solar zenith angle is plotted against the effective albedo. The morning period is plotted with negative solar zenith angles to distinct the morning and afternoon period. During winter, the solar zenith angle ranges from 90 to 58 degrees. A diurnal pattern is visible with the effective albedo approaching the surface albedo for zenith angles close to 90 degrees. At noon, the effective albedo drops to 0.25, in line with the experimental data.

During summer, the solar zenith angle ranges from 90 to 10 degrees. The same geometry and boundary conditions are used as for the winter case, but the diurnal pattern is less visible. This is due to the changed splitting of direct and diffuse radiation. In the summer case, the turbidity (amount of aerosols and dust particles in the air) is increased which means that relatively more diffuse radiation is scattered, causing a relatively large contribution of downward diffuse solar radiation. Since the zenith angle distribution of diffuse shortwave radiation is independent of time, this reduces the diurnal pattern in the effective albedo. A fair agreement is found between the Monte-Carlo simulation and experimental data.

2.2.2 Conductive heat flux

The conductive heat transfer (G) is computed using the temperature gradient inside the into the ground or obstacle as

$$G_i = \lambda \frac{\partial T}{\partial \xi} \tag{2.3}$$

with ξ the direction perpendicular to the surface.

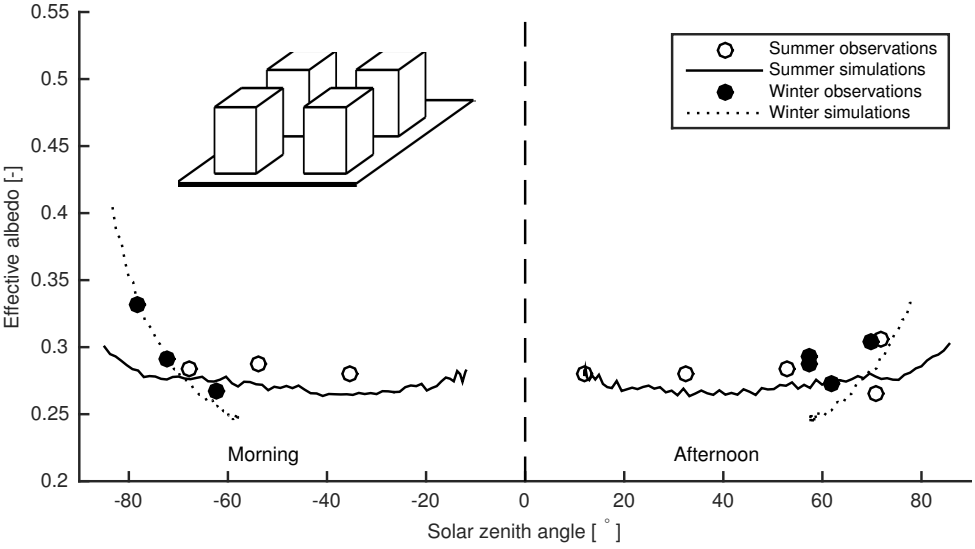

Fig. 2.2: Validation of shortwave radiation with experimental data of Aida (1982). Effective albedo is plotted for summer and winter conditions against the solar elevation angle. Morning data is plotted with negative solar zenith angles for clarity.

The temperature gradient in the urban material is a function of time and space, and is computed in 1D as

$$\frac{\partial T}{\partial t} = k_{\mathrm{d}} \frac{\partial^2 T}{\partial \xi^2} \tag{2.4}$$

where k_{d} is the thermal diffusivity, based on the conductivity λ, density ρ and specific heat C_{v} of the material

$$k_{\mathrm{d}} = \frac{\lambda}{\rho C_{\mathrm{v}}} \tag{2.5}$$

This equation can be solved by applying two boundary conditions. On the surface, the surface temperature of each individual grid cell is used. For the interior of the building or ground, a zero flux boundary condition is used at a distance $\Delta\xi$.

With these boundary conditions, temperature profiles into the ground and obstacle are computed by using the finite difference method, where fifty layers are used with a time step of 1 second. The time step of the other sub models is 6 minutes, indicating that the conductive heat flux only updates the surface temperature boundary condition at this time period.

2.2.3 Computational Fluid Dynamics (CFD) model

The outdoor airflow is computed by an in-house CFD model, which uses the Transient Reynolds Averaged Navier-Stokes (T-RANS) equations to solve air flow, air temperature distribution and sensible heat flux (Kenjeres and Hanjalic, 1999, 2006, 2009; Kenjeres and ter Kuile, 2013). The equations for mass, momentum and temperature are

$$\frac{\partial U_i}{\partial x_i} = 0 \tag{2.6}$$

$$\frac{\partial U_i}{\partial t} + U_j \frac{\partial U_i}{\partial x_j} = \nu \frac{\partial^2 U_i}{\partial x_j^2} - \frac{1}{\rho}\frac{\partial P}{\partial x_i} - \frac{\partial \overline{u_i u_j}}{\partial x_j} - g_i \beta (T - T_{\mathrm{ref}}) \tag{2.7}$$

$$\frac{\partial T}{\partial t} + U_j \frac{\partial T}{\partial x_j} = \kappa \frac{\partial^2 T}{\partial x_j^2} - \frac{\partial \overline{\theta u_j}}{\partial x_j} \tag{2.8}$$

where U_i is the i-th component of the velocity, U gives the ensemble averaged value and u gives the fluctuation around variable U, T is the temperature and θ the fluctuations around T, P is the pressure, ν the viscosity, ρ the density, g the gravitational vector, β the thermal expansion coefficient, T_{ref} a reference temperature and κ the thermal diffusivity.

The turbulent stress $\overline{u_i u_j}$ and turbulent heat flux $\overline{\theta u_j}$ are unknown and require modelling. For velocity, the standard $k-\epsilon$ turbulence model is used. Here, the unknown turbulent stress is modelled by using the eddy viscosity hypothesis. The eddy viscosity is then computed by a ratio between turbulent kinetic energy and dissipation, which both have their own transport equations

$$\frac{\partial k}{\partial t} + U_j \frac{\partial k}{\partial x_j} = \frac{\partial}{\partial x_j}\left[\left(\nu + \frac{\nu_{\mathrm{t}}}{\sigma_{\mathrm{k}}}\right)\frac{\partial k}{\partial x_j}\right] - \overline{u_i u_j}\frac{\partial U_i}{\partial x_j} - \epsilon - g_i \beta \overline{\theta u_i} \tag{2.9}$$

$$\begin{aligned}\frac{\partial \epsilon}{\partial t} + U_j \frac{\partial \epsilon}{\partial x_j} = \frac{\partial}{\partial x_j}\left[\left(\nu + \frac{\nu_{\mathrm{t}}}{\sigma_{\epsilon}}\right)\frac{\partial \epsilon}{\partial x_j}\right] + \\ \frac{\epsilon}{k}\left(C_{\epsilon 1}\overline{u_i u_j}\frac{\partial U_j}{\partial x_i} - C_{\epsilon 2}\epsilon + C_{\epsilon 3} g_i \beta \overline{\theta u_i}\right)\end{aligned} \tag{2.10}$$

$$\nu_{\mathrm{t}} = C_{\mu}\frac{k^2}{\epsilon} \tag{2.11}$$

C_μ	σ_k	σ_ϵ	$C_{\epsilon 1}$	$C_{\epsilon 2}$	$C_{\epsilon 3}$
0.09	1.0	1.3	1.44	1.92	1.44

Table 2.1: Model constants for the standard $k-\epsilon$ turbulence model

where k is the turbulent kinetic energy (TKE), ϵ is the dissipation of TKE, and C_μ, σ_k, σ_ϵ, $C_{\epsilon 1}$, $C_{\epsilon 2}$ and $C_{\epsilon 3}$ are constants, taken from the standard $k-\epsilon$ model (see table 2.1).

The unknown turbulent heat flux is modelled by the Simple Gradient Diffusion Hypothesis (SGDH) model, which relates the turbulent heat flux to the eddy viscosity and temperature gradient

$$-\overline{\theta u_i} = \frac{\nu_\mathrm{t}}{\mathrm{Pr_t}} \frac{\partial T}{\partial x_i} \tag{2.12}$$

where $\mathrm{Pr_t}$ is the turbulent Prandtl number, which is constant and set to $\mathrm{Pr_t} = 0.86$. The sensible heat flux is now computed with

$$H_i = \rho c_\mathrm{p} \overline{\theta u_i} \tag{2.13}$$

where ρ is the density of air (1.208 $\mathrm{kgm^{-3}}$) and c_p the specific heat capacity of air (1004 $\mathrm{Jkg^{-1}K^{-1}}$).

The latent heat flux is ignored in this study.

CFD validation

The CFD model has been validated by comparing simulation results with experimental data by Uehara et al. (2000). In this experiment, a grid-structure of 100mm high obstacles are placed in a heated wind tunnel where neutral (R_b=0), stable (R_b=0.78) and unstable (R_b=−0.21) stratifications are considered; here the Richardson number R_b is defined as

$$R_\mathrm{b} = \frac{gH(T_\mathrm{a} - T_\mathrm{f})}{TU_\mathrm{H}^2} \tag{2.14}$$

where H is obstacle height, T_a the free stream air temperature, T_f floor temperature and U_H the velocity at obstacle height.

Measurements are conducted in the 5th street canyon, where wind speed and temperature profiles are measured. The Reynolds number based on obstacle height and the velocity at roof level is constant for all measurements at $R\mathrm{e}$=10^4.

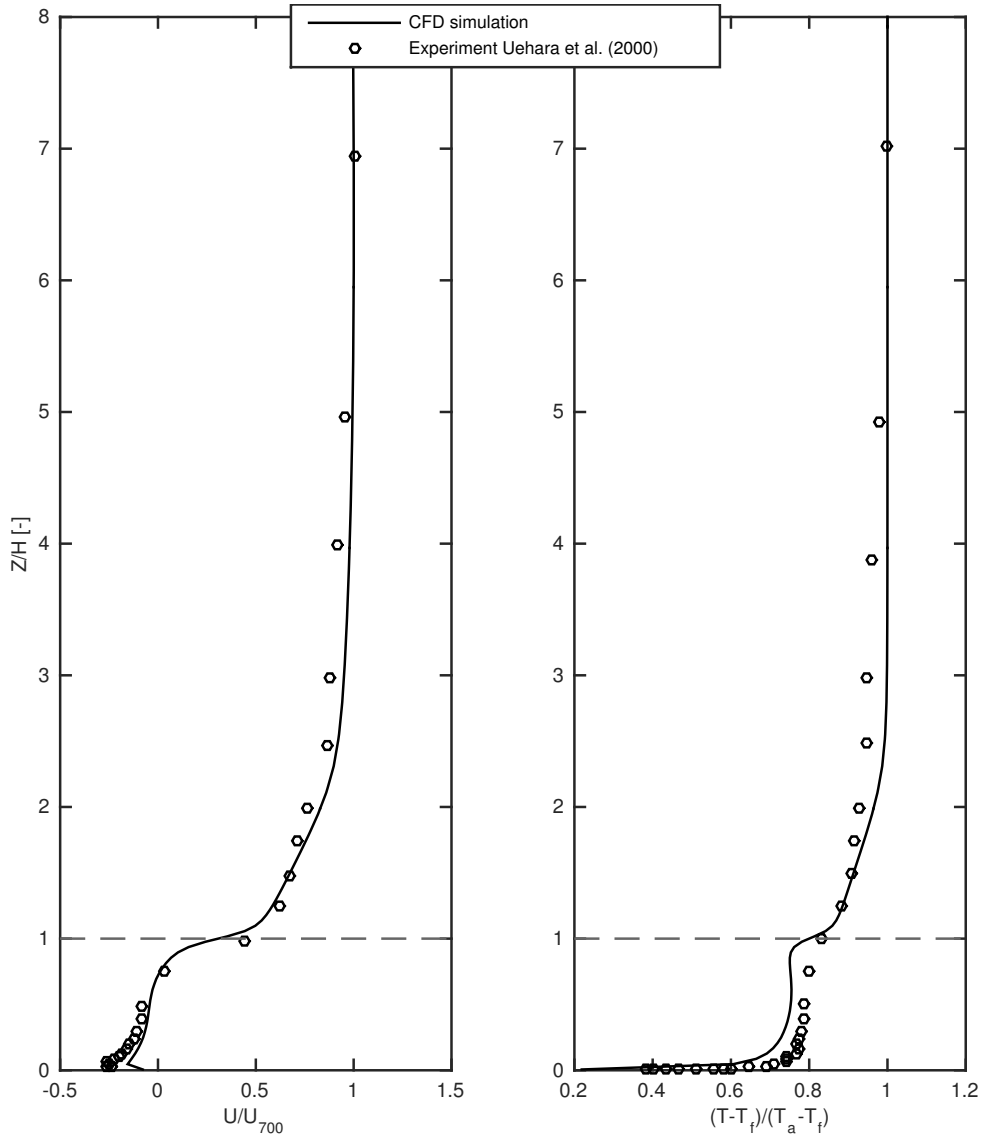

Fig. 2.3: Validation of the CFD model with experimental data by Uehara et al. (2000) with Re=10^4 and R_b=−0.21. The left panel shows non-dimensional velocity (scaled with u_{700}=1.6ms^{-1}) as a function of height (scaled with obstacle height H=0.10m). The right panel shows non-dimensional temperature profiles, scaled with T_a=293.15K and T_f=352.15K. Building height is at Z/H=1.

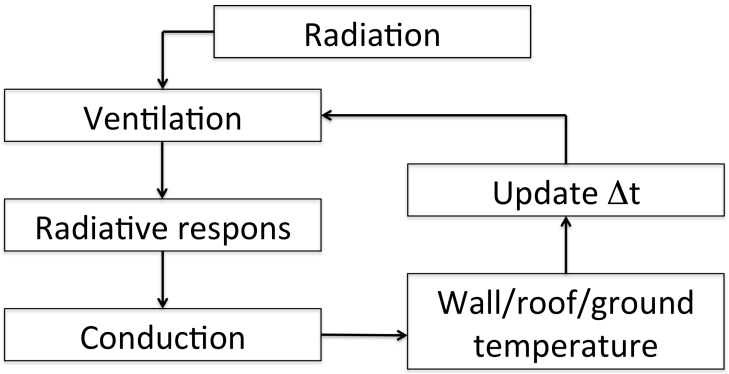

Fig. 2.4: Different sub models and computation order that is used to compute the surface energy balance for each grid cell.

Results for the strong unstable case (R_b=−0.21) are shown in Fig. 2.3, where velocity profiles are shown in the left panel and temperature profiles in the right panel. Velocity profiles demonstrate good agreement between experiment and simulation, with a wake region below building height. Velocity is scaled with the wind speed at 700mm (7 times obstacle height), which is u_{700}=1.6ms^{-1}.

Air temperature profiles are scaled with the free stream air temperature T_a=293.15K and the specified floor temperature T_f=352.15K and show reasonable agreement between measurements and simulations. The largest differences are found below building height, where the CFD model shows lower air temperatures compared to measurements. The maximum difference between measurement and simulation is 2.9K, with an air temperature of 303.6K for the CFD simulation and 306.5K for measurements at 0.9H. This is probably due to the mixing of air inside the canyon, which is overestimated in the CFD model.

2.2.4 Integrated energy balance model

With all individual components discussed and validated, these are combined into one model. This section discusses the details of this coupling. The equation that needs to be solved is the energy balance per grid cell,

$$SW_{\mathrm{dir}} + SW_{\mathrm{dif}} + LW_{\mathrm{sky}} + LW_{\mathrm{trap}} = LW_{\mathrm{out}} + H + G \qquad (2.15)$$

where SW_{dir} is the absorbed direct component of shortwave radiation, SW_{dif} the absorbed diffuse shortwave component, LW_{sky} the absorbed longwave radiation emitted by the sky, LW_{trap} the longwave radiation emitted by one surface and absorbed by another surface, LW_{out} is the emitted longwave radiation by surfaces, H the sensible heat flux (where a positive flux is heating of air) and G the conductive heat flux (positive is adding energy to the underlying layers). Note that SW_{dir}, SW_{dif} and LW_{sky} also include multiple reflections.

As a first step, all diffuse radiative components are computed and stored in memory. Based on the surface temperature of the previous time step, all other fluxes in eq. 2.15 are computed, which results in a net flux F which is the surplus or deficit of energy per grid cell. Based on this net flux, the surface temperature is computed by

$$\Delta_{\mathrm{skin}}\rho_{\mathrm{skin}}C_{\mathrm{v,skin}}\frac{\partial T_s}{\partial t} = F \tag{2.16}$$

where a skin layer is assumed with $\Delta_{\mathrm{skin}}\rho_{\mathrm{skin}}C_{\mathrm{v,skin}}$=0.01 $\mathrm{JK^{-1}m^{-2}}$. This skin layer prevents large changes in surface temperature from one time step to the other. A sensitivity study to the skin layer is discussed is Section 2.5.3.

The computed surface temperature is fed back as a new boundary condition into the CFD model where a transient simulation is conducted with 50 iterations per time step of 6 minutes (see Fig. 2.4 for the overview of steps taken per time step). The T-RANS simulation provides information on the development of vortices and changes of these during the day due to buoyancy effects. The surface temperature is also fed to the radiative transfer model, where the longwave radiation emitted by walls is computed for the next time step. This does not only influence the outgoing longwave radiation, but also longwave trapping.

2.2.5 Test cases and research methodology

To test the effect of different mechanisms and the effect of changing the H/W ratio, an urban geometry is simulated with 10 obstacles (see Fig. 2.5). This set-up mimics an idealized 2D city, where all obstacles have uniform height and have equal spacing. The number of obstacles give rise to a fully developed flow pattern in the last canyon, which means that more obstacles will not change the results from canyon to canyon. Building width is constant at B=25 meter, street width is constant at W=50m, while building height is varied ranging from 0.0 meter (H/W=0.0), 25 meter (H/W=0.5), 50 meter (H/W=1.0) and 100 meter (H/W=2.0). With this range of H/W ratios, the

effects can be studied of different mechanisms on the surface temperature and air temperature inside the street canyon.

In addition to changes in the obstacle height, also different physical mechanisms are considered (see table 2.3 for an overview). The simplest test case is considered first, where the longwave trapping mechanism, conductive heat flux and sensible heat flux are not included. This causes a radiative equilibrium, where all absorbed radiation is emitted again through longwave radiation and leave the domain without being perturbed by the other obstacles. longwave trapping is included in case 2, the conductive heat flux process is added in case 3 and finally the sensible heat flux process is added in case 4.

To obtain quasi-steady state results (indicating that the diurnal cycle is repetitive), 10 days are considered. A quasi steady state is required for two reasons 1) the temperature profile into the ground or obstacle is independent of the initially estimated temperature profile at t=0 and 2) the air flow and turbulence production is independent of the surface temperature at t=0. All results shown here satisfy this quasi-steady state constraint. Starting from the 10th of June, the simulation runs for 10 days with a time step of 6 minutes and results for the night between day 10 and 11 will be considered.

The input parameters for the cases are shown in table 2.2. The results plotted in Figures 7-10 are done according to the inset in Fig. 2.5. Vertical walls are normalized to a height of 1, independent of the actual building height. This allows us to compare all H/W ratios in a single graph similarly. Horizontal surfaces are normalized by the street width in such way, that all surfaces have a length of 1.

2.3 Results

2.3.1 Time series

To give an overview of time-evolution, the H/W=0.0 case i.e. no buildings (also referred to as flat plate) is plotted in Fig. 2.6. The spatially averaged surface temperature is shown in the left panel, while the spatially averaged surface fluxes for case 4 (the case including conductive and sensible heat fluxes) are shown in the right panel.

The surface temperature for case 1 shows a large diurnal variation, ranging from 278K to 358K. This is due to our assumption of radiative equilibrium for this case. There are no compensating mechanisms to limit the surface temperature from reaching very high or low values. When the conductive heat flux process is added (case 3) energy is transferred into the ground

	Radiation
Solar constant I	1360 Wm^{-2}
Emissivity	0.95
Albedo	0.40
Latitude	52° 22' N
Longitude	4° 53' E
Start date	2012-06-10 00:00
End date	2012-06-20 23:59
	Heat conduction
λ	0.72 $\mathrm{Wm}^{-1}\mathrm{K}^{-1}$
ρ	1920 kgm^{-3}
C_v	835 $\mathrm{Jkg}^{-1}\mathrm{K}^{-1}$
$\Delta\xi_{ground}$	1 m
$\Delta\xi_{building}$	0.25 m
	CFD
T_a	293.15 K
U	4.0 m/s
cell width	1.0 m

Table 2.2: Input constants for radiative transfer, heat conduction and the CFD model.

during the day and released again during the night, leading to less extreme surface temperatures. Finally, when the sensible heat flux process is added (case 4), there is now a second compensating mechanism which decreases surface temperature variations compared to case 3. Since the free stream air temperature is 293.15K, adding the sensible heat flux process will reduce the surface temperature during day, while at night the sensible heat flux will have a heating tendency.

When the individual fluxes are studied (Fig. 2.6-right, results are shown for case 4), it shows that the conductive heat flux (G) has it's largest negative value just after sunset (sunset and sunrise are indicated as a dotted lines). From this point in time, the conductive heat flux will release energy to the surface, thereby creating smaller temperature gradients inside the material and thus lowering the conductive heat flux itself. When the sun rises, the conductive heat flux follows the absorbed radiation at the surface. The sensible heat flux (H) is negative during the night. During the day, the sensible heat flux rises, peaks after mid day and declines during the afternoon.

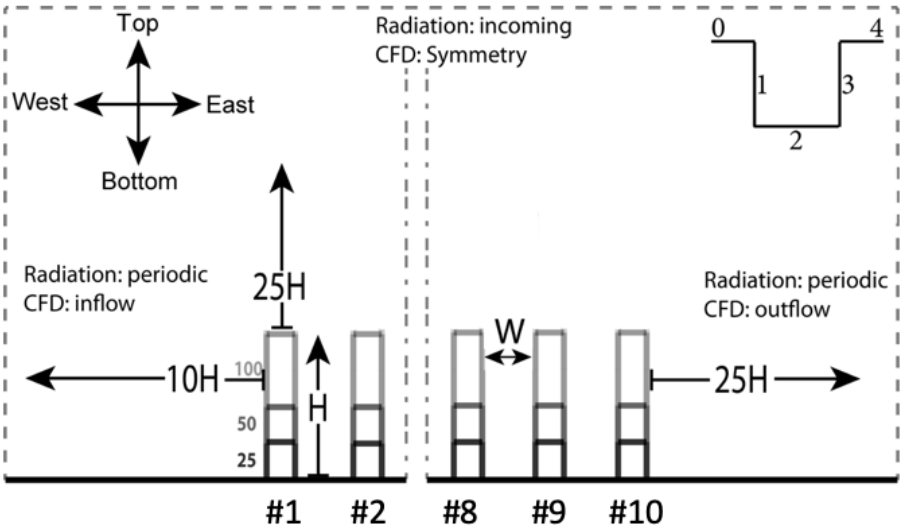

Fig. 2.5: Schematic of case set-up including spacing around obstacles. 10 buildings are spaced 50 meter apart, while building height is varied. Building height (H) is defined as the height from the ground plane to the top of the obstacle. Plotting is done according to the inset in the top right.

The dashed line in both graphs is the middle of the night between June 20 and June 21 (the last night of the simulation). This point in time will be used for detailed analysis of the spatial surface temperature and surface fluxes within the street canyon.

2.3.2 Radiation

The spatial radiative fluxes as observed during the middle of the night between simulation days 10 and 11 are displayed in Fig. 2.7. The street canyon between obstacle 9 and 10 (see Fig. 2.5) is used for the analysis. Plotting is done according to the inset shown in Fig. 2.5 and again in the middle panel of Fig. 2.7 for clarity.

For the flat plate, longwave radiation from the sky is uniformly absorbed. When obstacles are present, the same value at roof level is obtained as for the flat plate, since the same emissivity is used for all surfaces and there are no multiple reflections or longwave trapping effects. Inside the canyon, there is a decrease of absorbed longwave radiation from the sky at the vertical walls, where the absorbed radiation is decreasing when approaching ground level. At the ground surface, a parabolic-like shape is found, which peaks at the

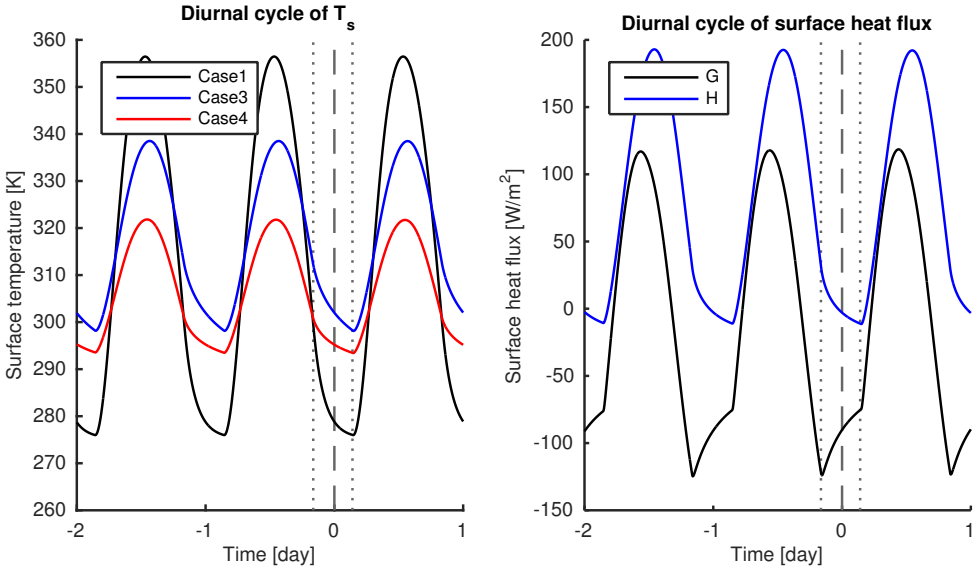

Fig. 2.6: Time series for the flat plate case. The left panel shows the surface temperature for the radiative equilibrium case (case 1), case with conductive heat flux (case 3) and sensible heat flux (case 4). The right panel shows the conductive (G) and sensible heat flux (H) at the surface for H/W=0.0 for case 4. Dotted lines indicate sunset (-0.15) and sunrise (0.15), while the time instance at the dashed line is used to compare spatial results.

Case	RAD	LW_{trap}	G	H
1	+			
2	+	+		
3	+	+	+	
4	+	+	+	+

Table 2.3: Physical mechanisms that are considerd per case. For each case, five different H/W ratios are computed.

centre of the canyon. This is due to the sky view factor, which is largest at that point. With increasing H/W ratio, the spatial variation of the sky view factor at street level is reduced, resulting in smaller variations at ground level.

Longwave trapping is defined in this paper as the amount of longwave radiation emitted by a surface and absorbed at another surface. Longwave trapping is absent for the case with H/W=0.0, since all radiation is emitted towards the sky and nothing is absorbed elsewhere. When buildings are present, there is a peak at the lower corner levels in the street canyon where the longwave trapping effect is most effective, while at the middle of the ground surface the longwave trapping effect reduces. With increasing H/W ratio, the energy involved with longwave trapping increases. For deep canyons, there is a larger surface area that emits longwave radiation compared to a shallow canyon. In addition, longwave radiation cannot escape deep canyons as easily as for shallow canyons.

Since radiative equilibrium is assumed, the absorbed and emitted longwave radiation should balance. This is shown in the bottom panel. Since the roof and flat terrain have the same radiative properties, these overlap for all H/W ratios. In the street canyon, emitted radiation is increasing with increasing H/W ratio. The longwave trapping effect exceeds the reduced absorption from longwave radiation emitted by the sky.

2.3.3 Surface temperature

If only radiation is taken into account, important processes are ignored. Therefore, we add the longwave trapping effect, conductive and sensible heat flux mechanism for each test case. Results are shown in Fig. 2.8, which shows the surface temperature for different cases (lines) and different H/W ratios (different sub-plots). From the results for case 1, similar patterns can be observed as for the absorbed longwave radiation from the sky (Fig.

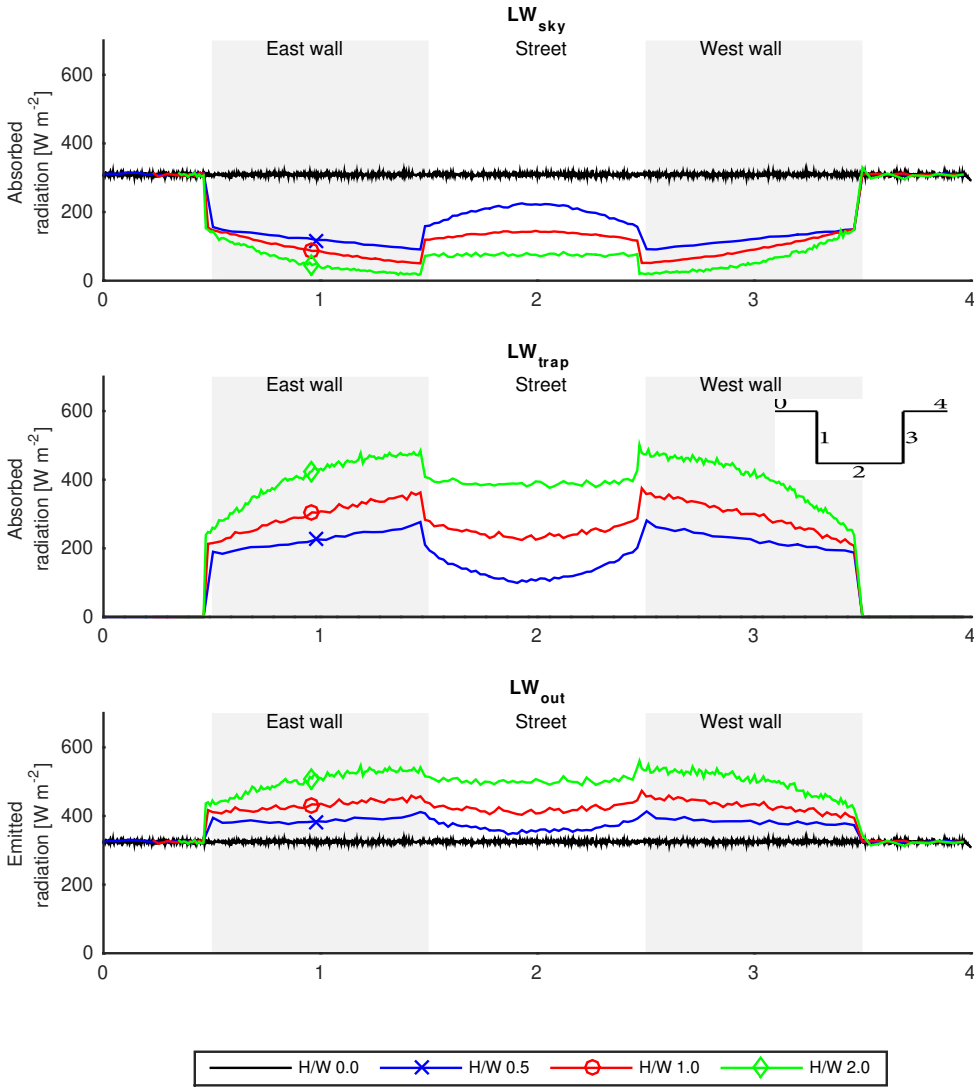

Fig. 2.7: Absorbed longwave radiation from the sky (top), absorbed radiation due to longwave trapping (middle) and emitted longwave radiation by walls (bottom) in case of radiative equilibrium including longwave trapping (case 2) for different H/W ratios (lines). Plotting is done according to the inset in the middle panel.

2.8), with a rapid decrease of surface temperature along the vertical walls and a parabolic-like shape at ground level. Surface temperatures can reach extremely low values of 150K deep inside the street canyon, since the surface temperature is only determined by the amount of absorbed longwave radiation.

The longwave trapping effect has a large heating tendency, where especially the lower parts of the vertical walls show a large increase in surface temperature. This effect can be as big as 160K (for H/W=2.0). Also for the ground surface, surface temperatures are increasing for all non-zero H/W ratios as a result of longwave trapping.

If case 3 (which includes the conductive, but not the sensible heat flux mechanism) is considered, there is again a further increase of surface temperature. Energy is stored during the daytime and released during the night, as shown in the time-series of Fig. 2.6. The spatial change in surface temperature is quite constant, indicating that there is no preferential location where the conductive heat flux is most active.

When the sensible heat flux process is added, a nearly constant surface temperature is observed over the canyon. Due to our free stream air temperature of 293,15K, the sensible heat flux forces surface temperature towards this free stream air temperature. For H/W=1.0 there is a large dip in the surface temperature at the west wall corner with the roof, which is due to an artificial increase in the turbulent viscosity. The increase in viscosity results in an unrealistically large sensible heat flux which extracts heat from the surface and leads to a low surface temperature. This issue is further discussed in Chapter 3 of this thesis.

2.3.4 Surface fluxes

Although the surface temperatures shown in Fig. 2.8 are insightful, it is hard to distinguish the contributions of different physical mechanisms. Therefore, all surface fluxes that are computed in Eq. 2.15 are shown here for case 4 (see Fig. 2.9). Note that a positive value of LW_{out}, G and H means extraction of energy from the surface (cooling tendency).

For the flat plate this shows that LW_{sky} is 300 Wm^{-2}, while the emitted longwave energy is 400 Wm^{-2}. This energy deficit is compensated by the sensible and conductive heat fluxes, with each component adding 50 Wm^{-2} to the surface. In Fig. 2.9, the lines for the conductive and sensible heat flux are overlapping, and are therefore not clearly distinguishable.

If obstacles are considered, it can be seen that the canyon averaged absorbed LW_{sky} is around the same value as LW_{trap} for H/W=0.5. There are

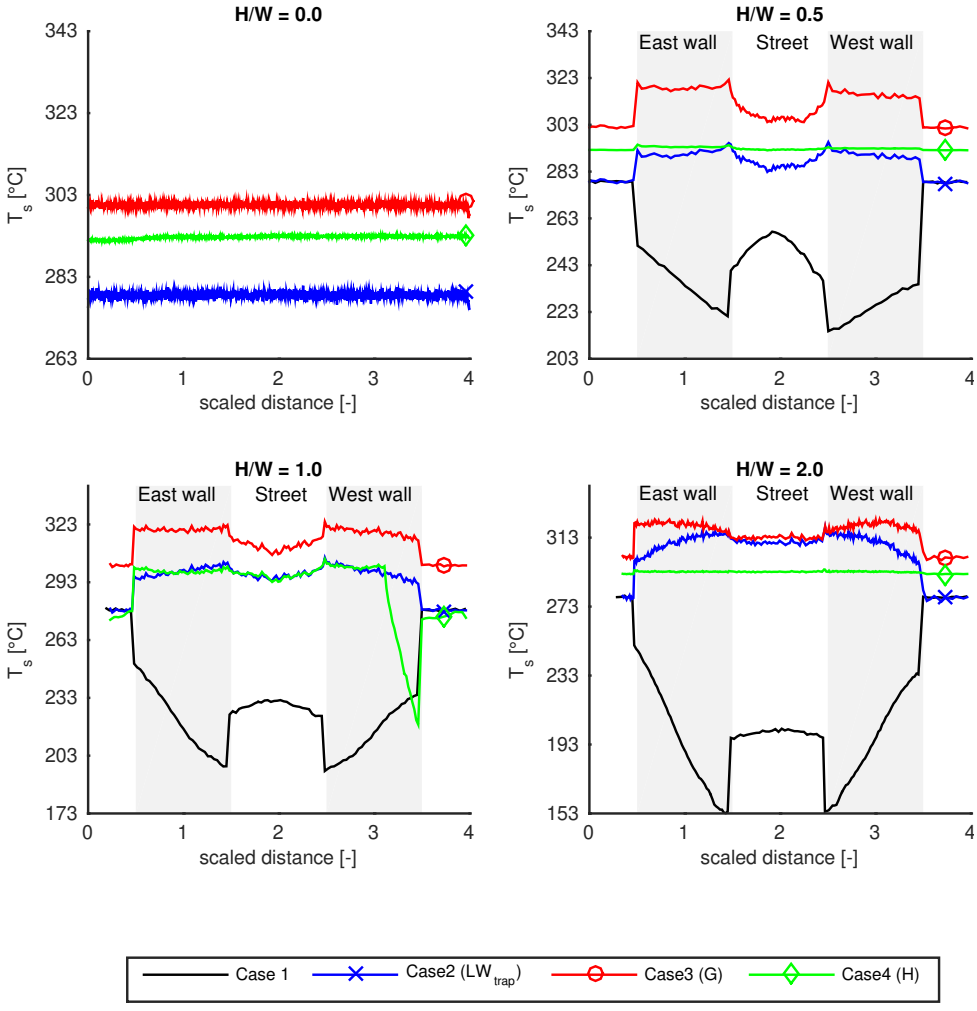

Fig. 2.8: Surface temperature for different H/W ratios (sub-plots) and cases (lines, see table 2.3). Note the different temperature scale for different H/W ratios.

however large spatial differences over the canyon, where longwave trapping is lowest in the center of the street, where absorbed longwave radiation from the sky is largest. The largest local difference between longwave trapping and absorbed longwave radiation from the sky is in the corner between the street and vertical walls, and exceeds 170 Wm^{-2}. With increasing H/W ratio, the absorbed longwave energy from the sky is decreasing over all surfaces. The longwave trapping effect is increasing, and is strongest at the corner between the street and vertical walls. The sensible heat flux and conductive heat flux play a much smaller role compared to radiation, and G and H are of the same order of magnitude. For H/W=1.0, the sensible heat flux shows a large peak at the corner between the west wall and roof, which also reduces the amount of LW_{out} at that location. The large peak in sensible heat flux is a numerical artefact, but due to the coupled energy balance, all other energy resources respond to this local disturbance.

In addition to plotting all processes for a single H/W ratio, the same results are also plotted for individual processes (sub-plots) and a range of H/W ratios (lines) (see Fig. 2.10). In this way, insight is gained in the contribution of processes to the surface energy balance with increasing H/W ratio. The reduced absorbed LW_{sky} displays a clear effect of building height, where absorbed radiation is decreasing with increasing H/W ratio. The emitted longwave radiation LW_{out} is fairly constant, except at the rooftop corner for H/W=1.0, which is a numerical artefact. Longwave trapping is increasing with increasing H/W ratio, similar to the radiation only case. The conductive heat flux shows some small changes over the canyon, but is generally quite invariant to changes in H/W ratio except for H/W=1.0. For H/W=1.0, changes in the conductive heat flux are found of 80 Wm^{-2} between roof level and the center of the street. For H/W=0.0, the conductive heat flux is around 15% of the absorbed longwave radiative energy for H/W=0.0 and reduces to 10% of the absorbed radiative energy for H/W=2.0 (canyon averaged conductive heat flux). These numbers are similar to De Bruin and Holtslag (1982), who showed a ratio of 10% based on observational data obtained from grassland at Cabauw (The Netherlands).

The sensible heat flux is close to 0 for H/W=2.0 over the canyon, indicating that the air temperature is very close to the surface temperature. For lower H/W ratios, there is a slight cooling effect of the sensible heat flux.

2.3.5 Air temperature

By using a CFD model to compute the sensible heat flux, also the wind speed and air temperature inside the street canyon are obtained for case 4

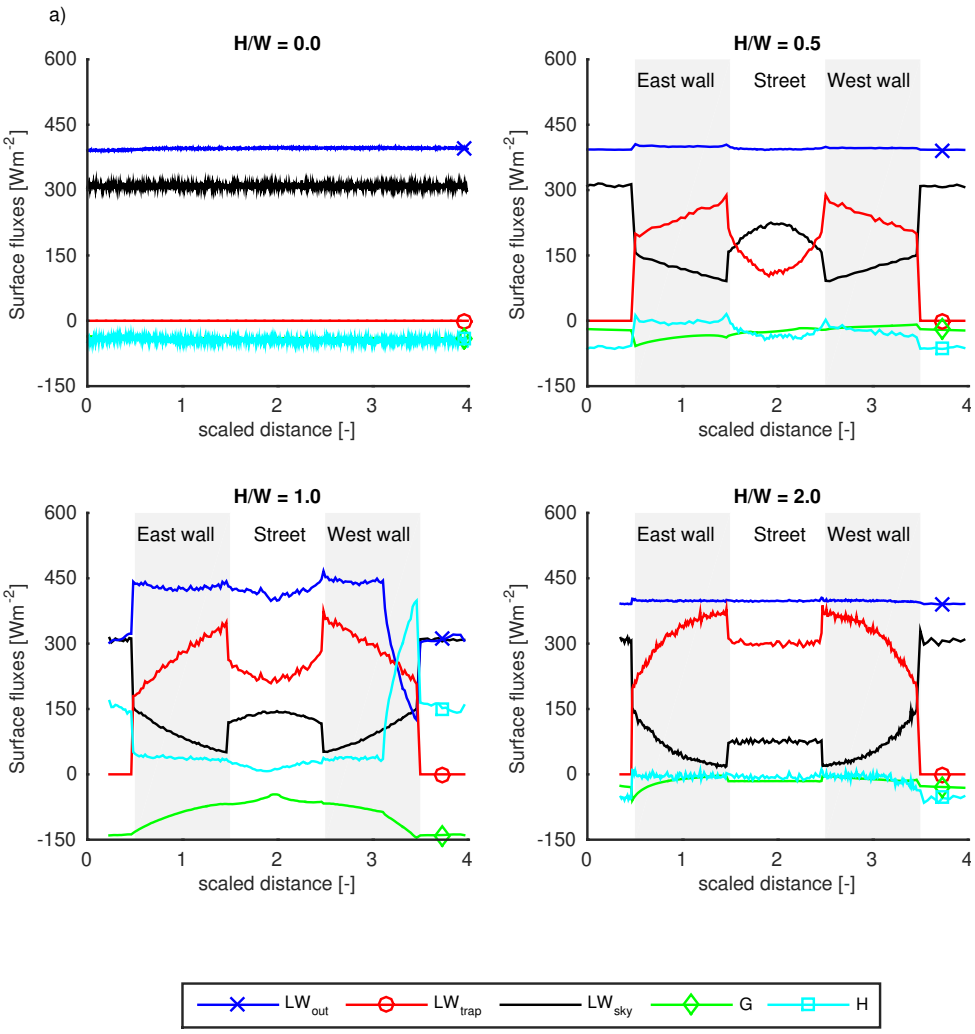

Fig. 2.9: Surface heat fluxes (lines) for different H/W ratios (sub-plots) for case 4 (including all physical mechanisms). Positive values of LW_{out}, G and H indicates extraction of energy from the surface (cooling tendency), while positive values of LW_{sky} and LW_{trap} indicate a heating tendency.

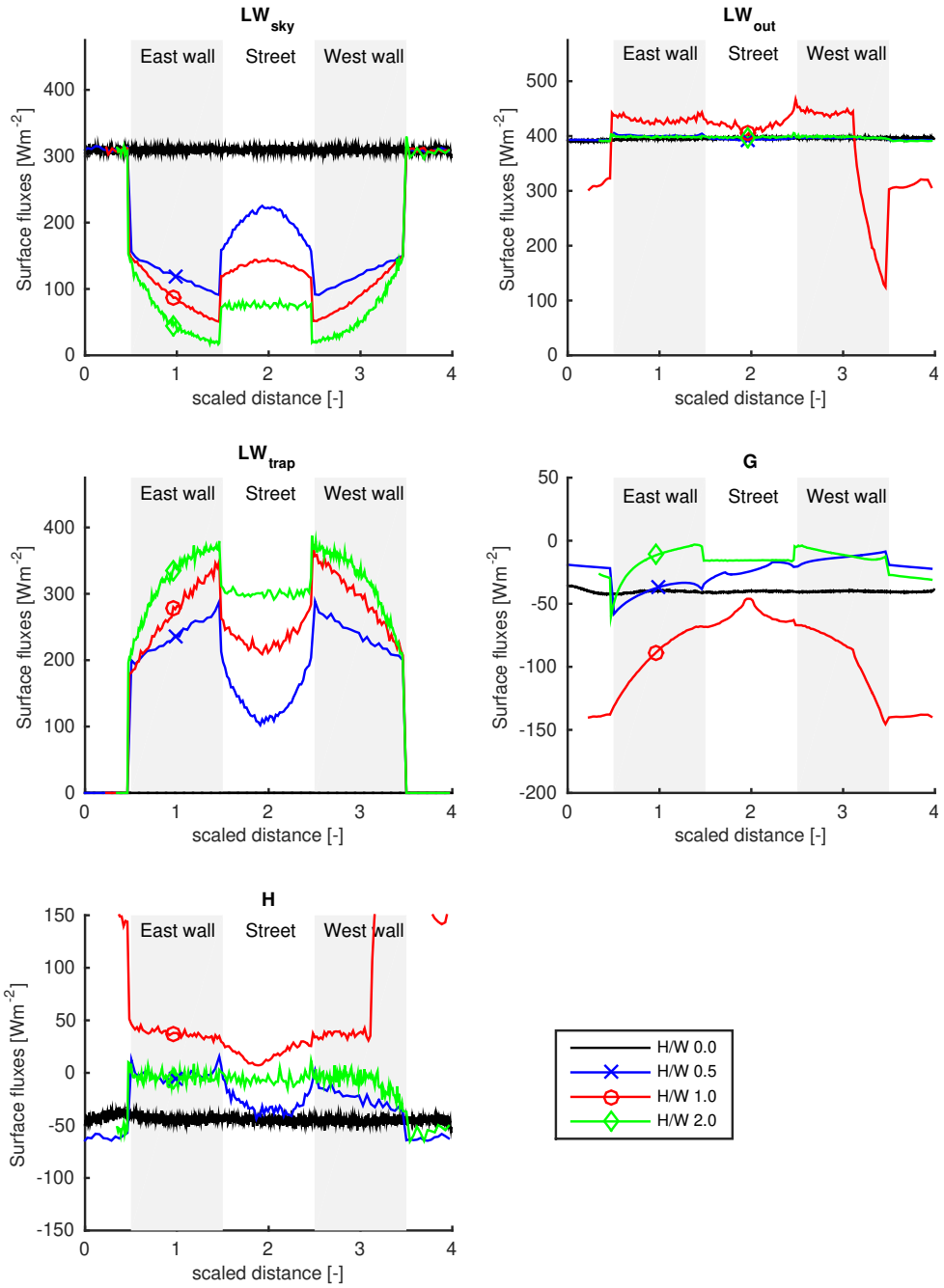

Fig. 2.10: The same surface heat fluxes shown in Fig 2.9, but now for different H/W ratios (lines) and different H/W ratios (sub-plots). Note the different range on the vertical axes for each sub-plot.

(the case including all physical mechanisms). Air temperature contours and velocity vectors are shown in Fig. 2.11.

There is mixing below obstacle height resulting in smaller temperature gradients with height, which was also observed in experiments by Uehara et al. (2000). Air temperature inside the canyon for H/W=0.5 and H/W=2.0 are slightly higher than ambient air, while for H/W=1.0 air inside the canyon is slightly lower than ambient air. For all H/W ratios there is one single rotating vortex inside the street canyon.

2.4 Model assumptions

To put the results in perspective, several simplifications in the case set-up and numerical model need to be discussed. The most obvious simplification is our 2D assumption of the urban geometry. This assumption has a large influence on the ventilation effect, where mixing of air is limited through the top of the canyon. When a 3D situation is considered, there will be outflow of air along the sides of the building and thus enhanced mixing. This limits the model to cases where 3D effects are small (e.g. long canyons with low H/W ratio). In addition to this simplification, only a limited domain size is used (1km) which might not allow for the development of a fully developed urban heat island, the albedo is constant in this study, the anthropogenic heating effect is not taken into account and constant input values for free stream air temperature and wind speed are used.

In addition to these simplifications in case set-up, there are also possible improvements in the used model. Firstly, it is known that CFD models can have trouble with strongly buoyant flows. It might be worthwhile to investigate a Large Eddy Simulation (LES) approach, although this comes with additional computation costs.

A second point that could be improved is our assumption of 1D heat conduction. This is valid if the temperature-gradients in the span-wise direction are small, which is not the case on the boundary between shaded and sun-lit part. In these regions, there will also be heat conduction alongside the walls, redistributing the conductive heat flux.

Finally, the longwave radiation from the sky could be improved. In the current model the assumption is that all longwave radiation is emitted at the top of the domain with a sky emissivity. In reality, canyon air locally absorbs and emits longwave radiation. This could reduce the differences that are found in air temperature inside the street canyon, since the warmer patches of air would emit more energy, which in turn is absorbed at other, colder,

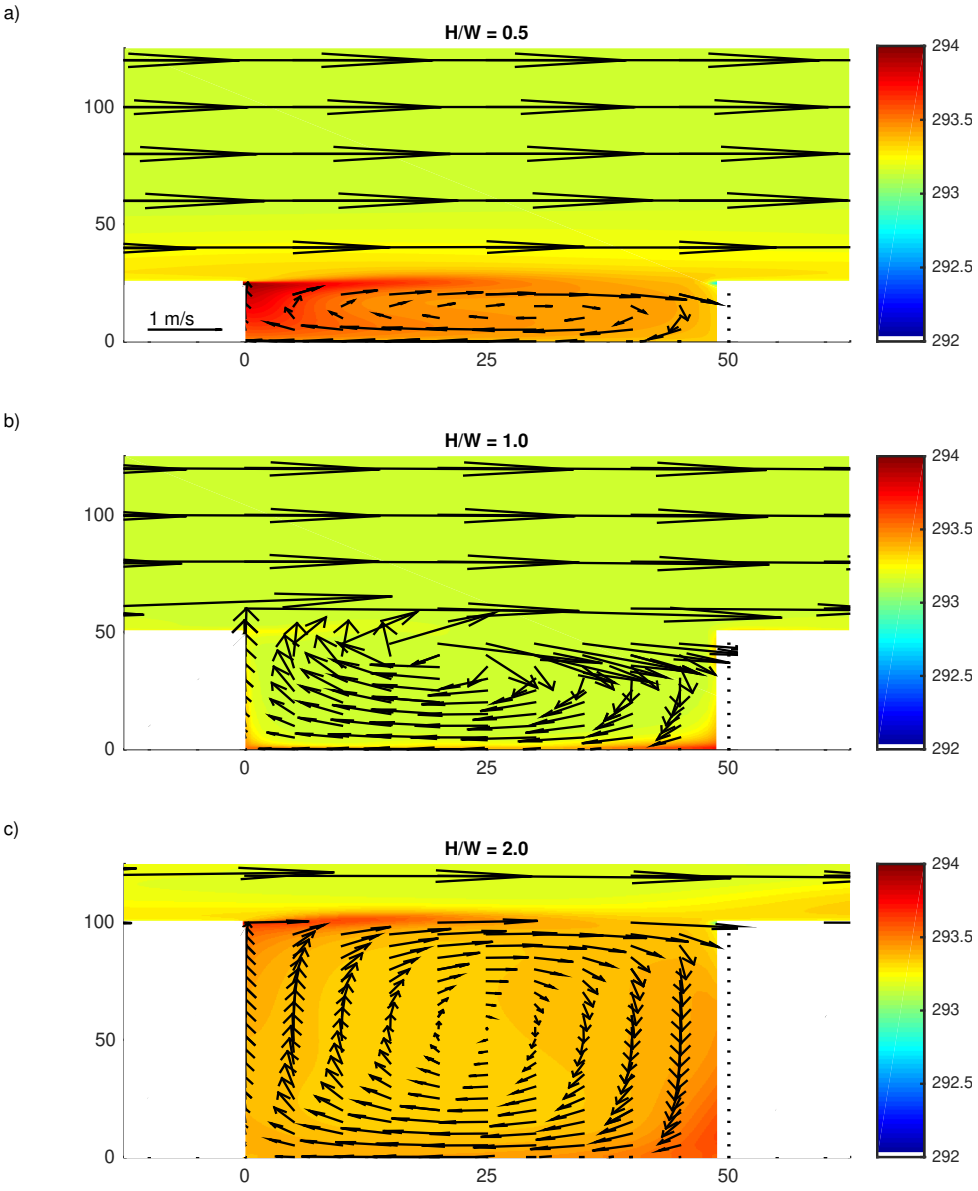

Fig. 2.11: Velocity vectors and contours of air temperature in the street canyon between obstacles 12 and 13 (see Fig. 2.5) when obstacles are present. Velocity vectors are all scaled equally, but note the different color-axis for different H/W ratios. Case 4 including all physical mechanisms is shown here.

locations.

2.5 Corrigendum to the original submission

This chapter is based on the publication of Schrijvers et al. (2015). The numerical model that was described and used in the original submission did not scale longwave trapping correctly with the local cell size. Within this chapter, these erroneous results have been corrected and results without this programming error are presented. These results supersede the results presented in the original journal submission. A corrigendum has been published to update the results for the deep canyons Schrijvers et al. (2020b).

2.5.1 Source of the programming error

The programming error that was found erroneously scaled the longwave trapping effect for the cell size area. In the original submission, a non-uniform cell size was used of 1 m^2 at ground level and roof level, and cells could expand 5% with each next grid cell over the vertical walls. The maximum cell size for H/W=2.0 is 3.0 m^2 in the middle of the canyon. Due to the programming error, radiation from longwave trapping was not scaled properly to Wm^{-2} with the cell area ratio. This resulted in an underprediction of the longwave trapping effect when cells are not exactly 1 m^2. For shallow canyons, cells are close to 1 m^2, and the programming error did not have such a large influence.

2.5.2 Changes in the results

With increasing H/W ratio, the relative contribution of longwave trapping to the urban energy budget is increasing, instead of decreasing as presented in the original submission. In case of radiative equilibrium, the presence of buildings locally increase the surface temperature compared to a flat terrain. The increase in longwave trapping exceeds the reduction of LW_{sky}. The increase in longwave trapping directly influences all other processes in the surface energy balance, where the longwave trapping effect strongly prevents surface cooling, especially in the lower parts of the canyon. The conductive heat flux raised surface temperature further, while the sensible heat flux showed a small cooling trend.

The increase in longwave trapping leads to heating of the air temperature compared to the ambient air for H/W=2.0, instead of the very stable stratification that was observed in the original manuscript. It was hypothesized that the very strong stable stratification was due to our 2D assumption. Our hypothesis is thus not (fully) correct, but the strong stable stratification was

formed due to a programming error.

2.5.3 Sensitivity to skin layer value

As mentioned in section 2.15, a skin layer $\Delta_{\text{skin}}\rho_{\text{skin}}C_{\text{v,skin}}$ is used with value of 0.01 $\text{JK}^{-1}\text{m}^{-2}$ in order to prevent large changes in surface temperature from one time step to the other. Even though this is a practical solution, it may not be fully correct. A better way to couple the net flux at the surface F to the surface temperature is by using the approach by Suter (2019)

$$\frac{\partial T_s}{\xi} = \frac{F}{\lambda} \tag{2.17}$$

with ξ the direction perpendicular to the surface, F the net energy at the surface and λ the conductivity of the ground or obstacle.

At this stage of the work, it is not possible to implement this new boundary condition. In order to quantify the influence of the skin layer, a sensitivity study has been conducted for H/W=0.5, where the skin layer is changed by 10% from 0.010 $\text{JK}^{-1}\text{m}^{-2}$ to 0.009 $\text{JK}^{-1}\text{m}^{-2}$ and 0.011 $\text{JK}^{-1}\text{m}^{-2}$. Results for the diurnal cycle in the centre of the canyon at the ground surface are shown in Fig. 2.12 for the surface temperature and Fig. 2.13 for the sensible heat flux and conductive heat flux. For brevity, the skin layer value is denoted in the legend with τ.

Using a skin layer with value of 0.011 $\text{JK}^{-1}\text{m}^{-2}$ shows large deviations compared to the other two calculations, both for the surface temperature and the fluxes. There are large jumps in surface temperature for one time step to the next, which can be as large as 2 K at midday. From the surface fluxes, the surface energy balance has not reached an equilibrium over the last three simulated days days, where the sensible heat flux and conductive heat flux are continuously increasing over time.

The differences between simulations using a skin layer of 0.010 $\text{JK}^{-1}\text{m}^{-2}$ and 0.009 $\text{JK}^{-1}\text{m}^{-2}$ are small. At midday, the difference in surface temperature is 0.1 K. For the sensible and conductive heat flux, differences are 0.7 Wm^{-2} and 0.2 Wm^{-2} respectively. At mid-night, the difference in surface temperature is 0.0 K, and for the fluxes 0.1 Wm^{-2} for both the sensible and conductive heat flux.

An increase in the skin layer thus results in a numerically unstable system, with large fluctuations per time step. The difference between a value of 0.01 $\text{JK}^{-1}\text{m}^{-2}$ and 0.009 $\text{JK}^{-1}\text{m}^{-2}$ is small.

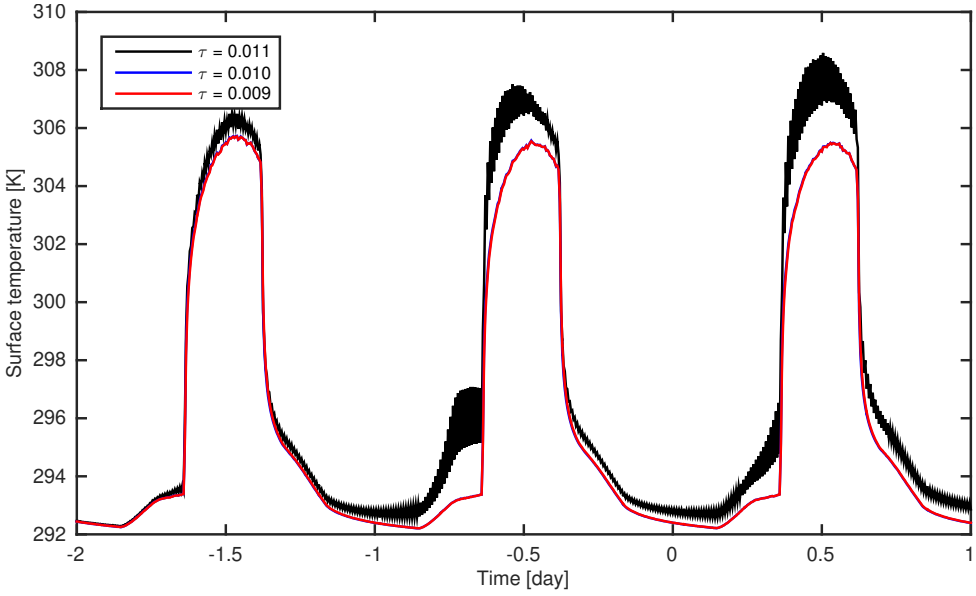

Fig. 2.12: Diurnal surface temperature in the middle of the ground surface for a canyon with H/W=0.5 and different values of the skin layer τ

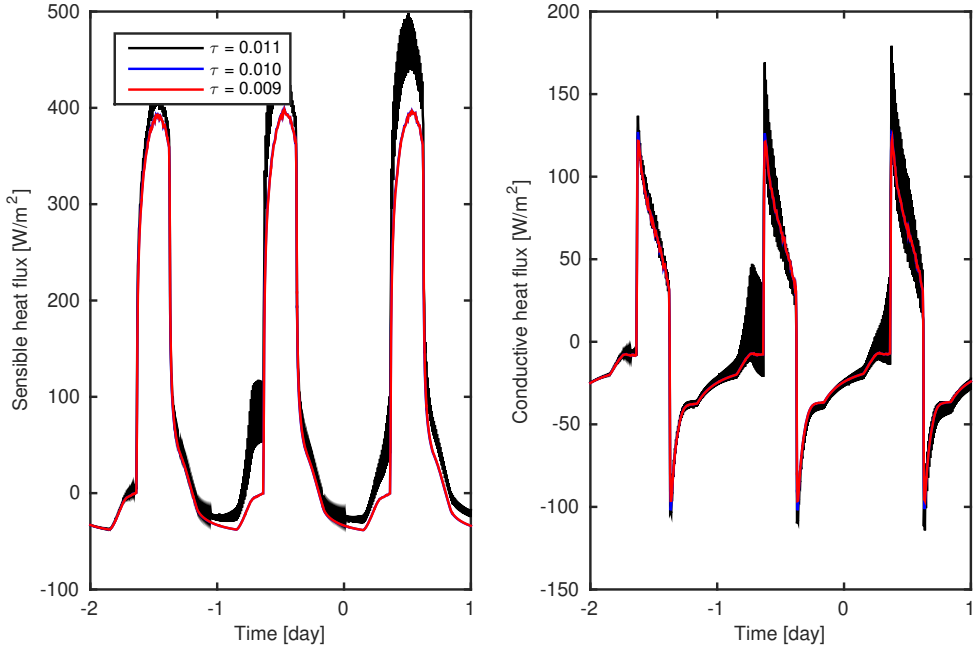

Fig. 2.13: Diurnal sensible and latent heat flux in the centre of the ground for a canyon with H/W=0.5 and different values of the skin layer τ

2.5.4 Conclusions of the erratum

Within the original submission, it was stated that longwave radiation is the main source of energy to the urban energy budget. This remains the case, and is even strengthened with the new results. Longwave trapping is the main contribution to the nighttime urban energy budget in our study. A very stable stratification was found for H/W=2.0. It was hypothesized that this is due to the 2D geometry that is used, that results in a strong stable stratification. The new results do not show this stable stratification, due to the increase in longwave trapping at the lower part of the canyon. One comment that was made in the original submission is that there is a subtle and complex interplay between all processes. This remains the case with the new results, which demonstrated that one small programming error can cause drastically different results. Therefore, it remains vital that all physical processes are taken into account as accurately as possible.

2.6 Conclusions

A systematic 2D conceptual study has been performed which aims at identifying dominant factors that are involved in the nighttime urban heat island energy budget at building level. A new transient simulation program has been developed which combines a Monte-Carlo radiative transfer model, conductive heat flux through the 1D heat conduction equation and convective heat transport by solving the transient RANS equations. Different H/W ratios have been considered as well as different physical mechanisms.

Results showed that buildings have a heating contribution to the surface temperature if only radiation is taken into account. The reduced sky view factor reduces the amount of absorbed LW_{sky}, while the longwave trapping effect (radiation emitted by a surface and absorbed at another surface) increases absorbed radiation. The reduction in LW_{sky} is smaller than the increase in longwave trapping, and the longwave trapping is becoming relatively stronger for increasing H/W ratios.

If surface temperature is considered, it was demonstrated that longwave trapping strongly prevents surface cooling, especially in the lower parts of the canyon. The conductive heat flux raised surface temperature further, while the sensible heat flux showed a small cooling trend.

In addition to surface temperature, the magnitude of all processes are studied for the case including all physical mechanisms. Canyon averaged longwave trapping is in the same order of magnitude as absorbed radiation from the sky (LW_{sky}) for H/W=0.5, but trapping is the main source of energy

for deeper canyons. The conductive heat flux is around 15% of the absorbed radiation for H/W=0.0 and decreases to 10% for H/W=2.0 due to the strong increase in longwave trapping. The contribution of the conductive heat flux is similar to the 10% that was found by De Bruin and Holtslag (1982) for a grass land. Sensible heat flux was shown to be almost zero in the lower parts of the canyon.

The increase in longwave trapping leads to in heating of the air temperature compared to the ambient air for H/W=0.5 and H/W=2.0. For H/W=1.0 no heating of the air temperature was observed.

2.7 Acknowledgment

This study is funded by the Dutch Climate Proof Cities consortium, which is part of the Knowledge For Climate program (knowledgeforclimate.climateresearchnetherlands.nl/climateproofcities).

Chapter 3

On the daytime micro-climatic conditions inside an idealized 2D urban canyon

Abstract[1]

This study investigates the surface temperature, air temperature and mean radiant temperature inside an idealized 2D street geometry during daytime. The goal is to unravel the relative impact of radiative transfer, heat conduction and ventilation to the urban heat budget. A building-resolving simulation model has been used, which represents these processes at a 1m spatial resolution. Different combinations of the canyon height to width ratio (H/W) and physical mechanisms are investigated. Shortwave radiation is the main source of energy, and for small H/W can be higher at the canyon ground level compared to flat terrain due to the occurrence of multiple reflections. The longwave trapping effect has the second largest contribution and becomes relatively more important with increasing H/W ratio. The influence of the interior building temperature (either a fixed temperature of 20°C or a zero-flux boundary condition) is small. Surface temperature and mean radiant tempera-ture are closely related, since both are largely controlled by radiative properties. No straightforward relation was found between surface temperature and air temperature, since air temperature is dependent on the competing mechanisms of forced and natural convection. All processes are modelled in high detail in this study, and a small urban heat island is observed. Including all these processes results in large computational requirements. In order to make the step to 3D, radiation can be computed using the view-factor approach instead of the expensive Monte-Carlo method.

[1]Published in Building and Environment (2019) with H.J.J. Jonker, S.R. de Roode, S. Kenjereš

3.1 Introduction

During clear nights with weak winds, cities tend to be 1 to 10°C warmer than the surrounding rural environment at night. This phenomenon has been observed for both small and large cities, in the tropics as well as in colder regions, and is called the Urban Heat Island (UHI) effect (Oke, 1981; Klysik and Fortuniak, 1999; Kim and Baik, 2004; Grimmond, 2007; Steeneveld et al., 2011). However, the daytime UHI effect is much smaller (Taha, 1997; Klysik and Fortuniak, 1999) and can even be negative, even in cold climates (Ryu and Baik, 2012). Furthermore, the daytime and nighttime UHI can have different distribution patterns and intensities over relatively short distances of less than 1km, as was found from measurements by Soltani and Sharifi (2017). This also holds for surface temperatures and mean radiant temperature, which is a quantity indicative of the human thermal comfort. The mean radiant temperature only depends on radiation, and is used in the computation of apparent temperatures like the Physiological Equivalent Temperature (PET, Höppe (1999)) and the Universal Temperature Climate Index (UTCI, Fiala et al. (2012)). Because of the higher temperatures, radiation, and thus heat load, human comfort in the city is more critical during daytime as compared to the night.

Klysik and Fortuniak (1999) studied the daytime atmospheric UHI effect of the town Lodz in Poland by using fixed point measurements from a weather station in the city centre over two different periods of three years. They found that on days with clear skies, there are large thermal contrasts within the city. In areas with narrow streets, the air close to the ground may be cooler than the rural environment due to shading of the ground surface. Klysik and Fortuniak (1999) state that the radiation and energy budget of roofs play an important role in that scenario. A warm layer of air can be formed at roof level, while the air inside the canyon remains cool due to the shading effect, creating a local inversion layer between canyon and roof level and limiting the vertical exchange of air in the street canyons.

In addition to air temperature, mean radiant temperature is also measured in dedicated field campaigns. Such measurements were conducted (amongst others) by Lindberg et al. (2008), who observed large local variations of mean radiant temperature. On a large open square in the city centre of Göteborg in Sweden, a peak value in mean radiant temperature of 57°C was found, which is on the threshold for moderate heat stress (Monteiro et al., 2012; Thorsson et al., 2014). In contrast, simultaneous measurements in a courtyard resulted in a mean radiant temperature of 17°C when shaded, which quickly raised to 27°C when the measurement location was directly sunlit. These measured

values are well below the threshold of moderate heat stress of 55°C, indicating the large impact of geometric properties and shading.

Even though the mean radiant temperature can be measured and the atmospheric UHI frequently observed, the urban UHI is a difficult phenomenon to interpret, due to its spatial inhomogeneity. When interpreting profiles of thermodynamic variables from a single measurement location, the effect of advection across the heterogeneous urban surface should also be taken into account, which is difficult to observe or quantify (Barlow, 2014). To overcome the local nature of measurements, numerical models can be used to study the urban environment, in which the complexity and non-linearity of the urban environment can be studied in a systematic manner. Often, these models apply on a larger scale (meso-scale) and the urban street canyon is parametrized. For instance, a meso-scale model (Weather and Research Forecasting model, WRF) coupled with a single-layer urban canopy model (SLUCM, (Kusaka et al., 2001)), was used by Ryu and Baik (2012). The building height (H =15 m) over street width (W =15 m) ratio (H/W) used was H/W=1.0. Their study indicated that during daytime the impervious surfaces (including the reduction in surface moisture availability and increased thermal inertia) contribute most to the urban heat island (+2.1°C). The 3D urban geometry (transfer of energy in vertical walls, shading, radiative trapping and reduction in ventilation) actually cools the city (-0.5°C).

Ryu and Baik (2012) used just a single H/W ratio, though it is known that this parameter has a large impact on the UHI effect (Oke, 1988).
Marciotto et al. (2010) investigated the influence of the aspect ratio and mean building height on local canopy energy fluxes by using an Urban Canopy Model (UCM) similar to Masson (2000). A north-south oriented canyon was used, and a full daily cycle was investigated. Results for one time-instance at midday (12:00) were discussed. Increasing the H/W ratio from 0.5 to 10.0, decreases the net radiation, as well as the sensible heat flux, by an amount of 120 Wm^{-2} (from 490 to 370) and 300 Wm^{-2} (from 360 to 60), respectively. The reduction in absorbed energy is compensated by the conductive heat flux, which transports energy towards the surface, and increases by 180 Wm^{-2}.

Theeuwes et al. (2014) differentiated the two compensating radiative effects in the urban canyon: shadow casting and longwave trapping. The net effect depends on the amount of available shortwave radiation penetrating the canyon. It was found that for H/W=1.0 the largest UHI effect is present. With increasing H/W ratio shading effects start to dominate over the longwave trapping effect during the day, and the UHI is decreasing.

All previously mentioned numerical studies used a meso-scale model in which the urban environment is parametrized. Therefore, results were obtained for the canyon as a whole, or for individual surfaces. When more spatial details are desired, smaller scale models are available that focus on the urban micro-scale. These include for instance Solweig (Lindberg et al., 2008), RayMan (Matzarakis, 2000), TUF-3D (Krayenhoff and Voogt, 2007) and envi-MET (Bruse, 1999). Hertel and Schlink (2019) developed a method for decomposing the urban heat island intensity at the neighbourhood scale. Envi-MET simulations are used as input, after which the surface energy balance is translated into temperature differences between two neighbourhoods. Unfortunately, no results were presented of a case study, nor validation of the model. In addition to the above models, generic Computational Fluid Dynamics (CFD) models are often applied in which surface temperature is prescribed and air flow is investigated. Toparlar et al. (2017) have performed an extensive review of CFD studies on the urban micro climate. They conclude that at present, CFD modelling results can be often validated from observations and CFD models are being increasingly applied for realistic case studies, including the assessment of the effect of adaptation measures. One specific example is Robitu et al. (2006), who used a coupled CFD, radiation and conduction model to investigate the effect of vegetation and ponds on the urban micro-climatic conditions. The presence of water ponds and trees improves the urban thermal comfort in summer during daytime by cooling the air and shading the urban surface. The influence of trees and ponds was not distinguished, nor the influence of trees and ponds on the different components of the surface energy balance.

Within the current study and Schrijvers et al. (2015), a new numerical model called URBSIM has been developed, which computes all processes at a 1 m spatial resolution at the canyon surface. The goal of the present study was to identify the mechanisms that control daytime surface temperature, air temperature and mean radiant temperature within a single canyon at a high resolution. As shown in the literature review, these processes are currently known for the canyon as a whole, thereby neglecting the spatial variability over a single surface. The processes taken into account are shortwave radiation, longwave radiation, conduction and turbulent transport of heat. Our objective was three-fold: 1) disentangle the mechanisms involved in the urban heat budget, 2) quantify the relation between surface temperature, air temperature and mean radiant temperature within a single street canyon, and 3) create insight for future studies into which processes can be parametrized at the urban micro-scale. The focus in this study was on the different processes and interactions, not so much on the most accurate representation

of the actual urban geometry. This was also reflected in our assumption of an idealized 2D geometry.

3.2 Methods and case set-up

The 2D micro-scale model URBSIM, that was discussed in Schrijvers et al. (2015, 2016) has been used. URBSIM couples a Monte-Carlo radiation model, 1D heat conduction equation for the conductive heat flux into buildings and the ground and a Computational Fluid Dynamics (CFD) model for the convective heat fluxes. In the present study, the 2D micro-scale model was extended with a new boundary condition for the interior building temperature, and mean radiant temperature can be routinely computed at any time and at any location. A 2D version of the model was used in order to simplify the geometrical complexity. A similar case set-up is used as in Schrijvers et al. (2015), and a range of H/W ratios were considered (0.0, 0.5, 1.0, 2.0). In addition to different canyon aspect ratios, also the inclusion of different physical processes were considered. Starting from a radiation only case, complexity was added by including the conductive heat flux and sensible heat flux. The canyon orientation is north-south, such that building facades are east-facing or west-facing. This is a typical orientation for 2D studies, and was also used in Schrijvers et al. (2015). A spatial resolution of 1 m was used at the building surface, and although a full diurnal cycle was modelled, here we only report the situation for a solar zenith angle of 28.9$^{\mathrm{o}}$ which corresponds to solar noon for the Netherlands at June 21. Details of the model and validation are discussed in Schrijvers et al. (2015), and only a brief description will be given here for convenience. Extensions of the model for this study are discussed in more detail.

3.2.1 Radiative transfer

Radiative transfer is computed by the Monte-Carlo model that was developed in Schrijvers et al. (2015), in which photon paths are computed for four radiative components: 1) diffuse shortwave radiation from the sky, SW_{dif}, 2) direct shortwave radiation from the sky, SW_{dir}, 3) longwave radiation emitted by the sky, LW_{sky} and 4) longwave radiation emitted by the surface, LW_{out} computed as:

$$LW_{\mathrm{out}} = \sigma \epsilon_{\mathrm{s}} T_{\mathrm{s}}^4 \tag{3.1}$$

with σ the Stefan-Boltzmann constant in [$\mathrm{Wm^{-2}K^{-4}}$], ϵ_{s} the emissivity of the surface and T_{s} the surface temperature in each grid cell in [K].

Note that reflection-events are not addressed separately; a photon emitted as direct radiation will be labelled SW_{dir} after a scattering event at the surface. The only exception is LW_{trap}, which is LW_{out} that is absorbed at another surface. Due to the 2D assumption, the solar azimuthal angle is not taken into account and only the solar zenith angle is used to describe the solar position. This means that the solar position is only described in the east-west plane, and that the north-south plane is discarded. The azimuthal angle is taken into account in the computation of the amount of incoming solar radiation at the top of the domain.

The photon packets trajectory is computed from cell face to cell face until a surface is hit. A fraction of the energy $(1 - \zeta)$ is absorbed at the surface, which is related to the albedo of the surface (shortwave radiation) and emissivity (longwave radiation). Note that radiation does not interact with the air inside the canyon, but only interacts at the surface.

The magnitude of the shortwave radiative flux is based on a parametrization proposed by Skartveit et al. (1998) and assuming clear skies. Maximum values for downwelling shortwave radiation and the constant value for LW_{sky} that are used at roof level, are shown in Table 3.1. Although LW_{sky} has a diurnal variation in reality, this is not taken into account in the current study. Kirchoff's law is assumed for broadband radiation, indicating that the same value is used for absorption (LW_{sky}) and emission (LW_{out}) of longwave radiation at the surface ($\alpha = \epsilon$).

3.2.2 Mean radiant temperature (T_{mrt})

The existing model has been extended to diagnose the mean radiant temperature, which is computed by

$$T_{\mathrm{mrt}} = \sqrt[4]{\frac{S_{\mathrm{str}}}{\epsilon_{\mathrm{p}}\sigma}} \tag{3.2}$$

where S_{str} is the local mean radiant flux density [Wm^{-2}] and ϵ_{p} the emissivity of the human skin, which is a constant independent of the application with a value of 0.97.

The mean radiant flux density can be regarded as the amount of radiation (both shortwave and longwave) that is absorbed by a person. It is computed following Thorsson et al. (2007)

$$S_{\mathrm{str}} = (1 - \alpha_{\mathrm{k}}) \sum_{n=1}^{6} SW_n F_n + \epsilon_{\mathrm{p}} \sum_{n=1}^{6} LW_n F_n \tag{3.3}$$

	Radiation
Emissivity ϵ	0.95
Albedo α	0.40
Latitude	52° 22' N
Longitude	4° 53' E
Start day	2012-06-10 00:00
End day	2012-06-18 23:59
max SW_{dir}	833.1 Wm^{-2}
max SW_{diff}	84.2 Wm^{-2}
LW_{sky}	325 Wm^{-2}
	Heat conduction
λ	0.72 $\mathrm{Wm}^{-1}\mathrm{K}^{-1}$
ρ	1920 kgm^{-3}
C_{v}	835 $\mathrm{Jkg}^{-1}\mathrm{K}^{-1}$
	Computational Fluid Dynamics
T_{a}	20°C
U	4.0 ms^{-1}
cell width	1.0 m

Table 3.1: Input constants for radiation, heat conduction into the urban material and the CFD model.

where n is the orientation (north, east, south, west, top, bottom), α_{p} is the albedo of the human body (with a standard value of 0.3), SW_n the total shortwave radiative flux in [Wm^{-2}], LW_n the total longwave radiative flux in [Wm^{-2}] and F_n a geometric factor representing a standing human body. A summation is performed over the 4 cardinal points (north, east, south, west), for which the geometric factor is set to 0.22 for each direction, while the geometric factor is set to 0.06 for radiation entering from the top and bottom (Lindberg et al., 2008). Since a 2D setting is used in this study, information is missing on the two faces that are occupying the sides of the canyon. These missing radiative fluxes are taken as the average of the two cardinal points that are available. This can physically be seen as computing mean radiant temperature on a square surrounded by obstacles.

3.2.3 Mean radiant temperature validation

The computation of T_{mrt} within the Monte-Carlo model is validated against values of the actinic flux from Madronich (1987). In that paper,

a derivation of the actinic flux (also called integrated density or flux density) is given and solutions are presented for the irradiance for direct and diffuse shortwave radiation.

Two cases are considered. In the first case direct radiation of 800 Wm^{-2} has been emitted with a solar zenith angle of 0 degrees onto a diffuse scattering surface with albedo α=1 (no absorption). For this configuration, the horizontal flux should be half of the incoming energy (400 Wm^{-2}). The left panel of Fig. 3.1 shows the horizontal and vertical flux directions, which show that the horizontal component is 400 Wm^{-2} (50%) of the incoming direct radiation. There are small spatial differences due to the Monte-Carlo method, which are around 2 Wm^{-2}. The averaged difference is 0.8 Wm^{-2} for the vertical components (0.1%) and 0.15% for the horizontal components. These differences decrease with increasing number of photons.

In the second simulation setup, diffuse radiation (100 Wm^{-2}) is emitted, for which Madronich (1987) derived that the irradiance is equal in all directions (this only holds for a perfect reflecting surface, with α=1). Results are shown in the right panel of Fig. 3.1, which shows an uniform distribution of 100 Wm^{-2} with fluctuations of 0.5 Wm^{-2}.

The Monte-Carlo radiation model performs well against the results by Madronich (1987), and as such will be used in the remainder of this study. The spatially averaged Monte-Carlo results are within 0.15% of Madronich (1987).

3.2.4 Conductive heat flux

The conductive heat transfer is computed using the temperature gradient inside the urban material (building walls and layers beneath the street)

$$G_i = -\lambda \frac{\partial T}{\partial x_i} \tag{3.4}$$

where λ is the thermal conductivity of the material in [$\mathrm{Wm}^{-1}\mathrm{K}^{-1}$] (see Table 3.1) and x_i the distance into the ground or building surface in [m]. The value of λ used in this study is that of brick, which is close to the thermal conductivity of asphalt and medium to dense concrete. Note that this is a highly simplified representation of the building walls, in which normally two layers of brick are used with a cavity in between. To simplify the problem, the cavity is not taken into account. Furthermore, no sensitivity study on other building materials is conducted, which is left for future work. The temperature profile is computed using the 1D heat conduction equation

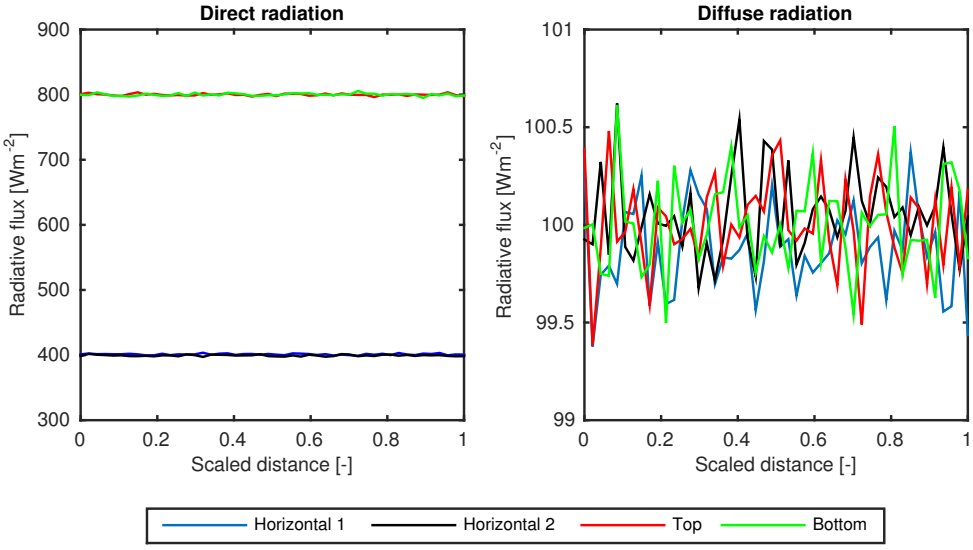

Fig. 3.1: Validation of radiative fluxes for two numerical tetsts against analytical results by Madronich (1987). Results show the horizontal flux (eastward and westward) for direct shortwave flux density for all directions and diffuse shortwave flux density for all direction. Input for the direct shortwave radiation is 800 Wm^{-2} and 100 Wm^{-2} for the diffuse shortwave radiation.

$$\frac{\partial T}{\partial t} = k_{\mathrm{d}} \frac{\partial^2 T}{\partial x_i^2} \tag{3.5}$$

where k_{d} is the thermal diffusivity in [$\mathrm{m^2 s}$], based on the conductivity λ, density ρ in [$\mathrm{kgm^{-3}}$] and specific heat C_{v} of the ground or obstacle in [$\mathrm{Jkg^{-1}K^{-1}}$].

$$k_{\mathrm{d}} = \frac{\lambda}{\rho C_{\mathrm{v}}} \tag{3.6}$$

Two different boundary conditions are used for the building interior. The first is a zero flux boundary condition at a distance of 1 m into the ground or 0.25 m into an obstacle. It was found that diurnal temperature cycle does not influence the interior temperature in the ground over more than 1 m, which is why this distance was used. The distance of 0.25 m for the fixed building temperature is based on the typical thickness of a building wall. Alternatively, a fixed interior temperature is used of 20°C at the same distance into the ground and obstacle. The choice of 20°C is based on a temperature inside a building that is comfortable. As a consequence of the zero-flux boundary condition, the interior building temperature follows from the absorbed radiation, sensible heat flux and conductive heat flux of previous time steps. With a constant, prescribed interior temperature, the energy inside the building is dissipated or generated, which can act as an unlimited source of energy. Physically, this can be seen as using an extremely efficient air-conditioning unit which is able to maintain the prescribed interior temperature. A time step of the global model is used of 6 minutes, except for the conductive heat flux where a time step of 1 second is used. The surface temperature of each grid cell is thus updated every 6 minutes. This will be discussed in more detail in section 3.2.7.

3.2.5 Computational Fluid Dynamics (CFD) model

Ventilation effects are computed by an in-house developed CFD model (Kenjeres and Hanjalic, 1999, 2006, 2009; Kenjeres and ter Kuile, 2013; Kenjeres et al., 2015). This model uses the Transient Reynolds-Averaged Navier-Stokes (T-RANS) equation to solve the wind field and air temperature distribution, and includes buoyancy effects.

The unknown Reynolds stresses $\overline{u_i u_j}$ [$\mathrm{m^2 s^{-2}}$] are computed using the $k-\varepsilon$ turbulence model, which relates the turbulent stresses to the turbulent kinetic energy k [$\mathrm{m^2 s^{-2}}$] and dissipation ε [$\mathrm{m^2 s^{-3}}$]. The model coefficients (C_μ, σ_k, σ_ε, $C_{\varepsilon 1}$, $C_{\varepsilon 2}$ and $C_{\varepsilon 3}$, see table 3.2) used are taken from the standard k-ε model, as often used for a wide range of turbulent flows in street canyons

C_μ	σ_k	σ_ε	$C_{\varepsilon 1}$	$C_{\varepsilon 2}$	$C_{\varepsilon 3}$
0.09	1.0	1.3	1.44	1.92	1.44

Table 3.2: Model coefficients used in the standard $k-\varepsilon$ turbulence model.

(Launder and Spalding (1974), Versteeg and Malalasekera (1995), Santiago et al. (2007)).

In addition to the velocity field, the temperature field is solved by using the T-RANS equations. The unknown turbulent heat flux $\overline{\theta u_i}$ [$\mathrm{ms^{-1}K}$] is computed using the Simple Gradient Diffusion Hypothesis, where the turbulent flux is related to the temperature gradient and the turbulent viscosity:

$$-\overline{\theta u_i} = \frac{\nu_\mathrm{t}}{\mathrm{Pr_t}} \frac{\partial T}{\partial x_i}. \tag{3.7}$$

with ν_t the eddy viscosity [$\mathrm{m^2s^{-1}}$], and $\mathrm{Pr_t}$ the turbulent Prandtl number (the ratio between the eddy diffusivity for momentum and heat transfer K_m/K_h), and is set to 0.86. Although the value of the turbulent Prandtl number depends on stability (Grachev et al., 2007; Li, 2019), we set $\mathrm{Pr_t}$ to 0.86 which is typically used in commercial CFD codes and is also in between the range between 1/3 and 1 commonly used in large-eddy simulation models for convective and stable conditions (de Roode et al., 2017).

The sensible heat flux at each individual surface grid cell is defined as

$$SHF_i = \rho c_\mathrm{p} \overline{\theta u_i} \tag{3.8}$$

where ρ is the density of air (1.208 $\mathrm{kgm^{-3}}$) and $\mathrm{c_p}$ the specific heat capacity of air (1004 $\mathrm{Jkg^{-1}K^{-1}}$). The sensible heat flux is computed based on the temperature gradient between surface and air in the neighbouring grid cell. The Boussinesq approximation is used, stating that density differences can be neglected except for the buoyancy term. Buoyancy effects are taken into account in the computation of the temperature field, and are therefore not specifically required in the computation of the sensible heat flux.

3.2.6 Integrated energy balance model

All sub-models compute a part of the total surface energy balance, which dictates that all fluxes should balance:

$$SW_{\mathrm{dir}} + SW_{\mathrm{dif}} + LW_{\mathrm{sky}} + LW_{\mathrm{trap}} = LW_{\mathrm{out}} + SHF + G \tag{3.9}$$

where SHF is the sensible heat flux (for SHF >0 there is heating of air) and G the conductive heat flux (for G >0 energy is added to the ground). The latent heat flux (evaporation of water) is not taken into account in this study. Multiple reflections of radiation are not addressed separately, but are included in the terms of SW_{dir}, SW_{dif} and LW_{sky}.

The controlling parameter for the surface fluxes is the surface temperature. A skin layer is assumed to prevent large variations in surface temperature in time

$$\Delta_{\mathrm{skin}}\rho_{\mathrm{skin}}C_{\mathrm{v,skin}}\frac{\partial T_s}{\partial t} = \Gamma \tag{3.10}$$

with Γ the flux imbalance resulting from the surface energy balance and $\Delta_{\mathrm{skin}}\rho_{\mathrm{skin}}C_{\mathrm{v,skin}}$=0.01 $\mathrm{JK^{-1}m^{-2}}$, which results from a very thin layer Δ_{skin}. This also creates an under-relaxation-factor, which helps to stabilize the simulation.

For a time step, all fluxes in the surface energy balance are computed based on the surface temperature of the previous time step in each building surface grid cell. This can result in a small flux imbalance Γ. Based on the flux imbalance and old surface temperature, the surface temperature for the new time step is computed. Surface temperature is thus not a fixed value, but interactive through all surface fluxes.

The time step of 6 minutes is used for the Monte-Carlo radiation model, CFD model and integrated model, while the conductive heat flux model uses a time step of 1 second. The time step of 6 minutes is based on the movement of the shadow: for the cases considered here, the shadow does not travel more than 1 grid cell per time step. Ideally, a smaller time step would be used for the CFD model, but this would increase computation times significantly.

3.2.7 Test cases and methodology

To study the effect of different physical processes as a function of the H/W ratio, an idealized 2D urban geometry has been used consisting of 10 obstacles which are spaced W=50 m apart. By using an array of obstacles, a fully developed flow pattern is found in the most downwind street canyons, which indicates that more obstacles would not change the flow in the next canyon. The establishment of a fully developed flow after multiple obstacles

has been obtained from a sensitivity analysis, and is confirmed by literature (Santiago et al., 2007; Memon et al., 2010). A uniform grid of 1 m is used. From sensitivity studies, it was found that for a convergence of the modelling results, a canyon should be covered by at least 20 x 20 cells to be grid independent. The total number of cells ranges between 400,000 for H/W=0.5 up to 1,500,000 for H/W=2.0. All buildings are B=25 m wide, while building height is varied between 0 m (H/W=0.0), 25 m (H/W=0.5), 50 m (H/W=1.0) and 100 m (H/W=2.0), see Fig. 3.2 for a schematic overview.

For the radiation modelling, periodic boundaries are implicitly used at the domain sides, such that radiation can only be absorbed at the building surface or reflected towards the sky. The CFD model uses an inflow boundary condition with a prescribed uniform inlet velocity, outflow boundary condition with a zero diffusion flux for all variables, symmetry boundary condition at the top of the domain which does not allow a vertical velocity gradient and no-slip walls at the ground and building surfaces.

In addition to changes in building height, different components of the surface energy balance are switched on and off. Instead of performing a full factor separation analysis like Ryu and Baik (2012) where all combinations of different processes were considered, the simplest case with only radiation is used as a starting point. From this basic case, complexity has been added by adding the conductive heat flux process with a zero-flux boundary condition (case 2) and sensible heat flux (case 3). The case including the sensible heat flux and fixed interior temperature is addressed separately.

Eight consecutive days were considered in the middle of June, which is the month where the sun is at its maximum zenith angle in the Netherlands. The simulated weather conditions correspond to sunny, cloud free weather. The maximum radiative components mentioned in Table 3.2 are a few tens of Wm^{-2} smaller than the maximum values observed in the Netherlands. By using eight days, quasi-steady state results are obtained that are independent on the initial conditions (the daily cycle is repetitive). For a point in the center of the canyon for H/W=1.0, differences between the last three days in the maximum surface temperature are below 1°C, while the maximum conductive heat flux differs by 3 Wm^{-2}. The inlet air has a velocity of 4 ms^{-1} and a temperature of 20°C and both are constant with height and time. The inlet wind speed of 4 ms^{-1} is used to avoid an urban heat island internal circulation that can develop in the presence of very weak background winds (Oke, 1995). The wind speed of 4 ms^{-1} is similar to the study by Draxler (1986), and leads to a wind speed above roof level of 2.5 ms^{-1} at the most downwind canyon, which is slightly lower than the 30 year average

wind speed in the month June at weather station De Bilt in the Netherlands (www.klimaatatlas.nl).

Both for daytime and nighttime, constant values in time and height are used for the inlet wind speed and air temperature. The reason for using these strongly idealized lateral boundary conditions, that ignore the diurnal cycle of wind and temperature, is to increase the understanding of the individual processes such as the radiative forcing on the surface energy balance. By using more realistic, time-dependent input parameters, differentiating the different processes from the input parameters becomes much more difficult, which would limit the insights gained from this study. The initial surface temperature is set to 27°C on all surfaces based on expected average surface temperatures over the complete canyon. In total, 8 diurnal cycles are simulated, such that the choice of the initial surface temperature does not influence the results. Other input parameters are shown in Table 3.2.

Fig. 3.2 illustrates how further results (Figure 4-7) are plotted, where all vertical surfaces are scaled to a length of 1. This allows us to compare different H/W ratios in a single plot. For H/W=0, the full domain is plotted (length of 1000m) which is plotted as a scaled distance from 0 to 4.

3.3 Results

Even though multiple diurnal cycles were computed, the results presented here only show the results for the last computed day and the time instance where the sun reaches its highest position. The last day has been used, to ensure that the initial conditions do not have an influence on the results, and the diurnal cycle is repetitive. For details on the diurnal cycle of surface temperature, the conductive heat flux and sensible heat flux, please see Schrijvers et al. (2015). The highest position of the sun is chosen, since radiation is strongest at this point in time, and will thus lead to the most clear relation between mean radiant temperature and surface temperature. Note that the sun is not directly overhead the canyon, such that there is shading of the west-facing wall.

3.3.1 Case with radiation only

The first case considers radiative equilibrium. Since there is no conduction or convection, this situation implies that all absorbed radiation should be emitted through longwave radiation. This case acts as the reference case, from which the effect of including additional process can be determined. Absorbed longwave radiation from the sky is shown in Fig. 3.3a, and is

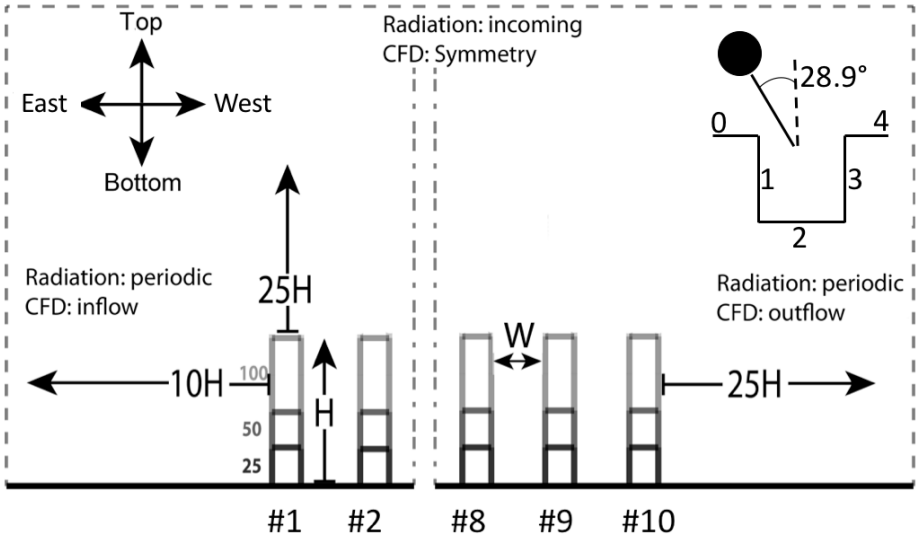

Fig. 3.2: Schematic of the case set-up with changing H/W ratio. Ten buildings are spaced W=50 m apart, while building height (H) is varied. Plotting is done according to the inset in the top right, which also includes the solar position with zenith angle of 28.9°. Building orientation is shown in the top left, surface 1 is denoted as 'west-facing', surface 3 is denoted as 'east-facing'.

decreasing with increasing H/W ratio due to the reducing sky-view factor. For a flat terrain (H/W=0.0) fluctuations are seen in the absorbed radiation. This is due to the Monte-Carlo method, where a finite number of photons are emitted. As a result, each grid cell receives a slightly different amount of energy. The fluctuations are decreasing when more photons are emitted, but this comes at a cost of increasing computation time. These fluctuations are also seen when buildings are included.

Fig. 3.3b shows the absorbed longwave radiation that is emitted by the buildings and the ground surface. This longwave trapping effect shows an asymmetric pattern that is due to the differential solar radiative heating of the canyon surfaces. The sunlit surface is warmer, emits more radiation and therefore the longwave trapping effect in the corner between the street and sunlit wall is higher.

For H/W=0.5 and H/W=1.0, longwave trapping peaks at the corner between the ground and the east-facing wall. Trapping in the corner between the ground and the east-facing wall is higher compared to the corner with the west-facing wall, since surface temperature in the east-facing wall corner is higher, and thus there is more emitted longwave radiation. With increasing H/W ratio, there is less variation in the longwave trapping. With higher buildings, longwave radiation progresses towards two infinite plates that are facing each other, where there is a uniform distribution. The corners are of less importance for these larger H/W ratios.

The total absorbed shortwave radiation (direct and diffuse component) is shown in Fig. 3.3c. The trapping effect due to multiple reflections can be observed at the ground level, where the absorbed shortwave radiation exceeds that of the flat terrain for H/W=0.5 and H/W=1.0. The shadow location on the ground can also be observed, where H/W=1.0 shows a larger shaded area of the ground surface as compared to H/W=0.5. For H/W=2.0, the street level is completely shaded.

Due to our assumption of radiation as the only transport means of heat, the total of all the absorbed radiative fluxes balances the emitted longwave radiation. This is shown in Fig. 3.3d, which displays a clear peak in emitted radiation for H/W=0.5 and H/W=1.0 at the lower corner between the ground and the east-facing wall, where emitted longwave radiation exceeds that of the flat plate. The longwave trapping effect and the absorbed shortwave radiation have approximately the same magnitude, while the magnitude of the absorbed longwave radiation emitted by the sky is much smaller. There is an imbalance over the canyon of 60 Wm^{-2}, which is due to the time stepping algorithm, where the emitted longwave radiation is based on the

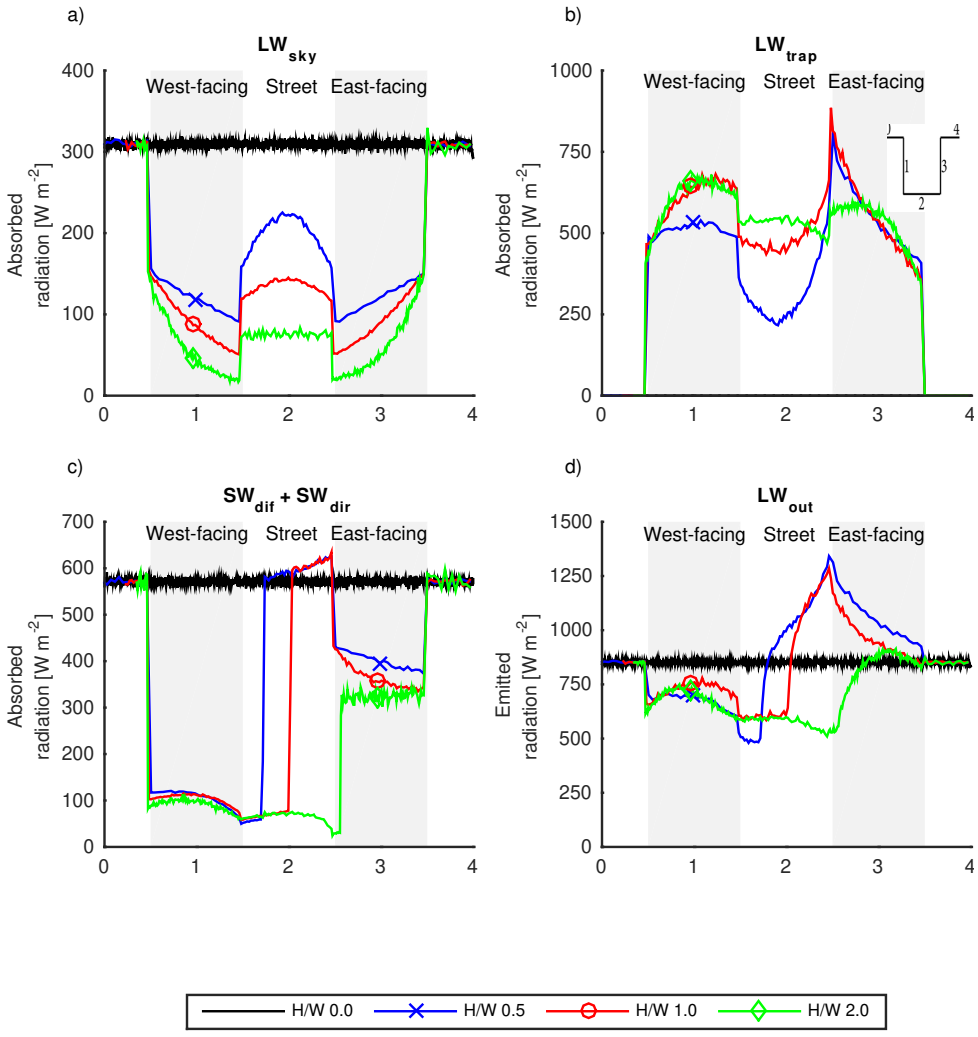

Fig. 3.3: Absorbed longwave radiation emitted by the sky, absorbed radiation due to longwave trapping, total absorbed shortwave radiation and emitted longwave radiation by walls in case of radiation only (case 1). Plotting follows the inset at the top right, except for a flat plate. Note the difference in scaling on the vertical axis for each plot.

surface temperature computed in the previous time step. For H/W=2.0, the lowest emitted radiation is in the corner between the street and the east-facing wall, at 500 Wm^{-2}, with the total absorbed radiation at roof level at 800 Wm^{-2}.

3.3.2 Surface temperature

From the radiation only case, more physical processes are added to study their effect on the surface temperature. For the radiation case, the surface temperature of a flat plate becomes very high at about 82°C (see Fig. 3.4a). Note that this is not a prescribed surface temperature, but its high value follows directly from the balance between the absorbed and emitted radiation. These temperatures are in line with Garratt (1992), who suggested that surface temperatures in the vicinity of 90 to 100°C may occur for dry darkish soils of low thermal conductivity (0.1-0.2 $\mathrm{Wm^{-1}K^{-1}}$), considering a simplified form of the surface energy balance equation, utilizing likely upper values of absorbed shortwave flux (1000 $\mathrm{Wm^{-2}}$) and screen air temperature (55°C).

If the conductive heat flux process is added, energy is transferred into the ground, reducing its surface temperature by 20°C. The inclusion of the sensible heat flux allows for another energy transfer from the solid surface to air which even further reduces the surface temperature by 30°C.

If obstacles are added, the effects of shadow casting (lower surface temperatures on the west-facing walls) and multiple shortwave reflections (higher surface temperature on the ground and the east-facing wall compared to the flat terrain) are clearly demonstrated for obstacles with H/W=0.5 and H/W=1.0 (Figs. 3.4b and 3.4c, respectively). The impact of multiple reflections is smaller for deeper canyons, where only a portion of the east-facing wall is directly illuminated. Surface temperatures at the ground level exceed these of the flat terrain, due to the longwave trapping effect, which is 750 $\mathrm{Wm^{-2}}$ in the corner between the street and the east-facing wall. In the absence of conduction and sensible heat fluxes this additional radiative energy causes excessively high surface temperatures of about 120°C.

The addition of the conductive heat flux influences the sunlit and shaded part of the canyon differently. In the shaded areas, the conductive heat flux has only a small effect. For H/W=2.0, the conductive heat flux has the smallest influence. Note that a zero-flux boundary condition is used deep inside the obstacle and the ground, of which the impact will be discussed later.

The inclusion of the sensible heat flux filters out surface temperature differences for H/W=0.5, where the temperature differs from 32°C close to the east-facing wall to 20°C at the corner between the west-facing wall and roof. For H/W=1.0, the highest surface temperature is located in the corner between the east-facing wall and the ground. A sharp decrease in surface temperature is found at the top corner. This is due to a local very high turbulent viscosity (ν_t), which is directly influencing the sensible

heat flux following from Equation 6. It is known that the standard $k-\varepsilon$ model computes too high values of turbulent kinetic energy at stagnation points (Durbin, 1996). The too large value of turbulent viscosity is directly increasing the sensible heat flux. The Durbin time-scale limiter τ may be applied, which bounds the turbulent viscosity and therefore also the turbulent heat flux (Durbin, 1996). Note that the same effect is also present for the other H/W ratios, but to a lesser extent. For $H/W = 2.0$, surface temperature is almost uniformly distributed, with temperature differences between 21 and 26°C.

3.3.3 Surface fluxes

The surface temperature plots reveal, in a qualitative sense, which processes are more important. To get a more quantitative view, all individual fluxes are plotted in Fig. 3.5. In this plot, all absorbed radiation entering from the sky (SW_{dir}, SW_{dif} and LW_{sky}) is combined. Also note that positive values of LW_{out}, G and SHF indicate a cooling tendency of the surface.

For the flat plate (Fig. 3.5a) the absorbed radiation contributes 900 Wm^{-2} to the surface, while 450 Wm^{-2} is emitted through LW_{out}. The energy surplus is compensated by the sensible heat flux (375 Wm^{-2}) and the conductive heat flux (50 Wm^{-2}). At this moment in time, there is a flux imbalance of 25 Wm^{-2}.

When cases including obstacles are considered, absorbed radiation remains the largest contribution in the sunlit areas, although its relative contribution decreases for high H/W ratio, which was also shown in Fig. 3.3. The incoming shortwave radiation is divided over a larger surface area, which results in lower surface temperatures. The longwave trapping effect remains larger than the conductive or sensible heat flux. Compared to absorbed radiation from the sky, the longwave trapping is increasing for increasing H/W ratio.

The conductive heat flux shows very small contributions at the west-facing wall and the top part of the east-facing walls. Only at the location where the absorbed radiation peaks, the conductive heat flux is significantly transferring energy into the canyon material. The addition of the sensible heat flux shows a small cooling tendency of the west-facing walls. For H/W=0.5, the sunlit parts of the street and the east-facing wall shows a much larger cooling effect, where energy is extracted from the warmer surface. For H/W=1.0 (Fig. 3.5c), the sensible heat flux at the ground surface is almost zero, which indicates that the temperature differences between the surface and the adjacent air are very small. The sharp peak in the sensible heat flux

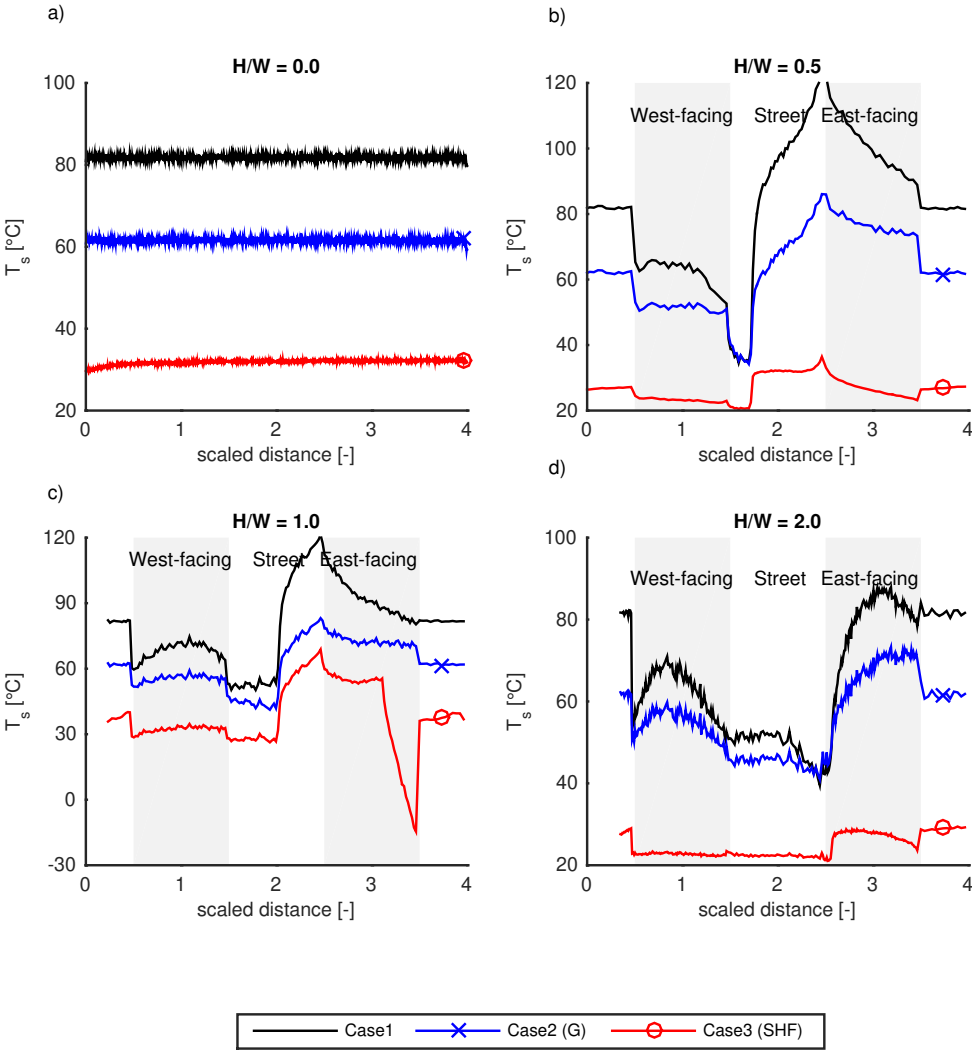

Fig. 3.4: Surface temperature for different H/W ratios (sub plots) and different cases (coloured lines). Different vertical scales are used in each plot to better visualize the temperature differences.

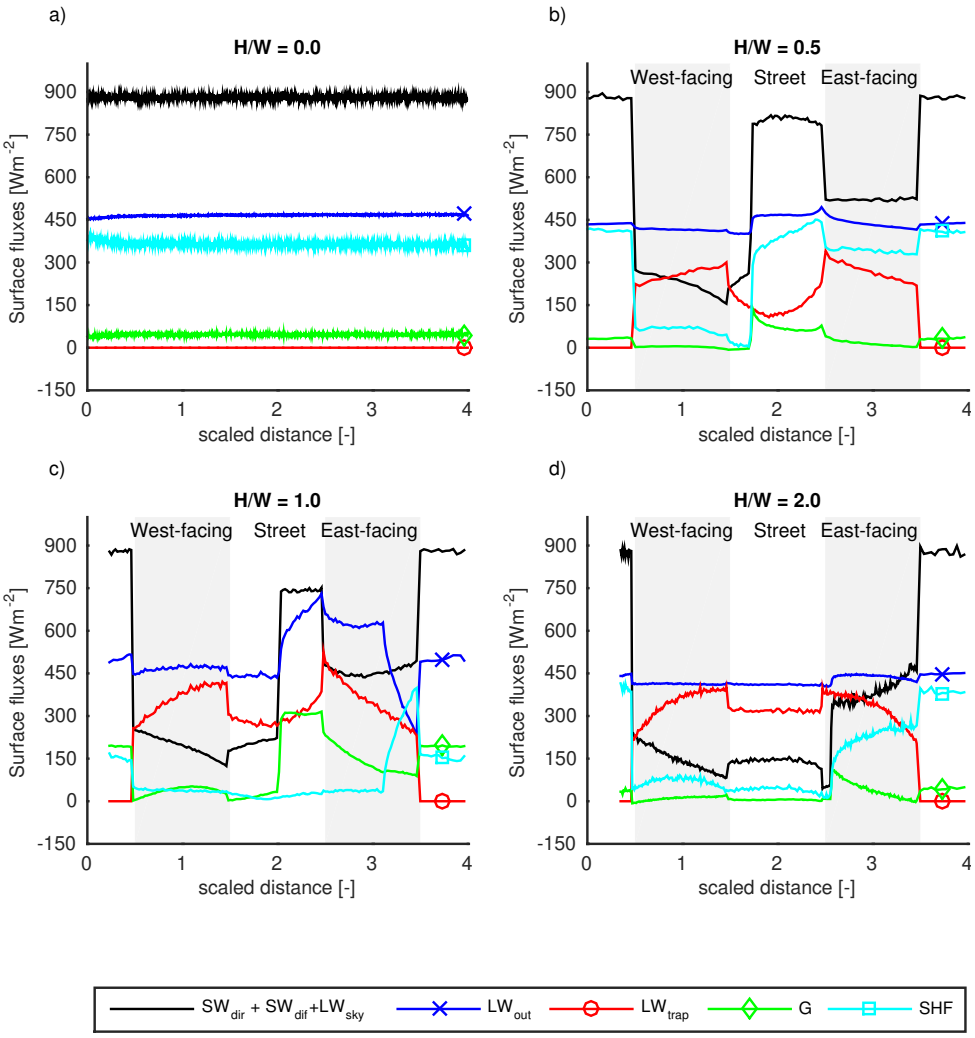

Fig. 3.5: Surface fluxes for different H/W ratios (sub plots) and physical processes (coloured lines) for case 3 (including conductive and sensible heat flux, but excluding latent heat flux). The same scale is used for all plots.

is clearly seen at the top corner between the roof and the east-facing wall, which is reducing the emitted longwave radiation directly. For H/W=2.0, sensible heat flux increases from 5 Wm^{-2} at the ground level to 250 Wm^{-2} at the corner between the roof and the east-facing wall, and is generally larger than the conductive heat flux contribution.

3.3.4 Air temperature

Air temperature and velocity vectors for Case 3 are shown in Fig. 3.6. For H/W=0.5, a warmer canyon is observed as compared to the free stream air temperature, and one single vortex is present. This is in contrast with results by Sini et al. (1996), who found a second vortex in the lower left corner in the absence of buoyancy forces. The non-uniform heating of the canyon in the present study suppresses the formation of the second vortex. However, in our model simulations a small second vortex becomes present only if the buoyancy force is switched off. This result (not shown here) hints at a subtle effect of the non-uniform canyon heating on the suppression of the second vortex. From the east-facing wall, air is heated by the surface and forced towards the west-facing wall, where the highest air temperature is found. Air temperature inside the canyon is 1.5°C higher than ambient air, which is comparable in magnitude to measurements from Giovannini et al. (2013), who found temperature differences up to 2°C for H/W=0.85.

For H/W=1.0 (Fig. 3.6b), a similar pattern of the flow structure is observed compared to H/W=0.5, but with lower air temperatures. Air is locally heated close to the surfaces, with a slightly larger region in the corners where the wind speed is low. Warm air is transported from the west-facing wall upwards towards roof level, and from there dispersed to the centre of the canyon due to the free stream air flowing over the top. The temperature distribution within the canyon for H/W=1 is remarkably different as compared to the other two examples shown for H/W equal to 0.5 and 2, respectively, in the sense that only a relatively small layer of warm air is found near the ground surface. For H/W=1 the relatively warm air is more efficiently transported out of the canyon.

Similar to H/W=0.5, a warmer canyon than the free stream air is seen for H/W=2.0, with an average air temperature of 20.1°C. Air temperature inside the canyon is rather uniformly distributed, with slightly higher temperatures along the east-facing wall. One single vortex is seen, but velocity inside the canyon is low. Other studies also presented a double vortex when one side of the canyon is heated, which is not observed here. These studies often apply uniform heating on one vertical wall, with typical temperature differences between two surfaces of 5°C or 10°C. In the present study, the application of an energy balance model at the solid surfaces lead to a non-trivial surface temperature distribution. Therefore, buoyancy forces are not constant inside the canyon, which can alter the formation of a double or single vortex structure. Further study is required to fully grasp the influence of these non-uniform temperature distributions and when the vortex structure

changes inside the canyon. An extensive analysis of air flow in deep canyon (H/W=2.1) is provided in the study by Offerle et al. (2007). Measurements were conducted over a range of seasons and primarily analysed for sunny days. A distinction was made on warmer windward and leeward walls in combination with wind directions. When the leeward wall is heated, heat transfer is concentrated near the wall, resulting in vertical transport of heat and less mixing. When this buoyant flow encounters the cross-canyon flow and the shear layer at the canyon top, the different flow layers become well mixed, such that this buoyant flow will be recirculated. Even though there is no cross flow in the present study, the mixing of the shear layer at the canyon top is also observed here. Note that the measurements by Offerle et al. (2007) indicate a weaker influence of buoyancy effects compared to several reported numerical studies.

3.3.5 Influence of interior boundary condition

The zero-flux boundary condition for the conductive heat flux calculations implies that the interior temperature will be determined by the net radiation and the sensible heat flux. To investigate the impact of a zero-flux boundary condition on the results, we have performed a sequence of simulations for H/W up to 1.0 with another boundary condition in which a fixed interior temperature of 20 °C is prescribed.

The surface temperature is plotted in Fig. 3.7, and compares the Case 3 (including sensible heat flux, but with a zero-flux boundary condition) to the same case but with a fixed T_g. For H/W=0.0, the difference between the two boundary conditions is about 1°C, where the fixed T_g provides a lower surface temperature. For H/W=0.5, there is only a small difference in the surface temperature of about 0.5°C on the east-facing wall resulting from the use of the two different boundary conditions. For all other surfaces, there is no distinctive surface temperature difference when changing the interior boundary condition. For H/W=1.0, the case with the fixed interior temperature provides a higher surface temperature, by 2°C. Furthermore, the decrease in the surface temperature towards the top of the east-facing wall is smaller. The fixed interior temperature is able to extract more energy from the surface into the urban material, compared to the zero-flux boundary condition.

In general, the differences between the two boundary conditions (fixed interior temperature and zero flux) are small, provided that a reasonable estimate is given for the interior temperature. Fig. 3.8 compares the individual surface fluxes for H/W=1.0. Differences are below 10 Wm^{-2} for the

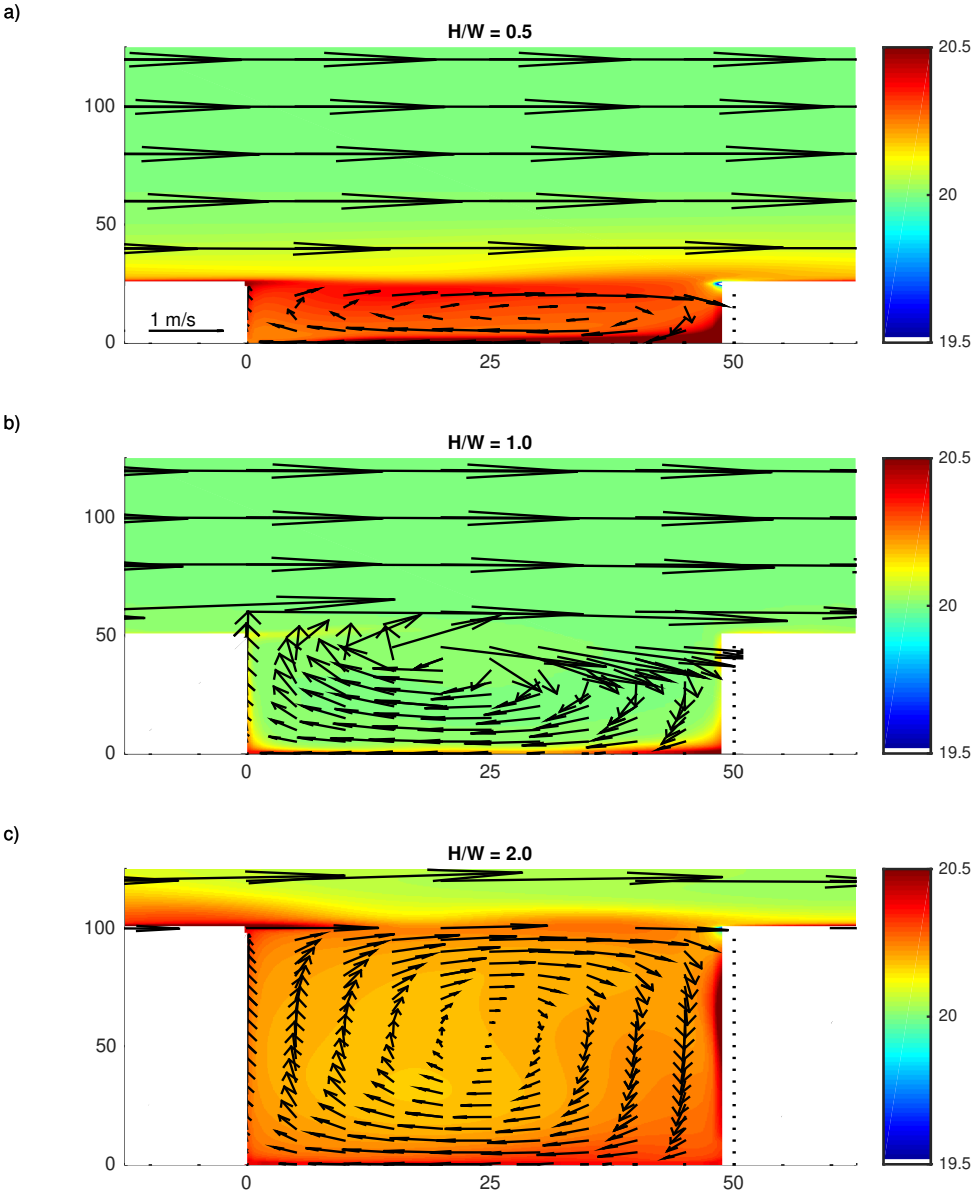

Fig. 3.6: Absolute air temperature (°C) and velocity vectors for Case 3 for different H/W ratios. The x-axis presents the distance from the west-facing wall in meters. Note the different length scales on the horizontal and vertical. A reference vector of 1ms^{-1} is shown on the bottom left of panel a.

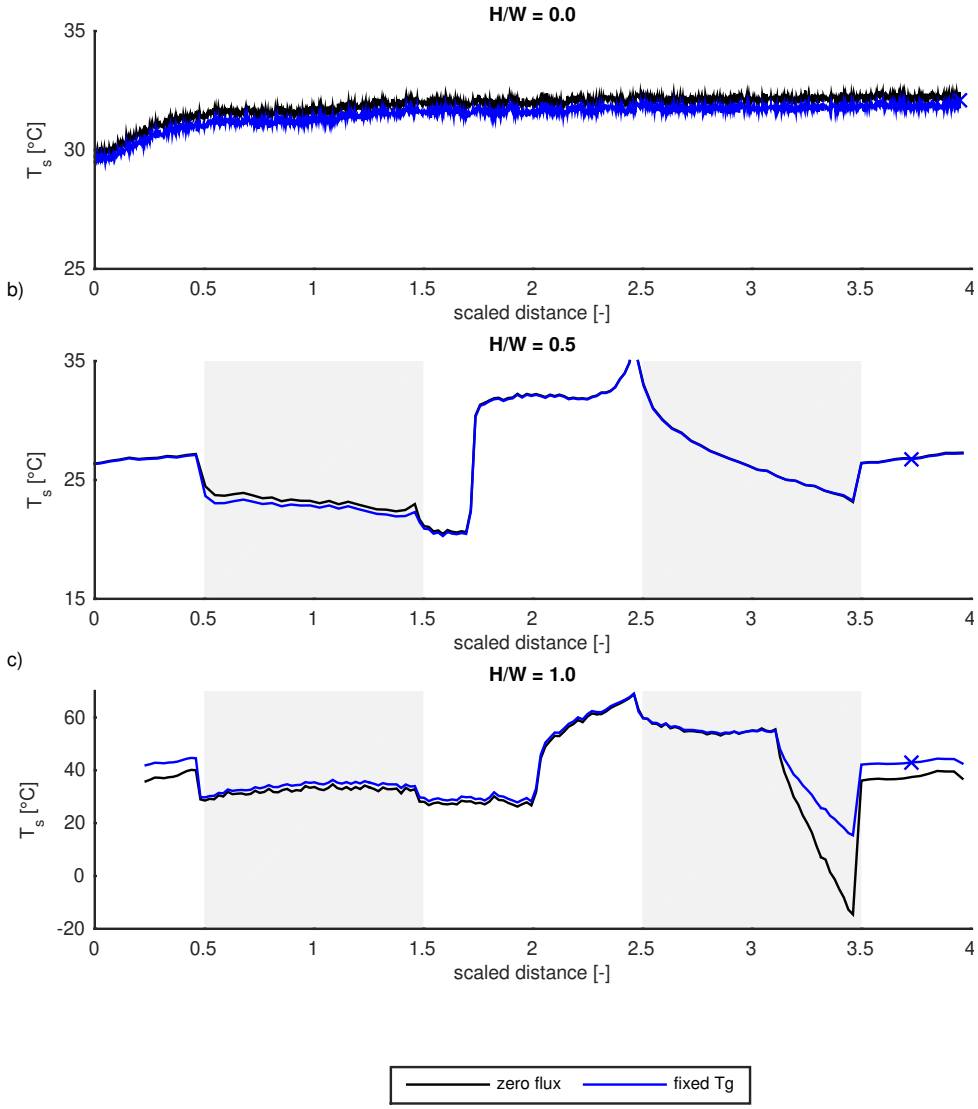

Fig. 3.7: Surface temperature for different H/W ratios (sub plots) for case 3 (including conductive and sensible heat flux, with a zero flux boundary condition) and the same case but with a fixed interior temperature T_g of 20°C.

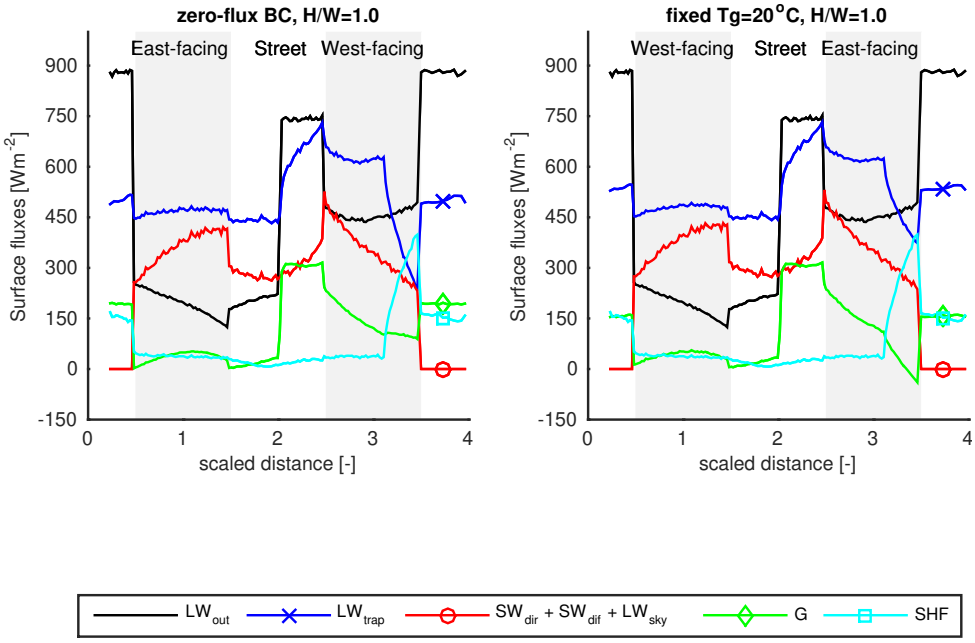

Fig. 3.8: Surface fluxes for H/W=1.0 for case 3 (including conductive and sensible heat flux, with a zero flux boundary condition) and the same case but with a fixed interior temperature T_g of 20°C.

conductive heat flux, except for the corner between the east-facing wall and the roof.

Despite the small differences observed in the surface temperatures and fluxes in this study, the fixed interior temperature can act as an unlimited source of energy, forcing surface temperature towards the prescribed building interior temperature. The large impact of the indoor temperature on the outdoor environment has also been demonstrated by Theeuwes et al. (2014) who studied the UHI with the WRF model, and showed a range of the UHI between 2 and 7°C when changing building temperature from 5 to 23°C.

The interior temperature boundary conditions therefore can be used as a 'tuning parameter' in which one can steer the model results by prescribing the desired interior temperature. For instance, when in the validation case the surface temperature is too low, one can prescribe a higher interior boundary temperature to 'solve' the problem. By using a zero-flux boundary condition, there is no user input, and the results cannot be controlled by the user to obtain the desired solution. Therefore, the choice was made to use the zero-flux boundary condition as the default option in this study.

3.3.6 Mean radiant temperature

The mean radiant temperature at a height of 2 m is shown in Fig. 3.9. For the flat plate (H/W=0.0), a mean radiant temperature of 69°C is found. The threshold for moderate heat stress is at 55°C, while strong heat stress is experienced above 60°C (Monteiro et al., 2012; Thorsson et al., 2014), indicating that very strong heat stress is experienced. Inclusion of obstacles below H/W=1.0 results in large spatial variations due to shading in this case. The mean radiant temperature in the sunlit part exceeds that of the flat terrain due to multiple reflections and longwave trapping and peaks at 90°C for H/W=1.0 (extreme heat stress), while a value of 45°C is found in the shade (no thermal heat stress). For H/W=0.5, a lower mean radiant temperature in comparison to H/W=1.0 is found, but extreme heat stress is observed over a larger region due to a smaller shaded area. For H/W=2.0, there is no sunlit part of the canyon at this height, and the mean radiant temperature is much more uniform and around 30°C. The highest temperature is found near the west-facing wall, due to solar reflections from the east-facing wall.

For H/W=2.0, a nearly constant surface temperature at the ground level is found. Surface temperatures for H/W=1.0 are higher at the ground level compared to H/W=0.5, especially in the sunlit area. The same is also seen in the mean radiant temperature. However, the mean radiant temperature is not only a function of surface temperature, but also of sky-based radiation (both shortwave and longwave). There is a thus a clear relation between the change in surface temperature and mean radiant temperature, although linking absolute temperatures show a less trivial relation.

3.4 Discussion

3.4.1 Results

Results in this study showed that for all H/W ratios the surface energy budget is strongly controlled by radiative terms. With increasing H/W ratio, the longwave trapping effect and conductive heat flux become relatively more important. This is similar to the findings by Marciotto et al. (2010), who found the largest contribution from the net radiation (all absorbed and emitted radiative terms combined) for H/W=0.5, while for H/W=10.0 the conductive energy flux becomes almost equally important compared to the net radiation.

Mean radiant temperature showed large spatial changes due to shadow locations, where mean radiant temperature is up to 10°C higher compared

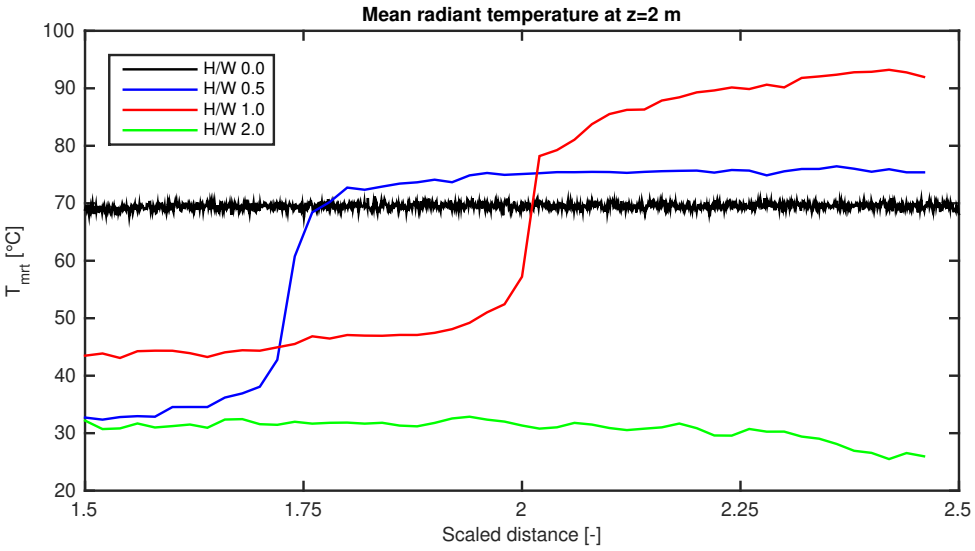

Fig. 3.9: Profiles of mean radiant temperature at z=2m height between buildings 8 and 9 for case 3.

to air temperature in shaded areas and up to 70°C higher in sunlit areas. Similar results were found by Ali-Toudert and Mayer (2006), although the mean radiant temperature in the sunlit part in their study is about 10°C lower than in our study.

The large impact of radiation on the urban energy budget, in particular for low H/W ratios, allows for a relatively simple link between mean radiant temperature and the surface temperature. The strong relation between surface temperature and mean radiant temperature is exploited in the modelling approach followed by simulation models Solweig (Lindberg et al., 2008) and RayMan (Matzarakis, 2000), in which the computation of the surface temperature is parametrized but accurate results are obtained for mean radiant temperatures. This study indicates that for H/W=2.0, the sensible heat transfer becomes more important compared to the conductive heat flux, which is highly parametrized in both Solweig and RayMan. This might compromise the accuracy of these models for deep canyons.

The addition of a CFD model in URBSIM gives insight in the impact of surface temperature on the air temperature. There is a complex interplay between forced convection (free stream air) and natural convection. Different vortex dynamics inside a canyon as a function of surface temperature have also been found by Magnusson et al. (2014) who found two vortices for a canyon with H/W=2.5. When the leeward wall of the canyon was heated,

the weak lower vortex disappeared and one vortex remained. However, these simulations where conducted with a fixed surface temperature, without feedback from warmer/colder air on the surface.

3.4.2 Model deficiencies

URBSIM has been developed with the goal to reduce the amount of assumptions that are made for modelling the urban micro-scale. Therefore, a Monte-Carlo radiation model and CFD model were used, which represent the physical processes as detailed as possible. The model results show a small increase in the air temperature inside the canyon for H/W=0.5 and H/W=2.0 as compared to the ambient temperature above roof level. These results appear physically sound. However, a weakness of the model is the representation of the dynamics near roof corners, where the CFD model produces a too large value for the turbulent viscosity (Durbin, 1996), which in turn directly affects the turbulent heat flux and reduces the surface temperature locally.

In order to take all processes into account in such high detail, the urban geometry is highly simplified by only taking into account a 2D street canyon. Taking into account a full 3D urban geometry would be computationally too expensive. Within URBSIM, it is assumed that if building arrays are much longer than their height, they can be considered to be 2D. Santamouris et al. (1999), Coronel and Álvarez (2001) and Giovannini et al. (2013) performed measurements in canyons with ratios L/H of the building length L to the height H in the range between 1.25 to 5.5, and found significant 3D effects on the air flow. All of these measurements observed that flow characteristics inside the canyon are either due to circulatory vortices or finite canyon length effects that are related to 3D flow patterns. These findings indicate that even with very long canyons, 3D effects are present, which are absent in the 2D model used in this study.

In addition to the 2D assumption, there is the effect of temporal variations. Although the whole diurnal cycle is computed, the current paper only focussed on the situation at one time instance. Especially the conductive heat flux shows large diurnal variations. Results shown here are therefore always a function of the situation of the previous time-steps. The large diurnal variations have been reduced in this paper by considering highly idealized conditions, such as a symmetrical 2D street canyon, constant inlet wind speed and air temperature, and a fully developed flow in the canyon of consideration.

Despite these assumptions, calculations are expensive and require substan-

tial amounts of computation time. A similar observation was made by Robitu et al. (2006). Therefore, the step to a 3D URBSIM program is not yet possible, and model simplifications must be made. The two most expensive computations are the sensible heat flux (CFD model) and the radiation (Monte-Carlo method). For the sensible heat flux computation, no suitable alternatives are present at the moment, that compute the airflow inside the canyon and handle the complex balance between forced convection and buoyancy forces. For the radiation model, a simpler model is available using view factor algebra. Especially for these simple urban canyon configurations, computation times for the radiative components using the view factor approach should be small, providing very similar results to the Monte-Carlo method. One limitation using view factor algebra is that only a limited number of reflections are typically taken into account (one or two reflections). Therefore, the radiation scheme is the most likely candidate to reduce the computation time, without deteriorating the results.

One process that has not been investigated in this study is the latent heat flux, which is extracting energy from the urban canyon through evaporation of water. Taking into account the latent heat flux requires one additional parameter in the CFD model (humidity) and a water balance on the building surfaces. As Theeuwes et al. (2017) demonstrated with the aid of a diagnostic equation, the inclusion of the vegetation fraction (directly relating to the latent heat flux) is required to accurately compute the city-scale UHI effect.

3.5 Conclusions

This study focussed on the daytime micro-climatic conditions inside an idealized 2D canyon. A building-resolving simulation model has been used, which includes key physical processes like radiation, conduction and ventilation by air flow at a 1 m spatial resolution. A range of canyon height to width (H/W) ratios and physical processes are considered.

Results showed that the daytime energy budget is strongly controlled by radiation, where absorbed radiation from the sky (SW_{dir}, SW_{dif} and LW_{sky}, including their multiple reflections) is the main source of energy at the surface, followed by trapped longwave radiation (energy emitted from the surface and absorbed at another location). The radiative components are, however, decreasing with increasing building height, while the conductive heat flux is increasing. Mean radiant temperature increased locally for H/W ratios of 0.5 and 1.0 compared to a flat plate. This is due to increased multiple reflections of shortwave radiation and longwave trapping. For deeper canyons, there is no direct sunlight reaching the street level, and mean radiant

temperature drops quickly.

The link between surface temperature and mean radiant temperature can be made (at least from a quantitative point of view) relatively easy, since both are largely dependent on radiative fluxes. This relation allows for simplified models, where the computation of the surface temperature is parametrized but accurate results are obtained for mean radiant temperatures (Lindberg et al., 2008; Matzarakis, 2000). The link between surface and air temperature is much harder to make. Air temperature inside the canyon is determined by a complex competition between forced convection (which is a function of free stream wind speed) and natural convection (buoyancy forces). This makes it difficult to develop a parametrization that holds for all H/W ratios and on every individual canyon surface.

The model used in the present study takes all processes into account in high detail, where the input of the user has been minimised as much as possible. The down-side of this approach is that calculations are costly and time-consuming, and the same approach can't be extended to 3D environments due to the large computational requirements of the CFD model and the Monte-Carlo model, in which the number of emitted photons would increase drastically. For these simple building shapes, the Monte-Carlo model may be replaced by a much faster view-factor model.

Furthermore, coupling to a large scale model, such as presented in the overview paper by Chen et al. (2011) could be pursued to allow for more detailed meteorological input conditions. Instead of using constant parameters as done now, a diurnal cycle in air temperature and wind speed could be used.

3.6 Acknowledgment

This study is funded by the Dutch Climate Proof Cities consortium (Albers et al., 2015), which is part of the Knowledge For Climate program (http://knowledgeforclimate.climateresearchnetherlands.nl /climateproofcities).

Chapter 4

The effect of using a high-albedo material on the Universal Temperature Climate Index within a street canyon

Abstract[1]

This study investigates the effect of different high-albedo adaptation strategies on air temperature, mean radiant temperature and the Universal Temperature Climate Index (UTCI) for an idealized 2D street canyon. The used numerical model computes the heat transport in the canyon, and specifically takes into account the effect of multiple scattering of radiation. In general the mean radiant temperature has a much larger impact on the UTCI than the air temperature. Moreover, the mean radiant temperature exhibits strong spatial variations in the canyon due to its sensitivity to shading. The impact of albedo-differences on the UTCI is thus relatively small compared to the large shading effects. The best strategy to minimize the UTCI for the outdoor environment with building height to width ratio H/W=0.5 is found to be a uniform albedo of 0.2. For H/W=1.0, an albedo gradient from high at the bottom part to low at the top of the vertical walls showed the lowest UTCI. Although using high-albedo materials can mitigate the atmospheric urban heat island effect, it is very likely to increase pedestrian heat stress.

4.1 Introduction

Several studies (Whitman et al., 1997; Vandentorren et al., 2001; Baccini et al., 2008) have reported a relation between the ambient air temperature

[1]Published in Urban Climate (2016) **17** with H.J.J. Jonker, S.R. de Roode, S. Kenjereš

and the number of heat related deaths. This heat-mortality relation, in combination with the Urban Heat Island effect (UHI, which is the phenomenon wherein the presence of buildings causes the temperature in the city to be higher than in its rural surroundings), poses a challenging problem on city planners to reduce the ambient air temperature inside the city. To achieve this air temperature reduction, the use of high-albedo materials for roofs or paving is often advocated, amongst others by Akbari et al. (2001) and Synnefa et al. (2008).

As a result, the use of these high-albedo materials is also incorporated as guidelines for architects and city planners. For instance, the New York High Performance Infrastructure Guidelines (2005) and Philadelphia High Performance Building Renovation Guidelines (2004) both recommend to use high-albedo pavement as a substitution for black asphalt to counter the local urban heat build up. The general idea is that high-albedo materials absorb less solar radiation and thereby reduce the outdoor air temperature, which has been shown by many (Silva et al., 2009; Santamouris et al., 2012; Erell et al., 2014). For instance, Taha et al. (1999) studied the impact of large scale albedo changes for ten regions in the USA. A high-resolution regional weather forecast model was used, where the response of buildings and streets on the surface energy balance was specifically taken into account. The regions were characterized and simulated in reference- and modified-surface conditions. The results suggested that large-scale increases in the albedo and vegetative fraction can result in spatially-averaged decreases in mid-day air temperature of -0.5K to -1.5K during a typical summer day. The highest reduction found locally was -5K.

Changing the albedo also influences the indoor air temperature (or the cooling load of obstacles, which is more often studied (Taha et al., 1988; Simpson and McPherson, 1997; Bretz et al., 1998)). The effect of a different exterior albedo on the indoor air temperature has been demonstrated by Cheng et al. (2005), who performed idealized scale-experiments on a resolution of 1.5m. These experiments were performed with separate black and white test-boxes and little insulation (20mm thick waterproof plywood and 25mm thick Styrofoam as interior thermal insulation). Both in summer and fall, the maximum indoor air temperature inside the black test box was roughly 12K higher compared to the white test box.

Although a reduction in outdoor and indoor air temperature is considered positive, there are also down sides of using high-albedo materials. One of the adverse effects was demonstrated by Erell et al. (2014), in which the response of high-albedo materials on the outdoor pedestrian heat stress was investigated for four cities by using the Canyon Air Temperature model

(CAT, Erell and Williamson (2006)). The CAT model uses meteorological measurement data from nearby rural locations to compute the canyon air temperature, wind speed and radiative properties inside the urban canyon. Radiative properties are based on the sky view factor and H/W ratio of the canyon, while urban wind speed and air temperature are computed from empirical formulations. The CAT model was used to compute the effect of different albedo values on the local urban climate inside the street canyon. The output of this model was then used to compute the Index of Thermal Strain (ITS model, Pearlmutter et al. (2007)), which is a pedestrian heat stress parameter. The ITS model empirically relates the clothing insulation, humidity of air, wind speed and the thermal and solar radiative fluxes to the thermal comfort of a standing human in units of Watt. For example, Erell et al. (2014) found that although a high-albedo material can lead to lower air temperatures, it may also cause a higher value of the heat stress, which is due to the increase in reflected radiation that can reach the pedestrian. The thermal stress is decreasing with increasing H/W ratio, independent of the albedo that is used. To quote the authors: "The results of this study indicate that local benefits, in terms of pedestrian thermal comfort, are likely to be marginal at best and that high-albedo paving materials may actually increase thermal stress in warm environments." (Erell et al., 2014)

4.1.1 Goals

The current research aims to take the study by Erell et al. (2014) one step further. Instead of assuming a uniform albedo for the entire canyon as Erell et al. (2014), a variety of adaptation measures are tested. A building resolving model, called URBSIM (Schrijvers et al., 2015), is used which computes radiative transfer, heat conduction into the urban material, and ventilation within the urban canyon at a 1m spatial resolution. Temperature and wind in the canyon are computed at this resolution, compared to a single point in the study by Erell et al. (2014). The different adaptation measures include differentiation between the north-facing and south-facing walls and albedo gradients along the vertical walls. In this way the impact of using different albedo values on the air temperature, mean radiant temperature and the Universal Temperature Climate Index (UTCI, (Fiala et al., 2012)) can be studied.

4.2 Methodology and used data

4.2.1 The numerical model

The effect of different albedo adaptation measures is tested by using the building resolving simulation model URBSIM that was developed and used in Schrijvers et al. (2015). The strength of URBSIM is that it hardly parametrizes the processes, but attempts to remain as close as possible to the physics. Radiation is solved by a Monte-Carlo model, which does not rely on view factor algebra, heat transport into the urban material is solved by the 1D heat conduction equation and a transient Reynolds-Averaged Navier-Stokes (RANS) Computational Fluid Dynamics (CFD) model is used for convective transport of heat, while the CFD model also takes into account buoyancy (Schrijvers et al., 2015; Kenjeres and Hanjalic, 1999, 2006, 2009; Kenjeres and ter Kuile, 2013; Kenjeres et al., 2015). At present, URBSIM is the only model available in literature, that combines Monte-Carlo radiation modelling and CFD at the street canyon resolving resolution. Only a short description is given here, and the reader is referred to Schrijvers et al. (2015) for model details and validation cases.

The Monte-Carlo radiation model computes individual photon paths, which allows the assessment of the absorbed shortwave and longwave radiation at the surface, the longwave trapping effect and mean radiant temperature. The mean radiant temperature is defined as the temperature that a human body would have if all absorbed radiation is emitted again through longwave radiation (which assumes that the human body is in radiative equilibrium), and is computed by

$$T_{\mathrm{mrt}} = \sqrt[4]{\frac{S_{\mathrm{str}}}{\epsilon_{\mathrm{p}}\sigma}} \tag{4.1}$$

where S_{str} is the local mean radiant flux density, ϵ_{p} the emissivity of the human body (with a standard value of 0.97) and σ the Stefan-Boltzmann constant. The mean radiant flux density is the amount of both shortwave and longwave radiation that is absorbed by a standing human body and is computed following Thorsson et al. (2007) as

$$S_{\mathrm{str}} = (1-\alpha_{\mathrm{p}})\sum_{i=1}^{6} SW_i F_i + \epsilon_{\mathrm{p}}\sum_{i=1}^{6} LW_i F_i \tag{4.2}$$

where α_{p} is the albedo of the human body (with a standard value of 0.3), SW_i the total shortwave radiative irradiance, LW_i the total longwave radiative

irradiance and F_i a geometric factor representing a standing human body. The index i is used for the six directions where radiation is entering from. The geometric factor F has a value of 0.22 for radiation entering from each of the four cardinal points and 0.06 for radiation entering from the upward and downward directions (Thorsson et al., 2007). Since the current study is 2D, radiation entering from two cardinal points is missing (the faces occupying the 'air-sides' of the canyon), and is taken equal to that of the averaged radiation entering from the two known directions. This assumption can be regarded as computing the mean radiant temperature for a square, surrounded by obstacles.

The time dependent 1D heat conduction equation is used to compute the energy transfer from a building or ground surface into the underlying urban material (conductive heat flux). A zero-flux boundary condition is used for the temperature inside the urban material.

Wind speed, air temperature and the sensible heat flux are computed on a non-uniform grid, refined in the proximity of building walls and the ground, by a CFD model, which solves the unsteady RANS-equations for mass, momentum and temperature, as well as turbulent kinetic energy and dissipation through the standard $k-\epsilon$ model including the Durbin time scale (Durbin, 1996).

The three different model components, i.e. convective and radiative transport of heat in the canyon, and heat conduction through the ground and the walls, each compute a part of the surface energy balance, and are coupled through the surface temperature. A time step of 6 minutes is used, after which all fluxes are updated and a new surface temperature is computed. The main advantage of the presented model is that it computes in detail the interaction of the different processes at a building-resolving scale.

The input-parameters of the model are shown in Table 4.1. The location considered is that of Amsterdam (The Netherlands) in the middle of June, the month where the sun reaches the highest elevation angle in the Netherlands. Free stream air temperature is 293.15K and is constant with height and time. The same holds for the free stream wind speed of 4ms^{-1} (which is the average wind speed during the summer at Schiphol airport, nearby Amsterdam), such that only the solar radiation experiences a diurnal variation. These constant input parameters are used to reduce the complexity of the urban system. This idealized set-up does allow distinguishing between the different processes, and investigating the effect of the albedo change on the processes that govern the UTCI. For the same reason, both vegetation and vehicle traffic are omitted from this study. Although more advanced urban geometries have

	Radiation
Latitude	52° 22' N
Longitude	4° 53' E
Start day	2012-06-10 00:00
End day	2012-06-20 23:59
max SW_{dir}	833.1 $/rmWm^{-2}$
max SW_{dif}	84.2 Wm^{-2}
LW_{sky}	325.0 Wm^{-2}
	Heat conduction
λ	0.72 $\mathrm{Wm}^{-1}\mathrm{K}^{-1}$
ρ	1920 kgm^{-3}
C_{v}	835 $\mathrm{Jkg}^{-1}\mathrm{K}^{-1}$
Δwall	$0.25m$
Δground	1.00m
	CFD
T_{a}	293.15K
U	4.0 ms^{-1}
min cell width	1.0m
cell expansion	5 %
max cell size	25m

Table 4.1: Input constants for radiation, heat conduction into the urban material and the CFD model, where λ is the thermal conductivity of brick, ρ the density of brick, C_{v} the thermal heat capacity of brick, T_{a} the constant inlet air temperature and U the constant inlet wind speed

been studied (e.g. Tominaga et al. (2005) for 3D wind patterns, Brown and Delay (2001) for different building shapes and Theeuwes et al. (2014) for different heat transfer coefficients), these studies do not take into account the complex interplay between all processes at the building resolving scale.

The model uses an initial estimate of surface temperature, which is used to compute the air temperature and heat fluxes at the first time step after which all variables are able to freely evolve in time. Ten consecutive days are simulated. The simplified set-up with constant inlet conditions causes the results to become repetitive, in a statistical sense, after 5 days. We also note that the results do become independent of the prescribed initial conditions.

The model has been validated in Schrijvers et al. (2015). The Monte-Carlo radiation model was validated against effective albedo measurements

conducted by Aida and Gotoh (1982), and showed a fair agreement between measurements and simulation, both for winter and summer conditions. In addition to experimental data, analytic results by Madronich (1987) were used to validate the computation of the radiative fluxes. The CFD model has been extensively validated by comparisons of velocity and concentration measurements (Kenjeres and ter Kuile, 2013; Kenjeres et al., 2015) from the Mock Urban Setting Test (MUST) wind tunnel experiments (Biltoft, 2002; Hilderman and Chong, 2004) and against wind tunnel measurements of wind speed and air temperature from Uehara et al. (2000). Both validation cases showed good agreement between the CFD model and experimental data. In addition to these validation cases, a grid convergence study has been conducted which indicated that grid convergence is reached by using a 1m resolution (50×50 cells for H/W=1.0 and 25×50 cells for H/W=0.5).

In the current work, the model output is used to compute the UTCI. This is an apparent temperature, which takes into account air temperature, wind speed, radiation, humidity, metabolism of the human body and clothing insulation worn by the subject. The UTCI is defined as the isothermal air temperature of the reference condition that would elicit the same dynamic response (strain) of the physiological model (Jendritzky et al., 2012). It has been developed as a standard measure for outdoor thermal conditions, and is designed to be applicable in all climates, seasons, and time and spatial scales. The advantage of using the UTCI is that all effects of an adaptation measure on the outdoor environment are captured in one number, that is directly related to the amount of heat stress.

From the UTCI-website (Bröde, 2005), a Fortran90 sub-routine is available, which uses a sixth order polynomial function to compute the UTCI, which has been implemented in URBSIM. This function uses air temperature, mean radiant temperature, wind speed and relative humidity as input, and the energy balance between the human core and skin, between skin and clothing and the human metabolism is parametrized. The fit is valid for the following conditions:

- $223 \leq T_{\mathrm{a}} \leq 323\mathrm{K}$
- $-30 \leq (T_{\mathrm{mrt}} - T_{\mathrm{a}}) \leq +70\mathrm{K}$
- $0.5 \leq u_{10\mathrm{m}} \leq 17\mathrm{ms}^{-1}$

where T_{a} is the local air temperature and $u_{10\mathrm{m}}$ the wind speed at 10m height.

Since the local UTCI inside the canyon is investigated here, the wind speed at each grid cell centre inside the street canyon is used instead of the

UTCI [°C]	Stress category
> +46	Extreme heat stress
+38 to +46	Very strong heat stress
+32 to +38	Strong heat stress
+26 to +32	Moderate heat stress
+9 to +26	No thermal stress

Table 4.2: Assessment scale of the Universal Temperature Climate Index (Bröde et al., 2012).

wind speed at 10m height. In this way, changes in wind speed due to the different adaptation measures are taken into account.

Relative humidity is a very complex parameter to take into account into a micro-climate model, since it is dependent on evaporation, entrainment, boundary layer height and large scale advection. This would severely complicate the analysis, while it is not the main focus in the current investigation. Therefore, the relative humidity is taken as a constant, and an estimate is made of the maximum effect of relative humidity on the UTCI. By using different constant values of the RH (changing these in the postprocessing UTCI routine offline), an increase in the UTCI of 3.3°C is found when changing the relative humidity from 0% to 100%.

The UTCI uses an assessment scale, which is displayed in Table 4.2. This assessment scale relates the UTCI temperature to the amount of heat stress that a human will experience. It must be noted that all temperatures throughout this manuscript are in units of Kelvin, except the UTCI, which is defined as the temperature in degrees Celsius to remain consistent with the literature on the subject.

A graphical representation of URBSIM is shown in 4.1. This flowchart displays the input parameters for URBSIM and the output parameters that are in turn used as input for the UTCI subroutine.

4.2.2 Adaptation measures

Different adaptation measures are tested for an idealized 2D geometry with square obstacles which are equal in height and spaced equally. The building width (B) is 25m, distance between the obstacles (W) is 50m, while building height is varied between H=25m (H/W=0.5) and H=50m (H/W=1.0). Ten obstacles are used in the domain to ensure a fully developed flow in the last canyon. The 2D geometry limits this study to cases where

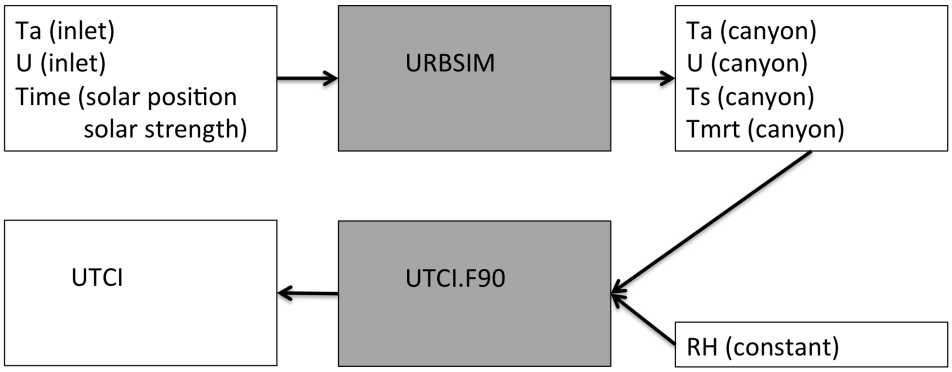

Fig. 4.1: Graphic representation of the different input and output of URBSIM to obtain the UTCI.

ventilation is mainly a 2D effect. For higher obstacles, it was found that the 2D geometry prohibits cross-flow through the canyon, which leads to a non-physical large stable stratification (Schrijvers et al., 2015). Therefore, these deep canyons are not considered here.

An east-west oriented canyon is used, such that building facades are either north-facing (shaded throughout the day) or south-facing (sunlit throughout the day). Since the current study is 2D, there is no solar azimuthal angle, and only the solar zenith angle is taken into account. Since the building facades are north-facing and south-facing, the 2D assumption is perfectly valid at solar noon.

As a first test, the albedo (α, which is referring to the reflectivity of solar radiation) of all canyon surfaces is varied between 0.2 (case 1), 0.4 (case 2) and 0.6 (case 3) respectively. These values for the albedo are also used for studying the impact of other adaptation strategies. An albedo of 0.2 corresponds to weathered asphalt, 0.4 to concrete and 0.6 to 'white-washed' surfaces. The outcome of varying longwave radiation is also quantified for different values of the emissivity ϵ, where ϵ is modified from 0.95 (case 2), 0.90 (case 4) and 0.85 (case 5) while the albedo is constant at α=0.4. Other test cases are shown in Fig. 4.2. Cases 6 and 7 investigate the effect of differentiating the albedo of the north-facing and south-facing wall, by using an albedo of 0.6 on one vertical surface and an albedo of 0.2 on the other surface. Cases 8 and 9 investigate walls with an albedo gradient, where a high top albedo (from a low-albedo bottom part to a high-albedo top part of the vertical wall) and a low top albedo (reversed) are used, respectively. Case 10 investigates a white roof (α=0.6 on all roof surfaces instead of the

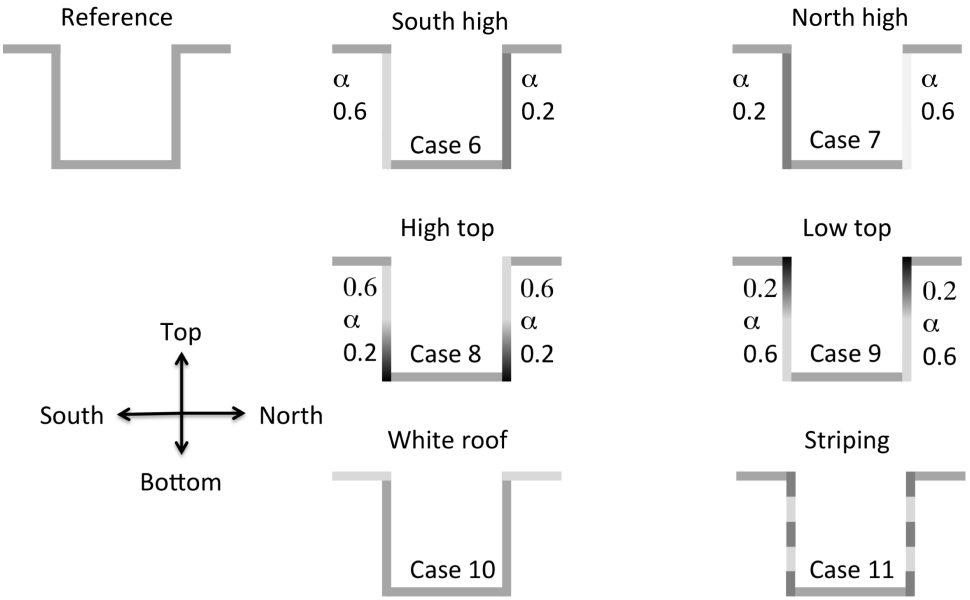

Fig. 4.2: Graphic representation of different albedo adaptation strategies. Cases with a uniform albedo (α=0.2, 0.4, 0.6) or uniform emissivity (ϵ=0.95, 0.90, 0.85) are not shown here. Note that the solar position is always on the south side of the canyon.

reference value of α=0.4). The hypothesis is that this reduces the ambient air temperature entering the canyon, which could cause a reduction of the UTCI. Case 11 investigates the impact of striping, where strips with different albedo values of 0.6 and 0.2 are used on the vertical walls. The reasoning is that this creates large spatial differences in surface temperature and therefore invigorates convection.

4.3 Uniform canyon properties

This section will discuss the two cases in which the canyon is uniformly modified. Firstly, the albedo case is discussed, secondly the case with different uniform emissivity values.

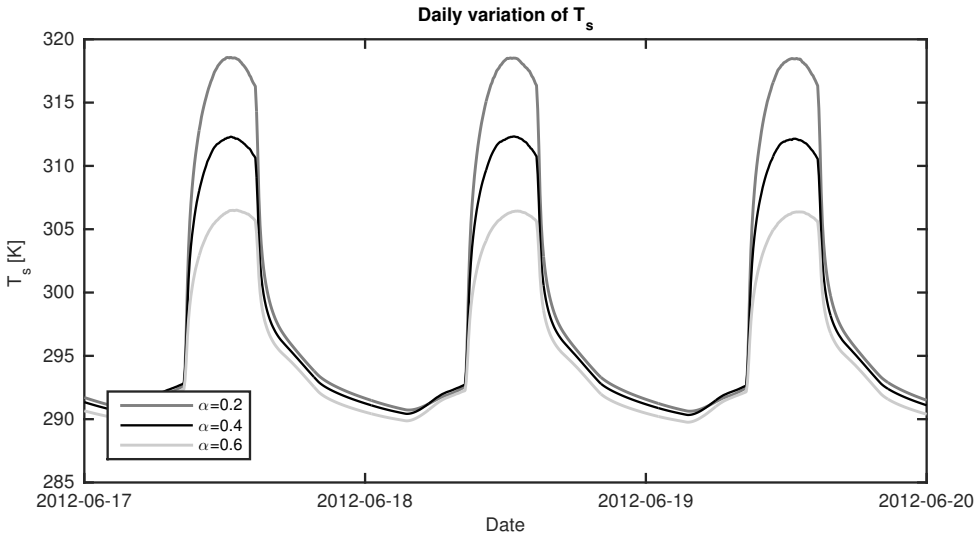

Fig. 4.3: Daily variation in surface temperature for one point in the centre of the street canyon (H/W=0.5) for three different albedo values. The cases considered are with a uniform albedo.

4.3.1 Uniform albedo changes

Diurnal cycle

The first question addressed is how different albedo values affect the daily cycle of surface temperature inside the canyon. Therefore, time series of surface temperature are displayed in Fig. 4.3. Results for a single representative point centred on the road surface of the street canyon are shown for H/W=0.5, and demonstrate a large variation in temperature, with the largest differences ranging from 290K during the night to 319K during day for the α=0.2 case. The case with α=0.6 displays differences between 290 and 306K. The large influence of the albedo can be observed during the day when the point of interest is directly sunlit, with surface temperature differences of 7K between the cases. However, the temperature differences during periods when the measurement point is in the shade (morning and afternoon) are small, indicating that the additional effect of multiple scattering is modest with changing the albedo. The impact of different albedo values is also limited during the night, where the surface temperature is mainly controlled by longwave radiation.

Since variations during the night are small, this study will only consider the results at solar noon of the last diurnal cycle.

Spatial distributions within a street canyon

Spatial changes as a result of different albedo values are shown in Fig. 4.4 for surface temperature (Fig. 4.4a), air temperature at 2m height (Fig. 4.4b) and mean radiant temperature at 2m (Fig. 4.4c). Solid lines are used for H/W=0.5, while dashed lines are used for H/W=1.0. Surface temperatures are plotted according to the inset in Fig. 4.4a, where all vertical surfaces are scaled to uniform height, to allow for direct comparison of different H/W ratios. Results for air temperature, mean radiant temperature and the UTCI are plotted along the width of the canyon (shown as canyon location), with 0m at the north-facing wall and 50m at the south-facing wall. Since both H/W ratios use a street width of 50m, this does not require scaling. Canyon-average values at z=2m height for air temperature, mean radiant temperature and the UTCI are also summarized in Table 4.3 for all cases.

The results are shown for solar-noon, and reveal higher values of surface temperature near the street level for H/W=1.0 in the sunlit region compared to H/W=0.5, due to an increased number of multiple reflections (Fig. 4.4a). A low albedo increases surface temperature by as much as +5K (H/W=0.5) and +14K (H/W=1.0) at the sunlit part of the ground surface compared to the reference case, while the influence of changing the albedo is negligible in the shaded areas. Temperature is changed in the high-albedo case by -5K (H/W=0.5) and -8K (H/W=1.0) in the sunlit areas. For both H/W ratios, the impact of changing the albedo on surface temperature becomes smaller towards roof levels.

Air temperature is lower for the high-albedo case compared to the reference case (Fig. 4.4b). For H/W=0.5, the difference in air temperature is (canyon averaged) +0.2K for α=0.2 and -0.4K for α=0.6 compared to the reference case (α=0.4). Note that the absolute air temperature is lower for H/W=1.0 compared to H/W=0.5 throughout the canyon. The difference in air tempera-ture as a result of changing the albedo is comparable in magnitude to the findings of Erell et al. (2014), despite the large differences in case set-up, inlet conditions and model that is used. This indicates that the impact of changing the albedo on air temperature is robust, i.e. similar for different conditions.

In addition to profiles at 2m height, contours of air temperature are shown in Fig. 4.5 for H/W=0.5 (left) and H/W=1.0 (right) and the three different cases considered. The results indicate that a low albedo creates a warmer canyon, for which there is more absorbed radiation, surface temperature is higher and consequently air temperature is increasing. For H/W=0.5, there is one recirculating vortex for all cases. For H/W=1.0, there are two counter

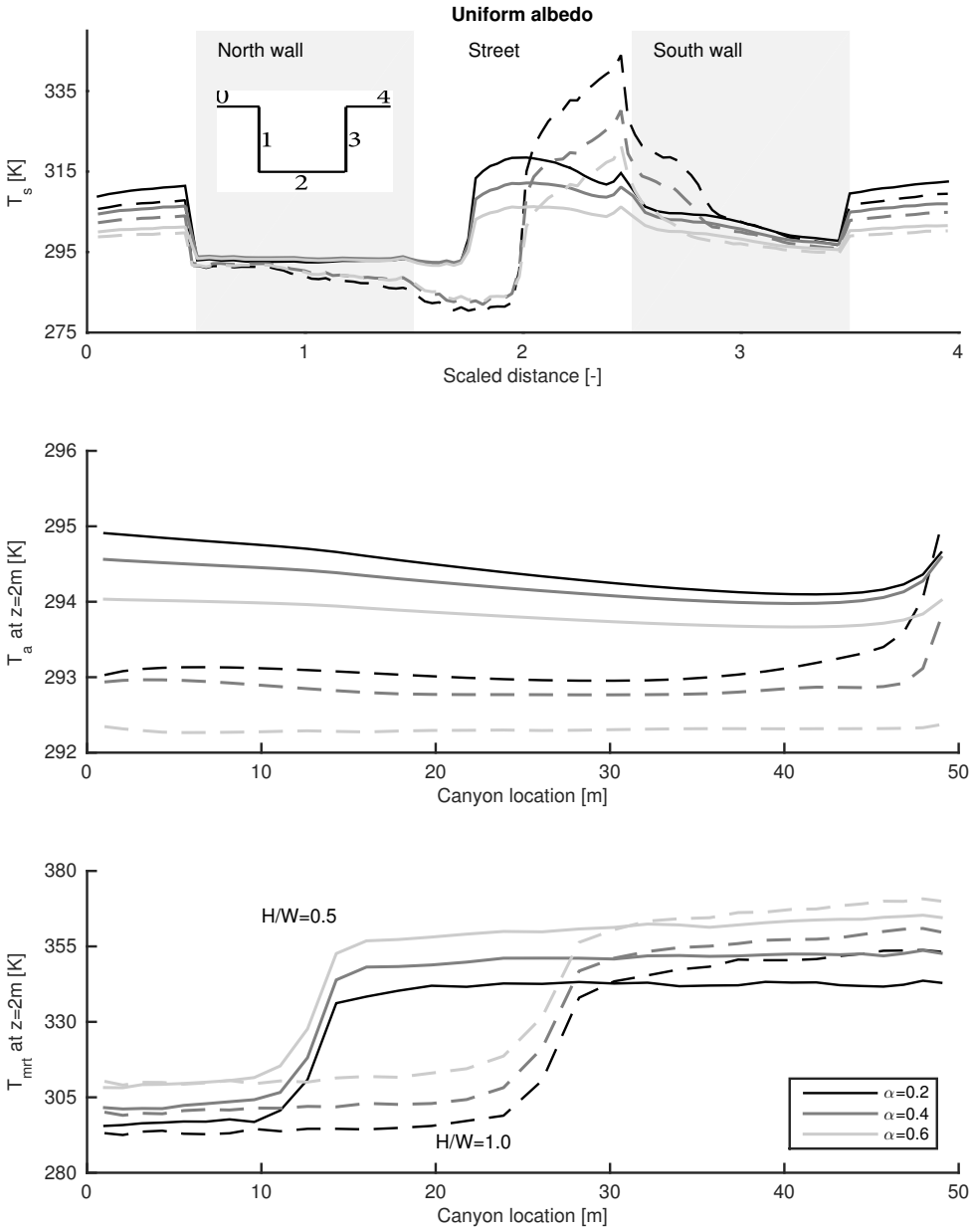

Fig. 4.4: Effect of albedo changes on surface temperature (a), air temperature at 2m height (b) and mean radiant temperature at 2m height (c). Grey scales are used for different cases, as indicated in the legend in the bottom panel. Solid lines are used for H/W=0.5, while dashed lines are used for H/W=1.0. Surface temperature is plotted according to the inset in the top panel. Air temperature and mean radiant temperature are shown as a function of the canyon location.

rotating vortices, where the warm south-facing wall creates buoyancy forces that are large enough to create a second vortex that spans the bottom part of the canyon. The air temperature profile at $2m$ height reveals relatively modest changes compared to the remainder of the canyon. It must be realized that the conditions considered are idealized by using a fully developed flow in the canyon under consideration and that the model is 2D. Despite these simplifications, these results reveal an intricate interplay between a wind induced vortex and canyon buoyancy.

According to Eqs 4.1 and 4.2, the mean radiant temperature (Fig. 4.4c) is not only influenced by the change in reflected shortwave radiation, but also by the emitted longwave radiation due to changing surface temperature. Mean radiant temperature displays the contrary effect to air temperature, where the high-albedo case shows a higher mean radiant temperature (+9.5K for H/W=0.5). The difference is however small when compared to the effect of shading, where T_{mrt} is over -40K lower in the shaded areas compared to the sunlit areas. For H/W=1.0, there is a larger area in the shade, with substantially lower canyon-averaged T_{mrt} as a consequence. In the sunlit part of the canyon, T_{mrt} is higher for H/W=1.0 compared to H/W=0.5 due to increased multiple reflections of shortwave radiation. Surprisingly, increasing building height has thus two different effects: there is a larger shaded area with lower heat stress, but due to the increase in multiple reflections the sunlit area experiences stronger heat stress.

T_{mrt} is controlled by the large contributions of direct shortwave radiation (which has a maximum value of 900 Wm^{-2} in the sunlit area. The maximum value obtained is higher than the incoming 833Wm^{-2} from Table 4.1 due to multiple reflections) and the longwave trapping effect (with a maximum contribution of 700 Wm^{-2}). This results in a T_{mrt} of 350K (sunlit part, H/W=0.5, α=0.4). When these values are compared to measurements of mean radiant temperature and radiative fluxes in the city of Göteborg, Sweden (Lindberg et al., 2008), the values obtained in the current study are higher than obtained from measurements, where a maximum T_{mrt} was found of 340K for a large open square with α=0.4. The higher mean radiant temperature from the model is partly due to the 2D assumption, in which radiative fluxes from the east and west direction are taken equal to the average of the north and south direction. For the α=0.4 case, the horizontal fluxes originating from the direct shortwave radiation in the sunlit area are 680Wm^{-2} and 320Wm^{-2} for the southward and northward directions, respectively. As a result, the current assumption uses its mean value 500Wm^{-2} for the east and westward flux, which results in a mean radiant temperature of 333.0K. However, if the minimum value for the direct shortwave radiation

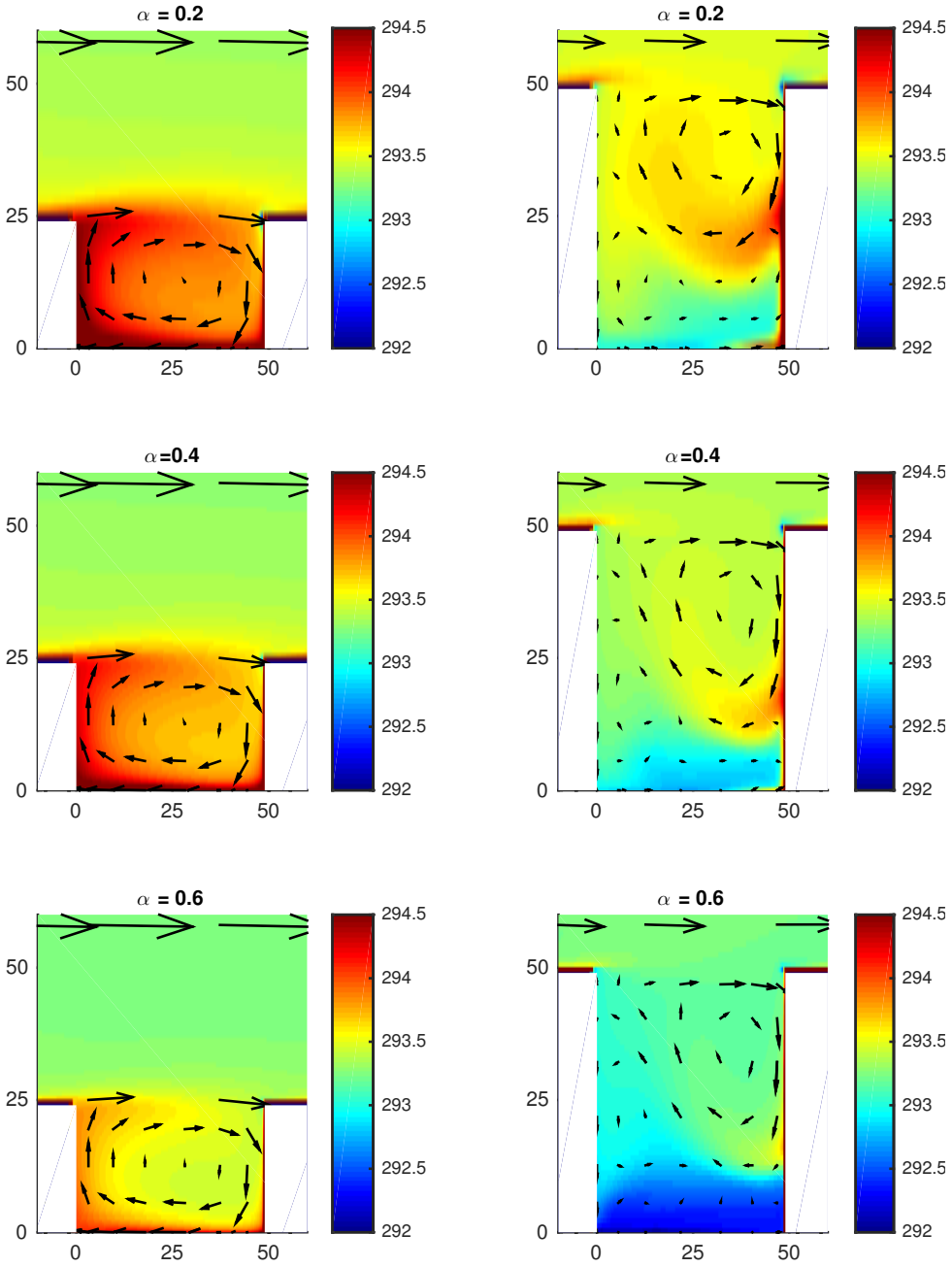

Fig. 4.5: Overview of air temperature for H/W=0.5 (left panels) and H/W=1.0 (right panels) when the albedo is changed uniformly over the entire canyon. The same colour axis is used for all sub plots. Local wind is indicated by arrows, where the top arrows at H/W=0.5 show a wind speed of 4ms^{-1}.

Case name	Case description	ΔT_a [K]	ΔT_{mrt} [K]	ΔUTCI [°C]
Case 1	α=0.2, ϵ=0.95	+0.2 / +0.3	-8.1 / -7.3	-1.9 / -1.9
Case 2	α=0.4, ϵ=0.95	0.0 / 0.0	0.0 / 0.0	0.0 / 0.0
Case 3	α=0.6, ϵ=0.95	-0.4 / -0.6	+9.5 / +9.7	+2.0 / +2.1
Case 4	α=0.4, ϵ=0.90	0.0 / +0.2	0.0 / 0.0	0.0 / +0.3
Case 5	α=0.4, ϵ=0.85	0.0 / +0.5	0.0 / -0.1	0.0 / +0.4
Case 6	South low	+0.3 / -0.7	-2.2 / -2.7	-0.2 / -1.1
Case 7	North low	-0.6 / +0.2	+1.7 / +0.2	-0.2 / +0.3
Case 8	High top	-0.4 / -0.1	-0.7 / -1.2	-0.4 / -0.4
Case 9	Low top	+0.8 / 0.0	-7.4 / -8.6	-1.1 / -2.7
Case 10	White roof	+0.1 / -0.1	+0.4 / +0.2	+0.2 / +0.1
Case 11	Striping	+0.8 / -0.6	-1.7 / -0.7	+0.3 / -0.3

Table 4.3: Effect of albedo and emissivity changes on air temperature, mean radiant temperature and the UTCI compared to reference case 2 with α=0.4 and ϵ=0.95. Results are canyon averaged values at z=2m for H/W=0.5 and H/W=1.0 respectively. Case description is shown in Fig. 4.2.

(in this case 320Wm^{-2}) would be used, the mean radiant temperature would reduce to 329.9K. In addition to the 2D assumption, the current study considers highly idealized conditions, where there is no vegetation, no latent heat flux and clear skies, thereby allowing for these large radiative fluxes.

The air temperature and the mean radiant temperature are both used as part of the input in the computation of the UTCI, which shows an increase for high-albedo canyons (see Fig. 4.6), by as much as +2°C for both H/W ratios compared to the reference case. Using a low albedo changes the canyon-averaged UTCI by -1.9°C for both H/W ratios. However, the influence of changing the albedo is small compared to the shading effect, which changes the UTCI in the shaded areas by as much as -12°C, thereby indicating only 'moderate heat stress' if there is any stress at all. The large reduction of the UTCI in shaded areas is mainly due to the large decrease of direct shortwave radiation, which impacts the mean radiant temperature and therefore the UTCI. The local differences in air temperature can not compensate the change in the mean radiant temperature. For an increase in T_{mrt} of +15K, air temperature should reduce by -7K to maintain the same UTCI temperature for this case. Note that for this comparison, feedback effects from air temperature to the sensible heat flux, conductive heat flux, surface temperature and mean radiant temperature are neglected, which gives just a very coarse indication of the required temperature increase.

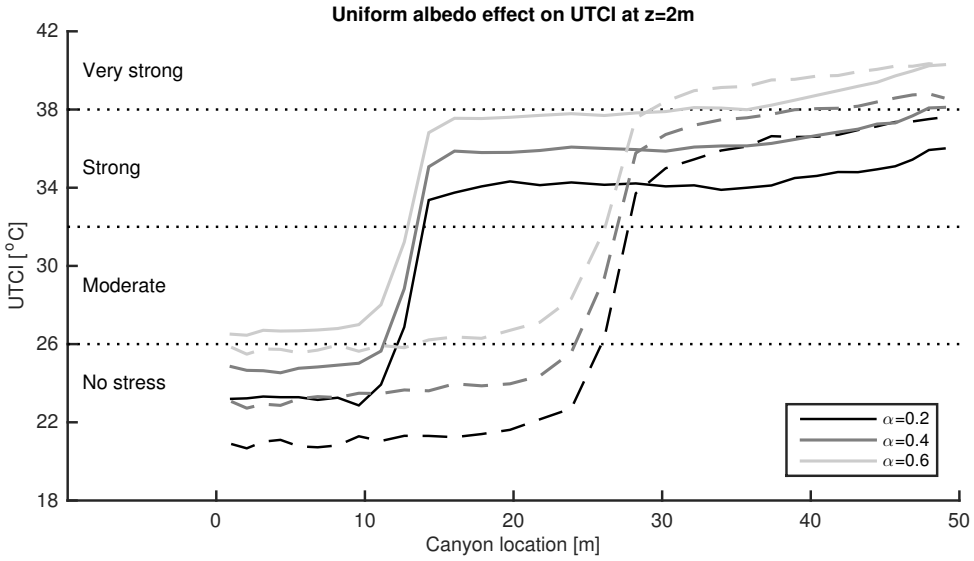

Fig. 4.6: The UTCI temperature for different values of the albedo, where the albedo is changed over the entire canyon. Solid lines indicate H/W=0.5, dashed lines are used for H/W=1.0.

Erell et al. (2014) found that for any albedo value the thermal stress for a pedestrian in the middle of the street canyon is decreasing with increasing H/W ratio. A similar result is obtained in the current study for the shaded part of the canyon. By contrast, in the sunlit part, the thermal stress increases due to the effect of multiple reflections at this location.

4.3.2 Uniform emissivity effect

In addition to changing the canyon albedo, a varying emissivity is investigated. There are currently coatings available that can be applied on the glass surface, such that emissivity is reduced. Unfortunately, the combined effect of glass including this emissivity-reducing coating is usually not given. Therefore, this remains an academic case, to investigate the possible impact of low-emissivity materials. Noting that according to Kirchhof's law the spectral emissivity equals the absorptivity of infrared radiation, one could hypothesise that decreasing the emissivity could lead to a feedback effect on surface temperature (less absorbed radiation from the sky, lower surface temperature, less longwave trapping, lower surface temperature, etc.), which could significantly lower the UTCI. The second consequence of reducing the surface emissivity is an increase in the surface temperature, due to the

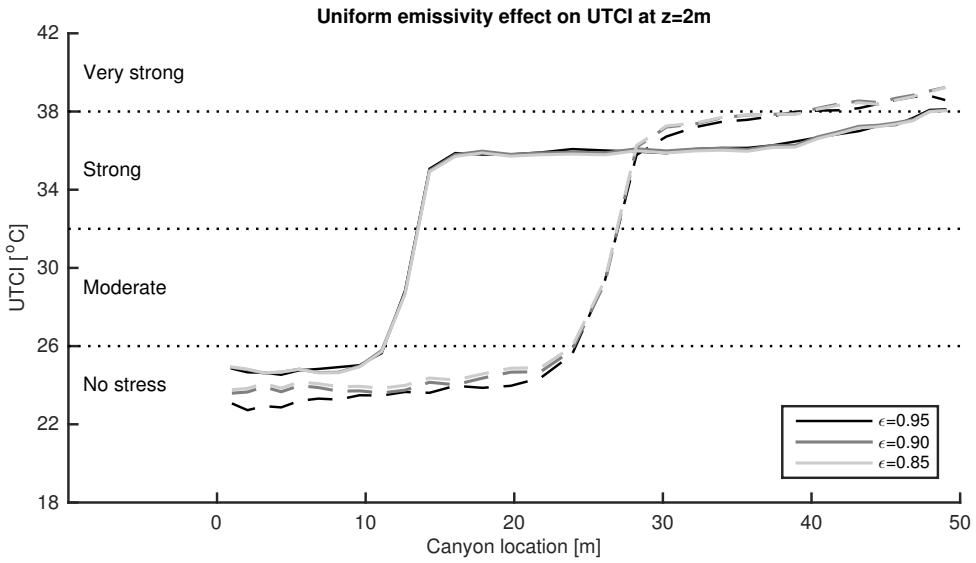

Fig. 4.7: Effect of different values of the emissivity on the UTCI, compared to the reference case with a uniform ϵ of 0.95. Solid lines are used for H/W=0.5, dashed lines for H/W=1.0.

reduced emission of longwave radiation from the surface. In the current study, the total impact of changing the emissivity is investigated, and the two separate mechanisms discussed above are not investigated separately.

The effect of varying the emissivity on the UTCI is visualized in Fig. 4.7 and in Table 4.3 for the different cases. A decrease in the emissivity from 0.95 to 0.85 did not affect the UTCI for H/W=0.5 and increased the UTCI by +0.4°C for H/W=1.0.

Absorbed infrared radiation at the surface is decreasing with a lower emissivity. However, this decrease is much smaller compared to changing the albedo of solar radiation. Due to the high value of the emissivity, the amount of energy involved with multiple reflections is smaller. Since the change in surface temperature is small, there is also little ramification on the longwave trapping effect. The UTCI is therefore hardly changing. For H/W=1.0, air temperature is increasing more than the mean radiant temperature is decreasing, leading to an increase in the UTCI.

4.4 Sensitivity studies

4.4.1 Differentiating albedo of the street canyon vertical walls

In this section, case 6 (a high-albedo on the north-facing wall) and case 7 (with a high-albedo for the south-facing wall) are compared to the reference case 2 with a uniform albedo (see Fig. 4.2 for a graphic representation). Note that the average albedo over all surfaces remains equal for these cases.

Varying the albedo of the vertical walls reduces the surface temperature for case 7 (Fig. 4.8a) at the lower corner between the south-facing wall and ground by -8K (-12K) for H/W=0.5 (H/W=1.0). The north-facing wall is heated by +2K compared to the reference case for both H/W ratios. The heating of the north-facing wall can be explained from the fact that the surface does not only absorb more solar radiation due to the lower albedo, but also due to the increased amount of received radiation that is reflected by the south-facing wall. The impact of a high albedo for the north-facing wall (case 6) is however smaller, with only a reduction in surface temperature of -1.5K (-3.0K) for H/W=0.5 (H/W=1.0) at the north-facing wall, while the surface temperature of the low-albedo south wall is increasing by +7K (+15K) for H/W=0.5 (H/W=1.0).

Air temperature profiles (Fig. 4.8b) reveal differences of up to +0.7K for case 7. The results are also summarized in Table 4.3. However, the most interesting phenomena can only be seen from the spatial air temperature patterns, as shown in Fig 4.10. For H/W=0.5, the canyon for case 7 is found to be colder than the reference case, particularly due to the lower surface temperature at the south-facing wall. For H/W=1.0, case 7 results in a higher air temperature at the bottom of the canyon, which is due to a change in vortex dynamics between the different cases. The reference case and case 6 exhibit two counter rotating vortices, where cold air is trapped at the lower part of the canyon. For case 7, the surface temperature at the south-facing wall is lower, there is less warm air rising and the forced convection (due to the free stream air flow) is larger than natural convection (due to buoyancy forces). This results in one single vortex which spans the whole canyon. The considered adaptation measures demonstrate different effects on air temperature for different H/W ratios. This justifies including CFD modelling, as it illustrates how a change in the albedo can completely alter the air flow patterns. It is recommended to investigate these phenomena with more advanced models (for instance the algebraic flux model) further, since it is known that k-ϵ turbulence models can have difficulties with complex buoyant flows.

The mean radiant temperature is shown in Fig. 4.8c, and display a

decrease for case 6 of -2.5K while it is increased by +1.7K (H/W=0.5) and +0.2K (H/W=1.0) for case 7.

Despite the changes in surface temperature, air temperature and mean radiant temperature, the effect of differentiating the albedo of the north-facing and south-facing wall on the UTCI is small for H/W=0.5 (see Fig. 4.9). Both cases with a different albedo at either side of the buildings reduce the UTCI by -0.2°C. For H/W=1.0, larger differences are present, where case 6 reduces the UTCI by -1.1°C, while case 7 with the high-albedo south-facing wall increases the UTCI by +0.3°C. Both H/W ratios indicate that a low-albedo south-facing wall reduces the UTCI, despite the increase in air temperature, again demonstrating the large impact of shortwave radiation.

4.4.2 Vertical albedo gradients

Instead of changing the albedo of the entire wall, two cases are considered where there is an albedo gradient on the vertical walls (case 8, which uses a high-albedo at the top, and case 9 which uses a low albedo at the top, see Fig. 4.2).

Differences in surface temperature due to the varied albedo values are mainly present at the bottom part of the south-facing wall (Fig. 4.11a), with maximum changes of +7K for case 8 and -7K for case 9.

Larger differences in air temperature are found (Fig. 4.11b) for the albedo gradient case compared to the uniform albedo cases, with a decrease in air temperature of -0.4K (H/W=0.5) for case 8 and an increase of +0.8K for case 9 (H/W=0.5). With a high albedo at the upper part of the canyon, there is less heating of ambient air at the top of the canyon, which has a lasting impact on the remainder of the canyon. The recirculating air is heated inside the canyon, but the canyon as a whole remains colder compared to the reference case.

For each of the vertical albedo cases, the mean radiant temperature is surprisingly decreasing as compared to the reference case (Fig. 4.11c). For case 9, the mean radiant temperature decreases by roughly -8K, while this is -1K for case 8. For a low albedo at the top part of the canyon, more shortwave radiation is absorbed at the top of the canyon, and less radiation is reflected towards the ground surface, and is present for both direct shortwave radiation and diffuse shortwave radiation. For case 8, the high-albedo top of the canyon reflects more radiation into the canyon, which is absorbed at the lower parts of the vertical walls.

If all effects are combined into the UTCI (Fig. 4.12), a decrease is shown

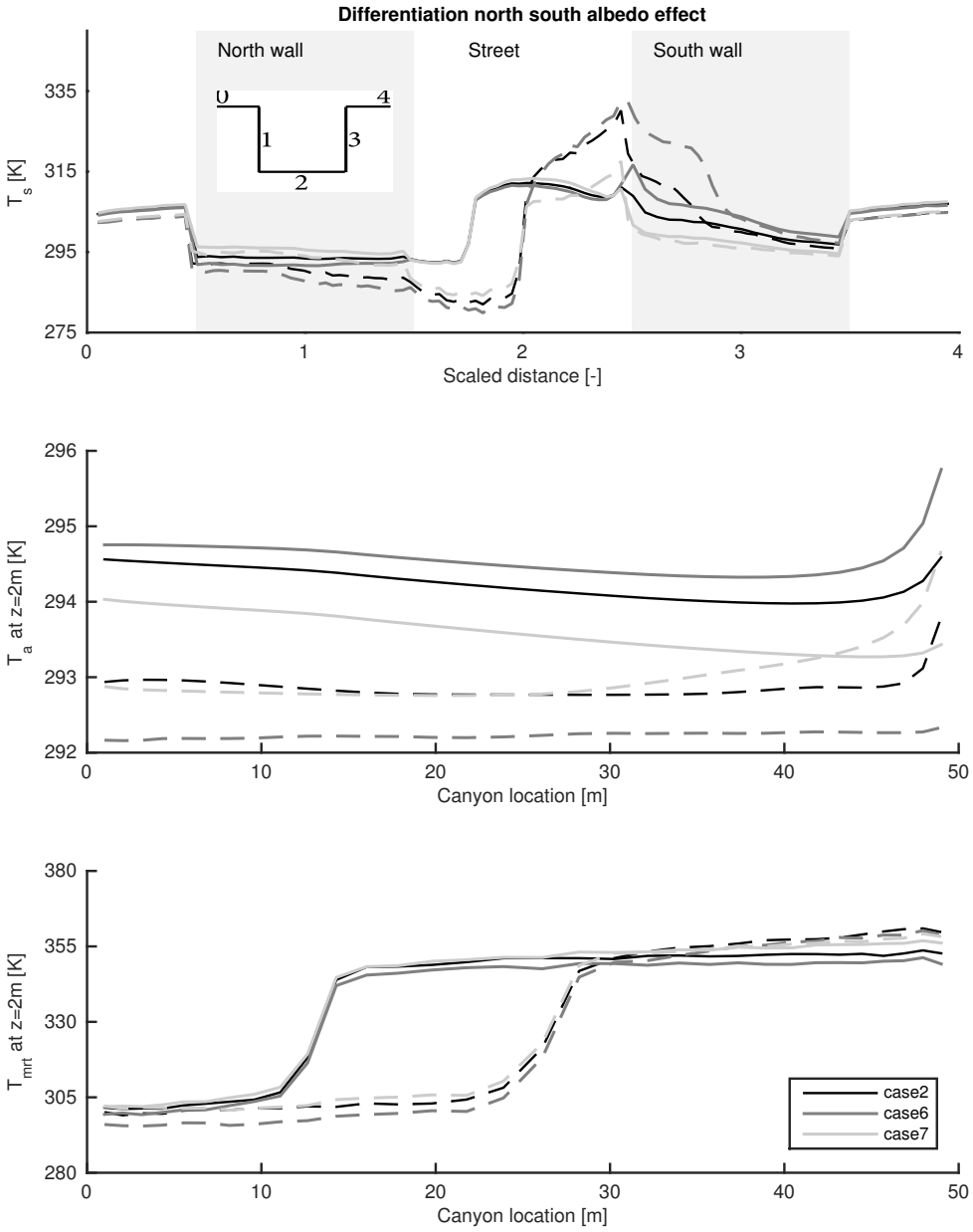

Fig. 4.8: Effect of using a high-albedo north-facing (case 6) and south-facing (case 7) wall on surface temperature (a), air temperature at 2m height (b) and mean radiant temperature at 2m height (c). A graphic representation of the cases is displayed in Fig. 4.2. Solid lines are used for H/W=0.5, while dashed lines are used for H/W=1.0. Surface temperature is plotted according to the inset in the top left panel. Air temperature and mean radiant temperature are shown as a function of the canyon location.

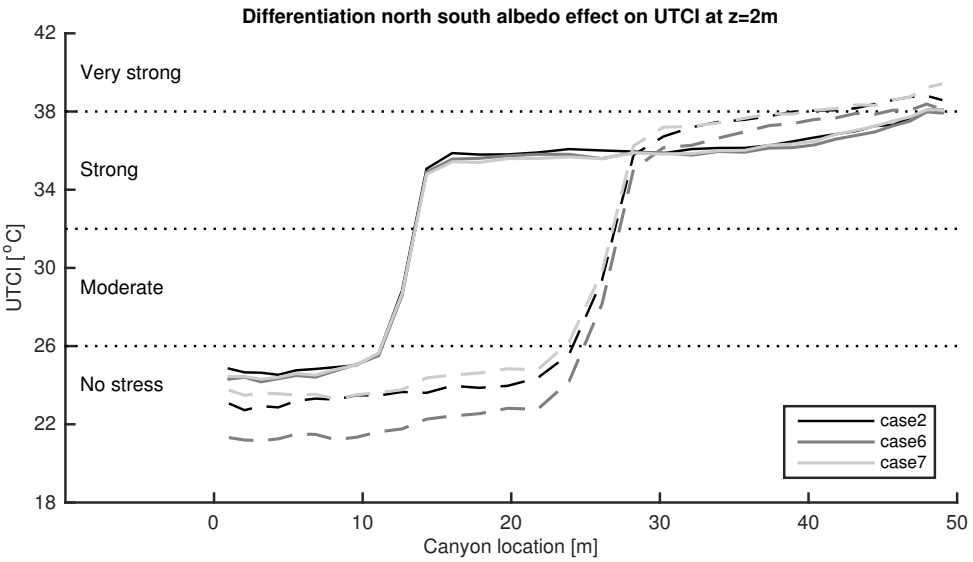

Fig. 4.9: Effect of differentiating the albedo of north-facing and south-facing wall on the UTCI, compared to the reference case with a uniform albedo of 0.4. Solid lines are used for H/W=0.5, dashed lines for H/W=1.0.

for both cases. Case 8 exhibits a decrease of -0.4°C for both H/W ratios, while case 9 decreases the UTCI by -1.1°C for H/W=0.5 and -2.7°C for H/W=1.0. The decrease in the UTCI for H/W=1.0 is larger for case 9 than a uniform albedo of 0.2 and is thereby the most efficient measure to reduce the outdoor thermal comfort found in the current study.

4.4.3 White roof and striping

Results for the UTCI for cases 10 (white roof) and 11 (striping) are displayed in Fig. 4.13 and Table 4.3 and display small changes in the UTCI compared to the reference case. For case 10, there is a reduction in ambient air temperature as hypothesised in Section 4.2.2 for H/W=1.0, but this is small (-0.1K). The reduction in ambient air temperature is not present for H/W=0.5. Remarkably, mean radiant temperature is increasing, which leads to an increase in the UTCI of +0.2°C for $H/W = 0.5$.

Case 11 (striping of vertical surfaces) has a large impact on surface temperature, where local differences of up to 10K are found compared to the reference case. However, such large temperature differences are not present when air temperature is considered, with an increase for H/W=0.5 (+0.8K) but a decrease for H/W=1.0 (-0.6K). Mean radiant temperature reveals

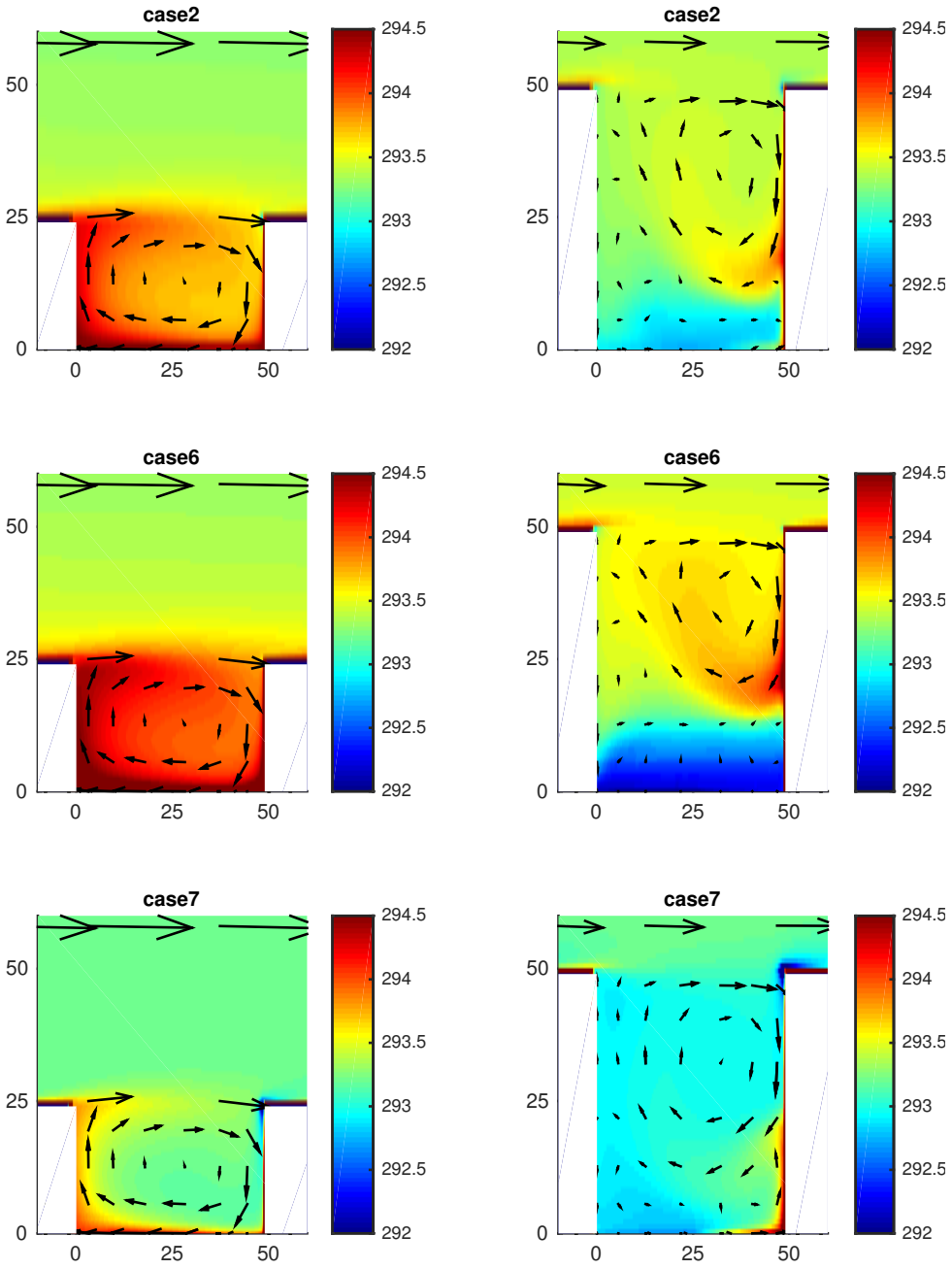

Fig. 4.10: Overview of air temperature for H/W=0.5 (left panels) and H/W=1.0 (right panels) for the reference case (uniform albedo of 0.4, top panels), case 6 (high-albedo north-facing wall, middle panels) and case 7 (high-albedo south-facing wall, bottom panels). The colour scale used is identical to the color-scale used in Fig. 4.5

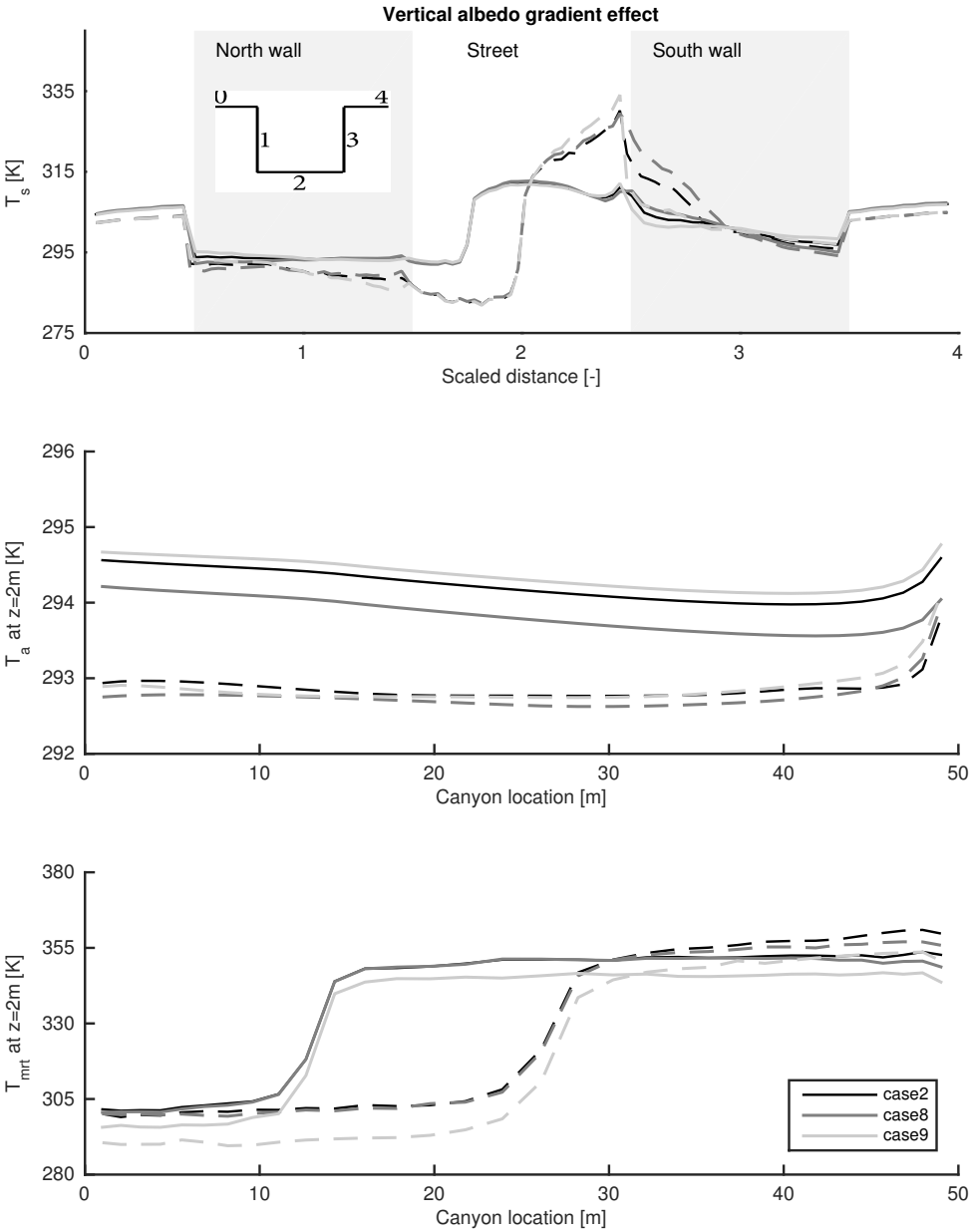

Fig. 4.11: Effect of vertical albedo gradients on surface temperature (a), air temperature at 2m height (b) and mean radiant temperature at 2m height (c). Case 8 uses a high albedo at the top part of the vertical wall, case 9 a low albedo.

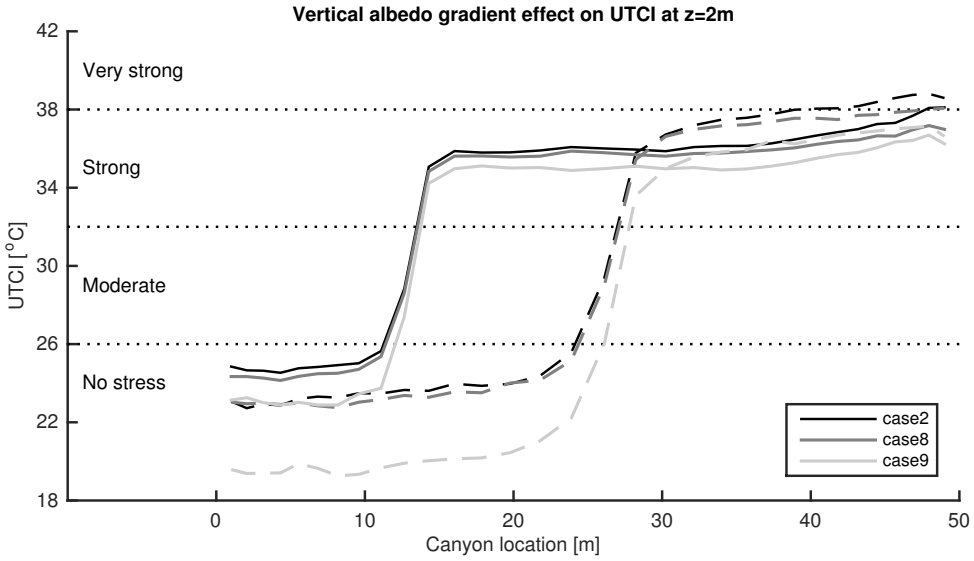

Fig. 4.12: Effect of vertical albedo gradients on the UTCI, compared to the reference case with a uniform albedo of 0.4. Case 8 uses a high albedo at the top part of the vertical wall, case 9 a low albedo. Solid lines are used for H/W=0.5, dashed lines for H/W=1.0.

opposite effects to air temperature, which results in a small impact on the UTCI for H/W=0.5 (+0.3°C) and a decrease in the UTCI for H/W=1.0 of (-0.3°C). It is unclear why striping demonstrates differences in the UTCI for the different H/W ratios.

4.5 Discussion

The present study is an extension of the work by Erell et al. (2014), who performed simulations with a uniform albedo for different H/W ratios in different cities. A more advanced model is used compared to Erell et al. (2014), which couples a CFD model, a Monte-Carlo radiation model and thermal diffusion through the 1D heat conduction equation, but finds similar results for the case with a uniform albedo. However, Erell et al. (2014) only considered a standing person in the middle of the canyon, while the entire canyon is investigated in the current study. As a second extension, different albedo adaptation strategies are used, which showed that using an albedo gradient (from a high-albedo at the top part of the vertical wall to a low-albedo at the bottom part) can be more beneficial in terms of lowering the heat stress compared to a uniform low albedo for H/W=1.0.

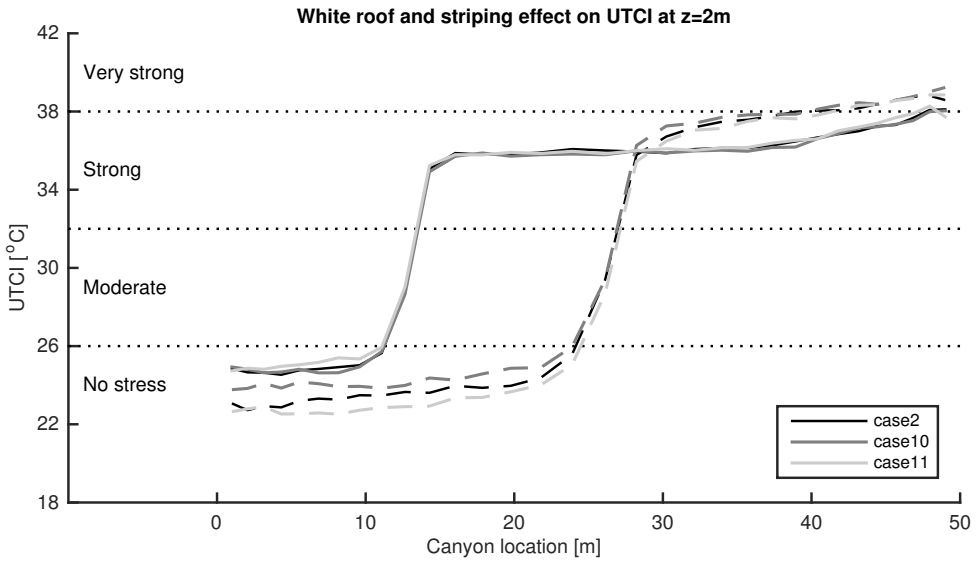

Fig. 4.13: Effect of white roof (case 10) and striping (case 11) on the UTCI, compared to a uniform albedo of 0.4 (case 2). Solid lines are used for H/W=0.5, dashed lines for H/W=1.0.

The maximum effect that is obtained by using different albedo adaptation strategies is about -2°C on the UTCI, and is independent of H/W ratio. Surprisingly, increasing the building height reveals two distinct effects: there is a larger shaded area with a lower heat stress, but due to the increase in multiple reflections the sunlit area experiences stronger heat stress, especially near the sunlit south-facing wall. The UTCI is reduced by up to -12°C in shaded areas compared to the sunlit areas, almost independent of the case that is investigated. The shadow-effect is also seen for the different H/W ratios: for every case investigated, the canyon averaged UTCI at $2m$ is lower for H/W=1.0 compared to H/W=0.5, which is also what Erell et al. (2014) found. Therefore, it might be worthwhile to investigate artificial shading measures, which provide shading during the day but can be opened during night (increase ventilation and reduce longwave trapping).

The present study also demonstrated that changing the albedo values can alter the vortex dynamics inside a street canyon. Although idealized conditions are used here, buoyancy forces respond to the various measures, which encourages further investigations with more advanced CFD models. The effect of changing surface temperature on vortex dynamics has been found in academic cases before, with heating of individual building surfaces (Kim and Baik, 2001; Huizhi et al., 2003). Although the changing surface

temperature leads to relatively small air temperature differences, the possible change in air flow inside the street canyon can have large consequences on, for instance, pollutant dispersion, as was shown by Baik et al. (2007). Exhaust gases of cars can be trapped in the bottom part of the canyon, or more easily dispersed throughout the canyon, dependent on the flow dynamics.

It must be noted that only the outdoor situation is considered in this study, and that the indoor environment can reveal opposite effects to the outdoor environment. Although Cheng et al. (2005) found a reduction in indoor air temperature when using a high-albedo, Yaghoobian and Kleissl (2012) found the opposite. The reflected radiation is penetrating through the windows, and therefore can increase the indoor temperature. The effect is however very much dependent on the street geometry, albedo and amount of glazing. This indicates that using one adaptation strategy on all locations might give different results, dependent on the local geometry.

The cases considered in this study are highly idealized and only consider a 2D geometry with constant free stream air temperature and wind speed during the summer time. Therefore, the model used can be considered of intermediate complexity. The goal is to include the full 3D arbitrary environment, for which currently steps are undertaken (Tomas et al., 2015; Kenjeres et al., 2015). In addition to the 3D environment, these studies use more advanced turbulence modelling (Large Eddy Simulations in Tomas et al. (2015) and a hybrid RANS-LES model in Kenjeres et al. (2015). Other seasons can also be investigated. For this reason, URBSIM can be coupled (for instance) to a large scale weather model. However, this is currently outside the scope of the current study. In addition to the highly idealized conditions considered in this study, only the building height is changed to obtain different H/W ratios. Using a constant H/W ratio indicates that air flow fields are similar independent of building height or street width. However, this similarity does not hold for the situation at pedestrian level ($z = 2\text{m}$), which is impacted by the actual building height. Qualitative results will not change dramatically, due to the already large building heights used here.

4.6 Conclusions

This study systematically investigated the effect of different albedo adaptation strategies on surface temperature, air temperature, mean radiant temperature and the UTCI for an idealized 2D street canyon. Using high-albedo materials for all canyon surfaces decreases air temperature but increases the mean radiant temperature more strongly, leading to an increase in the UTCI (indi-

cating more heat stress). This contrasting behaviour of air temperature and mean radiant temperature is observed for all cases. When the UTCI is considered, a higher albedo increases heat stress, which is consistent with the findings from Erell et al. (2014).

The lowest heat stress (within the simplified test cases considered) was found to occur for the case with a vertical gradient of the albedo for H/W=1.0. The gradient used a high albedo at the bottom part of the vertical wall and low albedo near roof level. Air temperature increases slightly compared to a uniform albedo of α=0.4, but reduces the UTCI the most (-2.7°C). For H/W=0.5, a uniform low albedo of α=0.2 resulted in the largest decrease in heat stress (-1.9°C) for which the increase in air temperature is compensated by a large decrease in mean radiant temperature.

The present study indicates that there are adverse effects of using high-albedo materials, where air temperature and mean radiant temperature often show opposite responses. It is therefore concluded that simply using high-albedo materials wherever possible might not lead to the desired result of a reduction in the thermal heat stress.

4.7 Acknowledgement

We would like to thank Victor Vertregt and Franka Veltman for their help in developing the Monte-Carlo radiation model and the implementation of the mean radiant temperature. This study is funded by the Dutch Climate Proof Cities consortium, which is part of the Knowledge for Climate program (http://knowledgeforclimate.climateresearchnetherlands
.nl/climateproofcities).

Chapter 5

Comparing a large-scale urban parametrisation scheme and micro-scale model

5.1 Introduction

Big cities (with a typical length scale in the order of 10km) comprise of a wide range of spatial scales that are relevant for the energy balance, which can span more than 5 orders of magnitude. To compute the bulk effects in terms of fluxes of heat, moisture, momentum and radiation of the urban environment on the atmosphere, parametrization schemes are typically used. These schemes model small scale processes (smaller than the grid size that is used) and therefore allow for larger grid cells and thus larger domain sizes. The smallest urban length scale is that of individual buildings (the urban micro-scale), where there is interaction between the building surfaces and their direct surroundings (Sini et al., 1996; Kim and Baik, 2001; Bohnenstengel et al., 2004; Xie et al., 2005; Schrijvers et al., 2015, 2016, 2020a). The micro-scale can be extended to that of neighbourhoods, which consists of multiple street canyons. Large cities also affect the surrounding rural climate, for instance by the urban plume (Masson, 2006) or rain formation in the wake of cities (Baik et al., 2001). To capture all these different scales, parametrization schemes are typically used.

Different parametrization schemes exist that represent the urban environment, which can be roughly categorized in three groups. The simplest of these models is the bulk-model, where parameters for a flat terrain are adapted to better represent the urban environment (Liu et al., 2006). The changes can include 1) increasing the roughness length compared to a flat terrain to account for changes in the generated turbulence by obstacles, 2) decreasing the effective surface albedo to account for increased absorption of

shortwave radiation due to multiple reflections, 3) adapting the volumetric heat capacity and thermal conductivity of the ground, such that the conductive heat flux into the urban material is better represented and 4) reducing the green fraction over urban areas to account for the reduced evaporation. These models are often designed to incorporate the effects of the urban environment on the large scale, but are in general unable to give detailed results for the urban micro-scale.

More complex models use the urban geometry to parametrise individual processes, as is done in the Single-Layer Urban Canopy Model or SLUCM (Kusaka et al., 2001). In this model, the urban geometry is represented by a two-dimensional, symmetrical street canyon with infinite length (see Fig 5.1). From the elementary 2D geometry, radiative transfer, the conductive heat flux (only depicted from the ground to the canyon space in Fig. 5.1) and the transport of convective heat are computed for a 3D environment. Distinction is made between the roof, wall (both vertical walls have the same properties) and ground surface. The model uses a so-called resistance network, which computes transfer from the obstacle surface to the canyon space (defined at height $z_T + d$), and from the canyon space to the atmosphere above the urban canyon. The implicit assumption made in the SLUCM scheme, is that the entire urban geometry within a single grid box behaves as such a street canyon, where variations in building heights, street widths and canyon orientation are neglected.

Instead of using one layer to represent the urban environment, there are also models that use multiple levels (Multi-Layer Urban Canopy Models or Building Effect Parametrization (BEP) models (Martilli et al., 2002)), which better capture the transport of heat, moisture and momentum through the urban canopy compared to single layer models. To take full advantage of the multi-layer models, a high vertical resolution is required, such that multiple grid layers are in the urban canopy, thereby putting a strain on the resolution.

With the tendency to run large-scale weather models at increasingly higher resolutions, it becomes more compelling to use an urban parametrisation scheme to investigate urban heat island effects inside a city or even within a single urban canyon. However, large scale parametrisation schemes are not explicitly designed to represent a single canyon, but are typically used to compute the overall impact of multiple canyons on the atmosphere above. To investigate the ability of such a large scale parametrisation scheme to represent one single urban canyon, this study compares the SLUCM parametrisation scheme (Kusaka et al., 2001) to URBSIM (the micro-scale model that is developed in this thesis (Schrijvers et al., 2015, 2016, 2020a)).

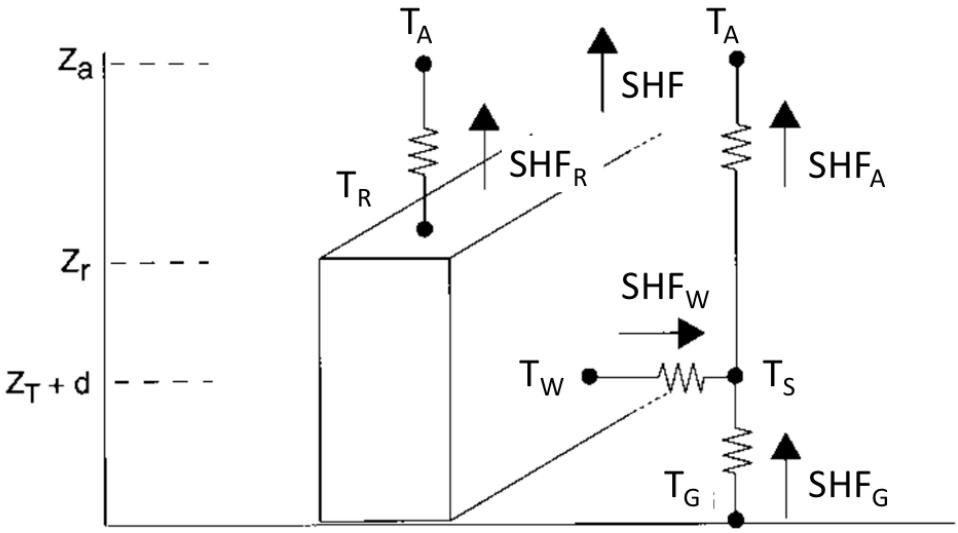

Fig. 5.1: Overview of the Single Layer Urban Canopy Model (SLUCM) by Kusaka et al. (2001). T_A is the air temperature at reference height z_a, T_R the building roof temperature, T_W the building wall temperature, T_G the road temperature and T_s the temperature defined at $z_T + d$. SHF is the sensible heat flux at the reference height, SHF_A the sensible heat flux from the canyon to the atmosphere, similarly SHF_W that from wall to canyon space, SHF_G from road to canyon space and SHF_R from roof to the atmosphere.

The goal is to gain insight in the level of complexity taken into consideration in the SLUCM parametrisation and to identify possible areas of improvement. This initial investigation also serves as a basis for more advanced coupling studies between large-scale models and the developed micro-scale model.

The SLUCM parametrisation is used as a reference model, since it is one of the standard urban canopy models that is available in the Weather and Research Forecast model (WRF), and is a widely used meso-scale model (Skamarock et al., 2005). Furthermore, the SLUCM parametrisation is also used within the Climate Proof Cities program (Ronda et al., 2012), which enables a future coupling between the two models.

Section 5.2 discusses results for absorbed radiation inside the canyon (both shortwave and longwave radiation) for a range of H/W ratios and the two different models. Canyon wind speeds are computed in the parametrisation scheme and micro-scale model, and results are presented in Section 5.3 for different free stream wind speeds and H/W ratios, while the sensible heat flux is discussed in Section 5.4 with the same cases as discussed in Section 5.3. The conductive heat flux is computed with the same method in both models and is therefore not compared here. This chapter ends with concluding remarks, recommendations for improving the SLUCM parametrisation scheme and an outlook to future work. Since the URBSIM micro-scale model is discussed already in Chapters 2, 3 and 4, mainly the SLUCM parametrisation will be discussed, and the framework that is used to compare both models.

5.2 Radiative transfer

5.2.1 Longwave radiation

Within the SLUCM radiation computation, distinction is made between three different obstacles surfaces inside the urban canyon (ground, wall and roof) and between longwave radiation emitted by the sky and obstacle surfaces. One reflection is taken into account, i.e. multiple reflections are neglected. The absorbed longwave radiation is:

$$L^{\text{sky}}_{\text{wall}} = \epsilon_{\text{w}} L_{\text{down}} \left[F^{\text{b}}_{\text{ws}} + (1-\epsilon_g) F^{\text{b}}_{\text{gs}} F^{\text{b}}_{\text{wg}} + (1-\epsilon_w) F^{\text{b}}_{\text{ws}} F^{\text{b}}_{\text{ww}} \right] \quad (5.1)$$

$$L^{\text{sky}}_{\text{ground}} = \epsilon_{\text{g}} L_{\text{down}} \left[F^{\text{b}}_{\text{gs}} + (1-\epsilon_w) F^{\text{b}}_{\text{ws}} F^{\text{b}}_{\text{wg}} \right] \quad (5.2)$$

$$\begin{aligned} L^{\text{trap}}_{\text{wall}} &= \epsilon_{\text{w}} \epsilon_{\text{g}} \sigma T^4_{\text{g}} F^{\text{b}}_{\text{ws}} + \epsilon_{\text{w}} \epsilon_{\text{w}} \sigma T^4_{\text{w}} F^{\text{b}}_{\text{ww}} + \epsilon_{\text{w}} (1-\epsilon_{\text{g}}) \epsilon_{\text{w}} \sigma T^4_{\text{w}} F^{\text{b}}_{\text{ws}} F^{\text{b}}_{\text{wg}} \\ &+ \epsilon_{\text{w}} (1-\epsilon_{\text{w}}) \epsilon_{\text{g}} \sigma T^4_{\text{g}} F^{\text{b}}_{\text{ws}} F^{\text{b}}_{\text{ww}} + \epsilon_{\text{w}} (1-\epsilon_{\text{w}}) \epsilon_{\text{w}} \sigma T^4_{\text{w}} F^{\text{b}}_{\text{ww}} F^{\text{b}}_{\text{ww}} \quad (5.3) \end{aligned}$$

$$\begin{aligned} L^{\text{trap}}_{\text{ground}} &= \epsilon_{\text{g}} \epsilon_{\text{w}} \sigma T^4_{\text{w}} F^{\text{b}}_{\text{wg}} + \epsilon_{\text{g}} (1-\epsilon_{\text{w}}) \epsilon_{\text{g}} \sigma T^4_{\text{g}} F^{\text{b}}_{\text{wg}} F^{\text{b}}_{\text{ww}} \\ &+ \epsilon_{\text{g}} (1-\epsilon_{\text{w}}) \epsilon_{\text{w}} \sigma T^4_{\text{w}} F^{\text{b}}_{\text{ww}} F^{\text{b}}_{\text{wg}} \quad (5.4) \end{aligned}$$

where L_{down} is the downward atmospheric longwave radiation, F the bulk view factor for the entire surface, ϵ the emissivity and T the temperature. The used notation indicates the ground surface, sky, and wall by subscripts g, s and w, respectively. $L^{\text{trap}}_{\text{ground}}$ is the absorbed radiation at the ground surface due to longwave trapping (radiation emitted from the wall or ground which is reflected back to the ground).

In the paper by Kusaka et al. (2001), it is stated that the view factors are computed following Sakakibara (1996),

$$F^{\text{b}}_{\text{ws}} = \int_{z=0}^{H} \left[\frac{1}{2} \times \left(1 - \frac{z}{\sqrt{z^2 + W^2}} \right) \right] \text{d}z \quad (5.5)$$

$$F^{\text{b}}_{\text{wg}} = \int_{w=0}^{W} \int_{z=0}^{H} \left[\frac{1}{2} \times \left(1 - \frac{H-z}{\sqrt{(H-z)^2 + (W-w)^2}} \right) \right] \text{d}z\text{d}w \quad (5.6)$$

$$F^{\text{b}}_{\text{ww}} = 1 - F^{\text{b}}_{\text{ws}} - F^{\text{b}}_{\text{wg}} \quad (5.7)$$

$$F^{\text{b}}_{\text{gs}} = 1 - F^{\text{b}}_{\text{wg}} \quad (5.8)$$

where W the width of the canyon, H the canyon height and subscripts w, s and g are used for respectively the wall, sky and ground. The view factor equations are integrated numerically by using z=0 to H and w=0 to W, which results in one bulk view factor for each surface. The computed view factor is then used in the computation of the absorbed longwave radiation for the entire surface (equations 5.1 to 5.4), following Kusaka et al. (2001). The view factor F_{ws} is read as the view factor from wall to sky, and is equal to the view factor from sky to wall. The view factor varies between 0 and 1.

However, these are not the equations that are actually implemented in the numerical scheme that is used within WRF (WRF version 3.8.1, released August 11, 2016). Within the WRF implementation, the view factors are computed by:

$$F^{\mathrm{b}}_{\mathrm{ws}} = \int_{z=0}^{H} \left[\frac{1}{2} \times \left(1 - \frac{z}{\sqrt{z^2 + W^2}} \right) \right] \mathrm{d}z \tag{5.9}$$

$$F^{\mathrm{b}}_{\mathrm{ww}} = 1 - F^{\mathrm{b}}_{\mathrm{ws}} - F^{\mathrm{b}}_{\mathrm{ws}} \tag{5.10}$$

$$F^{\mathrm{b}}_{\mathrm{gs}} = 1 - 2F^{\mathrm{b}}_{\mathrm{ws}} \frac{H}{W} \tag{5.11}$$

$$F^{\mathrm{b}}_{\mathrm{wg}} = 1 - F^{\mathrm{b}}_{\mathrm{gs}} \tag{5.12}$$

Where Eq. 5.5 and Eq. 5.9 are identical. Integrating equation 5.9, gives

$$F^{\mathrm{b}}_{\mathrm{ws}} = \sqrt{(H/W)^2 + 1} - H/W \tag{5.13}$$

which is identical to the formulation as used in the Town Energy Balance (TEB) model by Masson (2000), where the view factor is named Ψ_r. Furthermore, Equation 5.11 (the computation of $F^{\mathrm{b}}_{\mathrm{gs}}$) is identical to equation 5.6, and to the equation of the view factor from the TEB model. Even though the SLUCM and TEB model use quite different formulations and different literature references, the end result gives identical sky view factor computations.

Using equations 5.1 to 5.4, the longwave radiation is computed and compared to the Monte-Carlo calculation results. Results for the absorbed longwave radiation that is emitted from the sky as a function of the H/W ratio is presented in Fig. 5.2 . A uniform emissivity of ϵ=0.95 is used for all surfaces and L_{down}=300Wm^{-2}. The amount of absorbed radiation at the roof is independent of the H/W ratio and is only a function of the emissivity. Results show excellent agreement between the absorbed radiation from the parametrisation scheme and Monte-Carlo model. The Monte-Carlo model provides information on both vertical walls. However, since a symmetric street canyon is investigated, results for both walls are identical.

The radiation absorbed from the longwave trapping effect (radiation emitted at one surface and absorbed at an other) is displayed in Fig. 5.3, where a uniform surface temperature is used of 300K. The used emissivity of ϵ=0.95 for all canyon surfaces results in an emitted longwave radiation of 436.3Wm^{-2}. The radiation absorbed due to the longwave trapping effect is 0 at roof level and therefore not displayed here.

The longwave trapping effect shows excellent agreement between the two models, with differences of less than 10 Wm^{-2} for all H/W ratios.

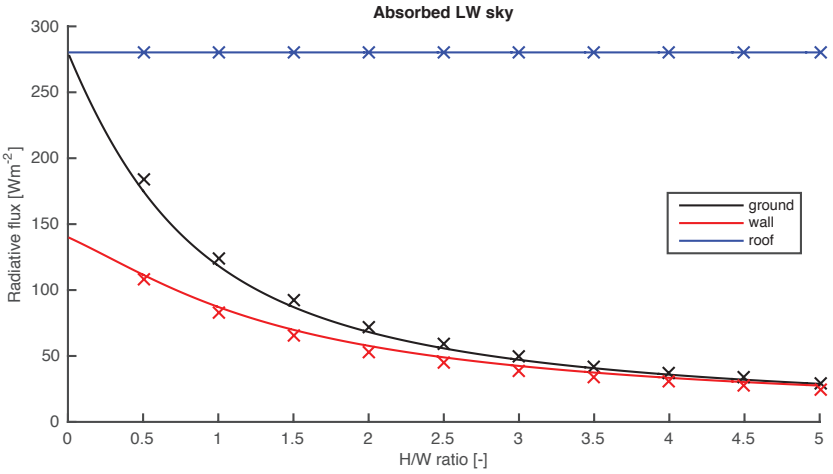

Fig. 5.2: Absorbed longwave radiation from the sky averaged for the three complete canyon surfaces for the Monte-Carlo model (crosses) and Kusaka radiation parametrisation (lines)

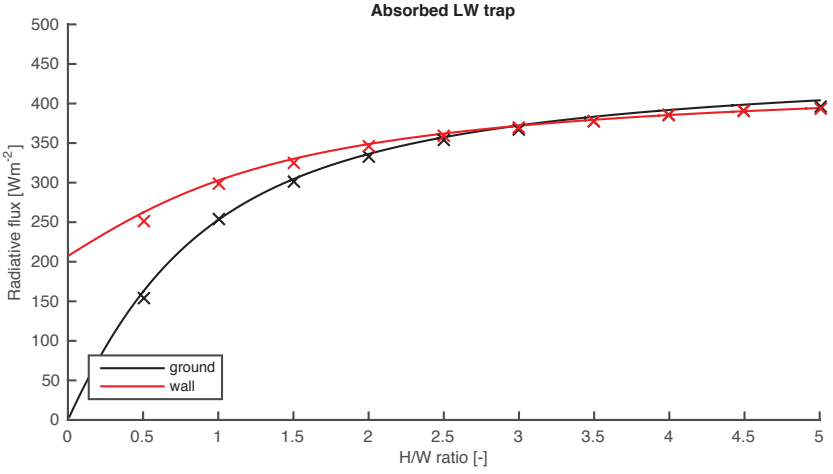

Fig. 5.3: Absorbed radiation due to the longwave trapping effect for the SLUCM radiation parametrisation (lines) and Monte-Carlo model (crosses).

5.2.2 Shortwave radiation

For the computation of direct shortwave radiation, a shadow length is introduced in the SLUCM scheme, which is computed based on the location of the sun. The shadow length indicates how much of the canyon does not receive direct shortwave radiation, and is computed by

$$l_{\text{shadow}} = \begin{cases} h \tan\theta_z \sin\theta_n & l_{\text{shadow}} < w \\ w & l_{\text{shadow}} > w \end{cases} \tag{5.14}$$

where h is the normalized building height (such that $h + w{=}1$), θ_z is the solar zenith angle and θ_n the angle between the solar azimuth angle and the canyon orientation, which is set to π in this study, such that $\sin\theta_n{=}1$.

In the SLUCM model, a distinction is made between the direct and diffuse component as

$$\begin{aligned}
S^{\text{dir}}_{\text{ground}} &= S_{\text{D}} \frac{w - l_{\text{shadow}}}{w}(1-\alpha_{\text{g}}) + S_D \frac{l_{\text{shadow}}}{2h}\alpha_{\text{w}} F_{\text{wg}}(1-\alpha_{\text{g}}) && (5.15)\\
S^{\text{dif}}_{\text{ground}} &= S_{\text{Q}} F_{\text{gs}}(1-\alpha_{\text{g}}) + S_{\text{Q}} F_{\text{ws}}\alpha_{\text{w}} F_{\text{ws}}(1-\alpha_{\text{g}}) && (5.16)\\
S^{\text{dir}}_{\text{wall}} &= S_D \frac{l_{\text{shadow}}}{2h}(1-\alpha_{\text{w}}) + S_{\text{D}} \frac{w - l_{\text{shadow}}}{w}\alpha_{\text{g}} F_{\text{ws}}(1-\alpha_{\text{w}}) \\
&+ S_D \frac{l_{\text{shadow}}}{2h}\alpha_{\text{w}} F_{\text{ww}}(1-\alpha_{\text{w}}) && (5.17)\\
S^{\text{dif}}_{\text{wall}} &= S_{\text{Q}} F_{\text{ws}}(1-\alpha_{\text{w}}) + S_{\text{Q}} F_{\text{ws}}(1-\alpha_{\text{w}}) \\
&+ S_{\text{Q}} F_{\text{ws}}\alpha_{\text{w}} F_{\text{ww}}(1-\alpha_{\text{w}}) && (5.18)
\end{aligned}$$

where S^{dif} is used for the absorbed diffuse component, S_Q the incoming diffuse shortwave radiation, S^{dir} the absorbed direct shortwave component, S_D the incoming direct shortwave radiation and α the albedo. One reflection of shortwave radiation is taken into account, which means that the label S^{dir} is the direct shortwave radiation and one reflection (even though the reflection is technically diffuse radiation). The naming convention and subscripts are identical to the longwave radiation, discussed in Section 5.2.1.

Results for the absorbed diffuse shortwave radiation on the individual building facades are shown in Fig. 5.4, where a uniform albedo is used of $\alpha{=}0.4$ and $S_{\text{Q}}{=}100\text{Wm}^{-2}$. There is a reasonable agreement between the SLUCM scheme and Monte-Carlo model, where the absorbed radiation at the ground is better represented than the vertical walls. The amount of

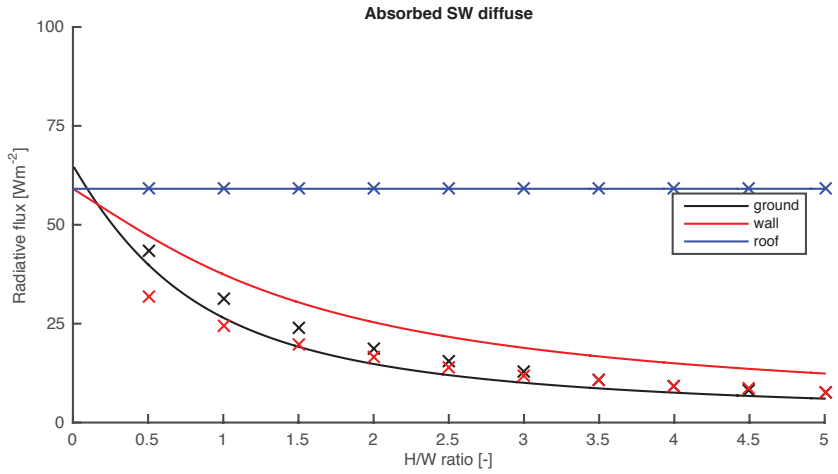

Fig. 5.4: Absorbed diffuse shortwave radiation for the Monte-Carlo model (crosses) and Kusaka radiation parametrisation (lines) for the three canyon surfaces.

absorbed radiation on the vertical wall is larger in the SLUCM scheme for all H/W ratios, with a maximum difference of 20Wm^{-2} for H/W=0.5.

For the comparison of direct shortwave radiation (see Fig. 5.5), a radiative input of $S_{\mathrm{D}} = 800\mathrm{Wm}^{-2}$ is used and a solar zenith angle of 33 degrees. The first thing that strikes the attention is the large difference due to the shading effect on one of the two vertical walls, while there is no distinction between the two vertical surfaces within the SLUCM scheme. When the absorbed radiation at the two vertical walls is averaged from the Monte-Carlo model (x), results show higher values for the Monte-Carlo model for H/W <2.0, with differences of up to 50Wm^{-2}. For larger H/W ratios (where the ground is completely shaded), the two models show nearly perfect agreement. The absorbed direct radiation at the ground is decreasing very rapidly for increasing H/W up to a value of 1.75, which is due to the increasing shadow length. For H/W >1.75, the entire ground surface is shaded, and the SLUCM scheme computes values of absorbed radiation very close to zero. Absorbed radiation from the Monte-Carlo model is slightly higher, which is due to multiple reflections. In the SLUCM scheme, a single reflection is taken into account, and $S_{\mathrm{D}} \times \alpha \times \alpha$=128Wm^{-2} is reflected from the surfaces. Since the direct shortwave radiation is the largest source of energy to the system, it can be considered to include 2 reflections in the SLUCM scheme, such that the energy discarded in that case reduces to 50Wm^{-2}. Off course, taking into account more reflections will increase the

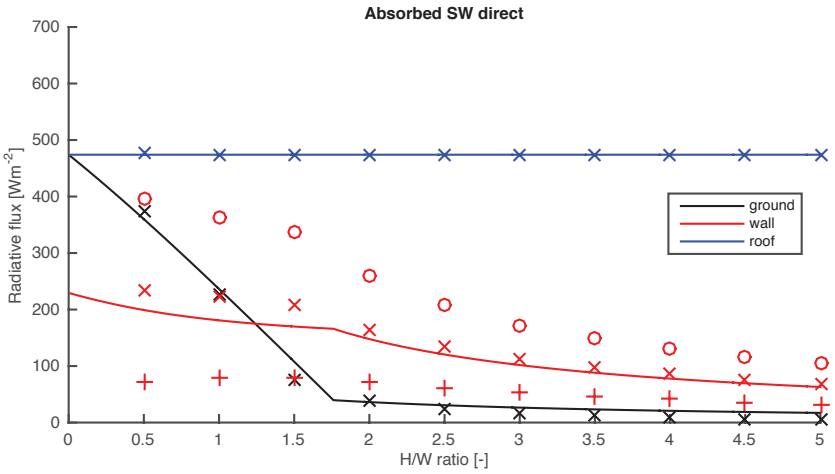

Fig. 5.5: Absorbed direct shortwave radiation for the Monte-Carlo model (o indicates sunlit wall, + shadowed wall and x the value for the complete surface) and Kusaka radiation parametrisation scheme (lines) for the three canyon surfaces.

accuracy.

5.2.3 Total absorbed shortwave and longwave radiation

The total absorbed shortwave and longwave radiation as computed in the Monte-Carlo model and from equations 5.1 - 5.4 and eqs 5.14 - 5.18 are compared for the ground, vertical walls (the average of both walls is taken in the Monte-Carlo model) and the roof (see fig. 5.6). The largest component at ground level is the direct shortwave radiation, from which also the sharp distinction between sunlit ($H/W \leq 1.75$) and shaded area is originating from. The total absorbed radiation matches well between both models. For the vertical walls, longwave trapping and direct shortwave radiation provide equal contributions to the total absorbed radiation. There are small differences present, but in general there is excellent agreement between the two models.

The good agreement could have been expected beforehand. The radiation parametrisation computes the different view factors, and uses these to compute the absorbed radiation at a surface. One assumption is made, which is the number of reflections that are taken into account (one reflection in the SLUCM parametrisation). Within the Monte-Carlo model, the view factor is computed by brute force, and there is no limit in the number of reflections that are taken into account. When reflections play no role

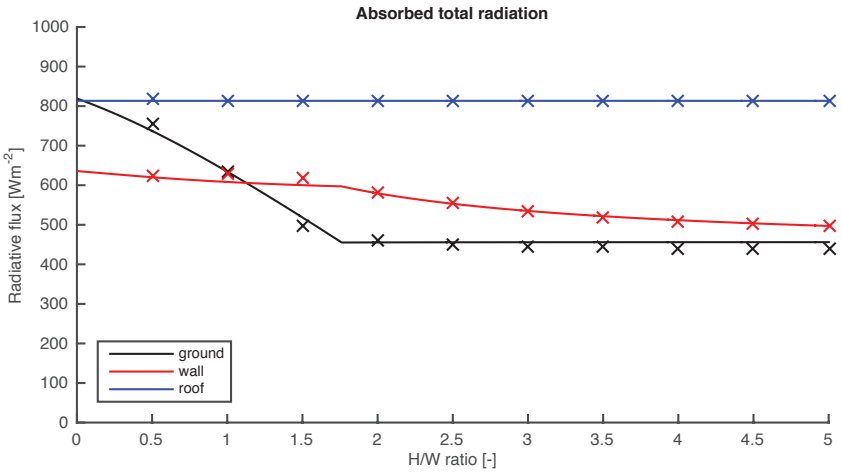

Fig. 5.6: Total absorbed radiation for the Monte-Carlo model and the Kusaka radiation parametrisation scheme (lines) for the three canyon surfaces.

(perfect absorption at the surface, ϵ=1, α=0), the results of SLUCM and Monte-Carlo simulations are identical. The models deviate when reflections become important due to the one reflection assumption in the SLUCM. This is the reason that the shortwave radiation components show larger discrepancies compared to the longwave radiation components. When the geometry becomes more complex (for instance by placing a balcony at one vertical surface), the number of view factors that have to be computed increases rapidly, while it is very straightforward to take multiple surfaces into account within the Monte-Carlo model. Therefore, the Monte-Carlo method can be seen as a more suitable approach for complex geometries, for which the number of view factor calculations are large and not straightforward.

5.3 Canyon wind speed

The wind speed at half the building height (U_s) is computed in the SLUCM parametrisation scheme, based on the wind profile equation proposed by Swaid (1993)

$$U_s = U_r \exp\left(-0.386\frac{H}{W}\right) \tag{5.19}$$

where U_r is the wind speed at roof level. Note that within the large-scale model, U_r is a function of the free stream wind speed above the urban canyon and Monin-Obukhov similarity functions. This is not taken into account

here, but instead wind speed at roof level is directly specified in the SLUCM scheme.

To compare the wind speed parametrization at the mid-level of the canyon according to Eq. 5.19 to the micro-scale CFD model, a range of wind speeds at roof level are used. Within the micro-scale model, U_r can't be directly specified. Instead, we found that if we set the free stream wind speed at the inlet to $2U_r$, we obtain approximately the desired U_r. Fixed surface temperatures ($T_\mathrm{g} = 300\mathrm{K}$, $T_\mathrm{w} = 295\mathrm{K}$) and an inlet air temperature of $T_\mathrm{a} = 293\mathrm{K}$ are used. Buoyancy forces are neglected in this study, i.e. temperature is a passive scalar. Buoyancy forces are also neglected in Eq. 5.19, in which non-thermal flow was assumed. As a result, a relatively simple framework is obtained to test the wind speed and (in the next section) the sensible heat flux parametrisation used in the SLUCM scheme.

Fig 5.7 displays the velocity profile (with $U_s = \sqrt{U_x^2 + U_z^2}$ the velocity magnitude) in the middle of the street canyon for H/W=1.0 as obtained from the micro-scale model, where the black line indicates the wind speed. The minimum wind speed is close to $H/2$, which is the centre of the vortex. Below $H/2$ there is counter flow due to the recirculating vortex. To obtain a realistic velocity scale at $H/2$, the local wind speed profile is averaged over the canyon height (blue crosses), which is believed to be a more representative value of the canyon wind speed compared to the actual wind speed at $H/2$.

The first investigation concerns the SLUCM parametrisation of the wind speed inside the canyon. Therefore, the wind speed at roof level is varied for the case with H/W=0.5. Results are presented in the left panel of Fig. 5.8, which shows wind speed at roof level (black) and the canyon wind speed (blue) for both the SLUCM scheme (lines) and micro-scale model (crosses). The wind speed at roof level is difficult to control in the micro-scale model, since only the wind speed at the inlet is prescribed. Therefore, the values of U_r used in the parametrisation scheme are matched to the resulting U_r from the micro-scale model. As a result, U_r reveals a perfect agreement between the two models. In the SLUCM scheme, canyon wind speed is reduced by 18% compared to wind speed at roof level. The reduction is not a function of free stream wind speed, and is much smaller compared to the micro-scale model which reveals a reduction of 64%. The difference is most likely explained by the use of a 2D street canyon to obtain results for the 3D environment within the SLUCM scheme. For a 3D environment, air flow is able to penetrate the canyon from the sides, thereby allowing for larger wind speeds inside the canyon. This is inhibited by the 2D geometry, which results in wind speeds that are much lower.

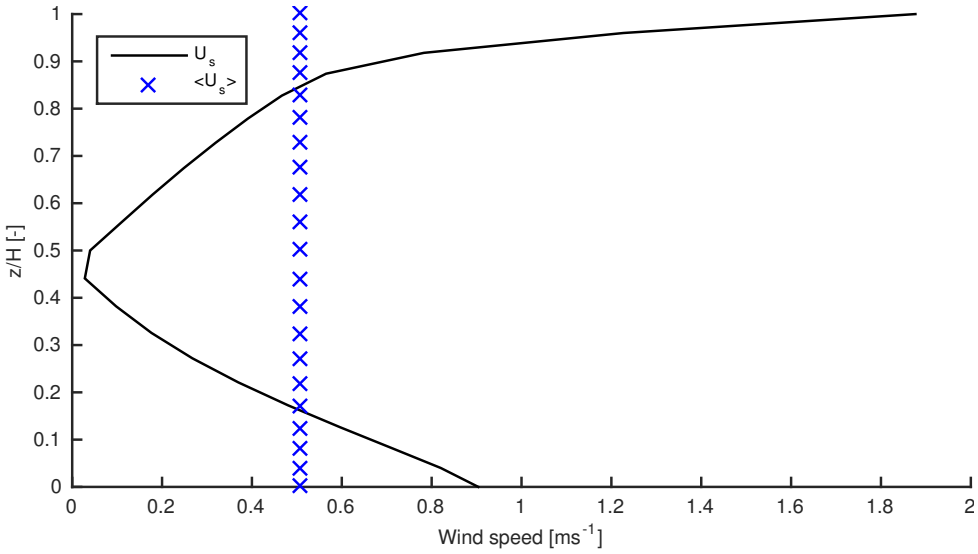

Fig. 5.7: Velocity profile in the center of a street canyon with H/W=0.5 and U_r=2.0 ms^{-1}. The black line indicates the wind speed profile computed from CFD, the blue crosses are used as the representative velocity scale, and is the height-averaged value of the CFD velocity profile.

As a next test case, the H/W ratio is varied, while using a constant inlet wind speed of 4.0 ms^{-1} in order to achieve U_r=2.0 ms^{-1}. Results are shown in the right panel of Fig. 5.8, which demonstrates that the micro-scale model does not exactly match the desired velocity at roof level. Therefore, U_r in the SLUCM scheme is set to 1.8 ms^{-1}. The wind speed from the SLUCM scheme is exponentially decreasing with increasing H/W ratio, where the canyon wind speed at H/W=2.0 is 50% of the wind speed at roof level. The micro-scale model shows lower wind speeds inside the canyon, where the decrease is nearly linear with increasing H/W ratio. Again, this can be largely contributed to 3D effects, which are not taken into account in the geometry for the micro-scale model.

5.4 Sensible heat flux

The sensible heat flux is computed in the SLUCM scheme by a heat transfer coefficient and the temperature difference between the obstacle surface and replaced canyon surface temperature T_s (T_s is further discussed in Section 5.4.1)

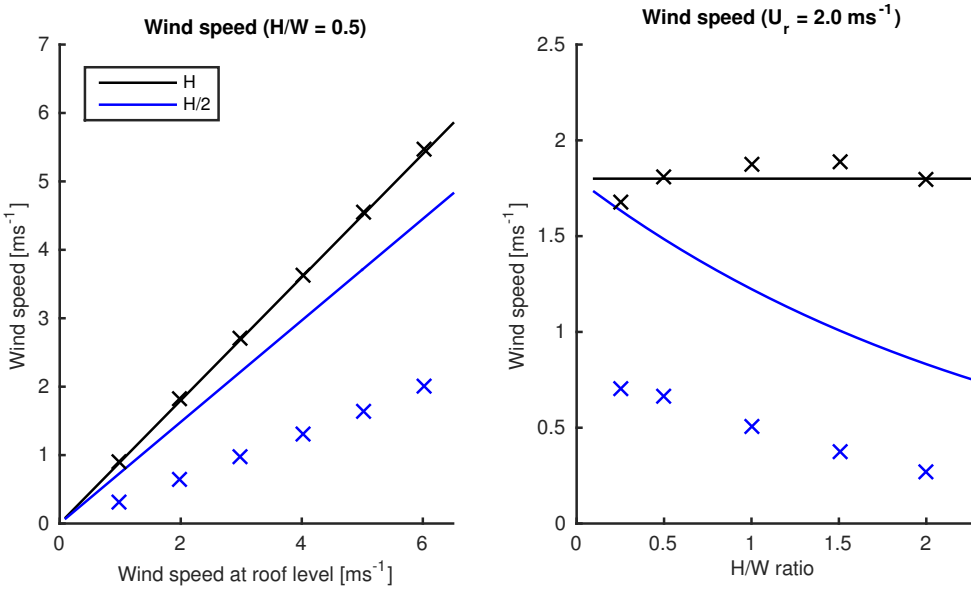

Fig. 5.8: Wind speed at roof level and mid-canyon as a function of roof level wind speed (left panel) and as a function of H/W ratio (right panel). The lines shows results from the SLUCM parametrisation, crosses are used for results from the micro-scale model.

$$H_{\mathrm{w}} = C_{\mathrm{w}}(T_{\mathrm{w}} - T_{\mathrm{s}}) \tag{5.20}$$
$$H_{\mathrm{g}} = C_{\mathrm{g}}(T_{\mathrm{g}} - T_{\mathrm{s}}) \tag{5.21}$$

where the heat transfer coefficient C is computed by

$$C_{\mathrm{g}} = C_{\mathrm{w}} = \begin{cases} 7.50 U_s^{0.78} & (U_s > 5\mathrm{ms}^{-1}) \\ 6.15 + 4.18 U_s & (U_s \leq 5\mathrm{ms}^{-1}) \end{cases} \tag{5.22}$$

with U_s the wind speed at half the building height as computed from Eq. 5.19. Note that there is no difference in the heat transfer coefficient between the different surfaces. Furthermore, the equations for the sensible heat flux are missing a factor ρc_{p}, which is most likely incorporated in the pre-factor values used in the computation of the heat transfer coefficient. In addition, for wind speeds >5 ms^{-1}, the equation for the heat transfer coefficient is dimensionally incorrect, indicating that the factor 7.50 does not only include the factor ρc_{p} but also other factors.

In the current test case, a fixed surface temperature is used and there is no feedback from radiation, conductive heat flux or from the sensible heat flux on the surface temperature. Although the effects of these processes are present in the full SLUCM parametrisation scheme, this simplified test case provides insight in the difficulties involved within the SLUCM parametrisation assumptions. It can be that possible errors in the computation of the sensible heat flux are compensated through feedback effects, but these are not taken into account here.

Only equations 5.19 to 5.21 are used to compute the sensible heat flux in the simplified test case that is used in this study. For full clarity, the paragraph below present the full computation of the sensible heat flux in the SLUCM scheme, which includes radiation and energy transfer from the overlying atmosphere to the canyon. However, for the current comparison, it is believed that the simplified test case provides more insight in the SLUCM scheme.

5.4.1 Full computation of the sensible heat flux within the SLUCM scheme

The replaced canyon surface temperature T_{s} that is used in Eq. 5.20 and 5.21 is computed from the canyon surface energy balance and the sensible heat flux between the urban canyon and overlaying air

$$R_{\mathrm{n,i}} = H_i + Le_i + G_i \tag{5.23}$$

where R_{n} is the net absorbed radiation that is computed from the equations presented in section 5.2, H the sensible heat flux, Le the latent heat flux, G the conductive heat flux and i denotes the different surfaces. The sensible heat flux of individual surfaces can heat or cool the canyon, which can create a sensible heat flux from the canyon to the overlaying atmosphere. The sensible heat flux between the canyon and atmosphere above is computed as

$$wH_a = 2hH_{\mathrm{w}} + wH_{\mathrm{g}} \tag{5.24}$$

in which H_a is the sensible heat flux from the canyon to the atmosphere, H_{w} the sensible heat flux from the vertical wall and H_{g} the sensible heat flux from the ground. The total sensible heat flux to the atmosphere is area weighted with the height of the vertical walls (h) and the length of the ground surface (w).

The sensible heat exchange between the canyon and overlaying atmosphere is computed as

$$H_a = \rho c_p \frac{k u_*}{\Psi_h} (T_s - T_a) \tag{5.25}$$

where u_* is the friction velocity, k the Von Karman constant (with a value of 0.41), ρ and c_p the density and heat capacity of air respectively and Ψ_h the integrated universal function. This universal function uses the Obukhov stability length, which is computed as

$$L = \frac{\rho c_p T_m u_*^3}{k g H_a} \tag{5.26}$$

where T_m is the mean temperature and g the gravitational acceleration.

In this balance, H_a is a function of Ψ_h which is again a function of H_a. The equations are solved iteratively within the SLUCM parametrisation, thereby computing a replaced canyon temperature T_s. This parameter can be seen as an effective surface temperature of the canyon, but has no real physical interpretation.

5.4.2 Results

To simplify the sensible heat flux computation for the current investigation, it is assumed that the replaced canyon surface temperature (T_s in Eq. 5.20 and 5.21) in the SLUCM scheme is identical to the free stream air temperature in the URBSIM model (293.15K). Since the replaced canyon surface temperature can be seen as an effective surface temperature of the canyon, it is expected that T_s has a value between the air temperature (lowest temperature in the canyon) and the surface temperature (highest temperature inside

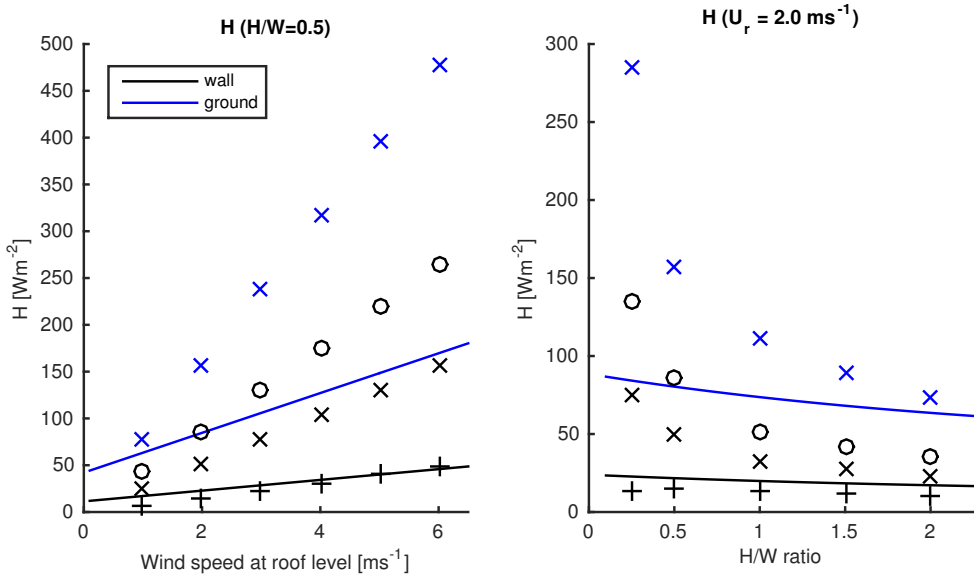

Fig. 5.9: Sensible heat flux at ground and wall as a function of roof level wind speed. Lines are used for the SLUCM results (with colors according to the legend in the top left panel). Micro-scale model results are depicted with symbols, where the distinction is made between the windward wall (black, o), leeward wall (black, +) and the average value of these two walls (black, x for the vertical wall, blue, x for the ground surface).

the canyon). To provide a conservative agreement, the air temperature is assumed for T_s. As a second simplification, the surface temperatures in the URBSIM model have a fixed value, which is identical to the surface temperatures that are used in the SLUCM parametrisation scheme.

The resulting sensible heat flux, as a function of wind speed at roof level, is displayed in the left panel of Fig. 5.9, and shows the sensible heat flux for the ground surface (which has a surface temperature of 300K) and vertical walls (with a surface temperature of 295K). Similar to the radiative transfer comparison, the micro-scale model results are split between the two vertical walls (o for the windward wall, + for the leeward wall), while there is no distinction between the two vertical surfaces in the SLUCM parametrisation.

The sensible heat flux as computed from the SLUCM scheme and micro-scale model differ by as much as 250% for the ground surface and 350% for the vertical walls, where the micro-scale model results in a heat flux that is much larger. Both models do show a linear increase in the sensible heat flux with increasing wind speed.

To obtain the same values of the heat flux in the SLUCM scheme as obtained by the micro-scale model for the ground surface and U_r=6.0 ms^{-1}, there are three options.

- The temperature difference ($T_g - T_s$) should increase to 19K
- The wind speed inside the canyon should increase to 16.9 ms^{-1}
- A combination of the above points

The temperature difference can only increase by lowering the replaced canyon surface temperature T_s (since the surface value of T_g is fixed in this case) below the air temperature and below the surface temperature of the canyon surfaces. The increase in wind speed inside the canyon, is far above the windspeed at roof level and therefore also not realistic. It may be that our simplified test case with fixed surface temperatures is too simplistic for the SLUCM scheme, which requires further investigation.

The same remark that was made when investigating the direct shortwave radiation also holds here: there is a large distinction between the two vertical walls. Relatively cold free stream air is forced over the windward wall, resulting in a larger sensible heat flux at that surface. Air is heated inside the canyon, thereby reducing the temperature difference between air and the leeward wall, resulting in a smaller sensible heat flux over the leeward wall. This distinction between the two vertical walls is not taken into account in the SLUCM parametrisation scheme.

When the H/W ratio is varied (right panel of Fig. 5.9), the sensible heat flux decreases for increasing H/W ratio, where the micro-scale model displays a much faster decrease in the sensible heat flux than the SLUCM scheme. For H/W >2.0, it was found that 3D effects become important (Schrijvers et al., 2015) and are therefore not considered here.

Fig. 5.10 shows the heat transfer coefficient as a function of wind speed. The heat transfer coefficient in the SLUCM parametrisation scheme is computed as in Eq. 5.22, and is divided by the term ρc_p (which is missing in Eq. 5.22). The heat transfer coefficient in the micro-scale model is computed by taking the vertically averaged air temperature in the centre of the street canyon (similar to the computation of the canyon wind speed), and compute the heat transfer coefficient following

$$C_i = \frac{H_i}{\rho c_p (T_{s,i} - T_a)} \tag{5.27}$$

where i indicates the ground or wall surface.

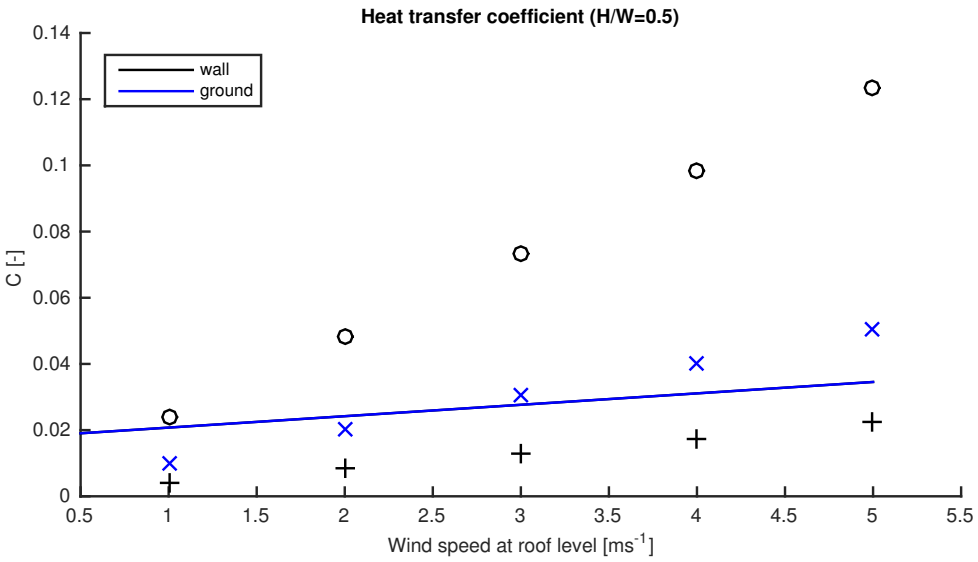

Fig. 5.10: Heat transfer coefficient at ground and wall as a function of roof level wind speed. Lines are used for the parametrisation scheme, while symbols are used for the windward wall (o), leeward wall (+) and the ground (x).

Note that the parametrisation scheme makes no distinction between the ground and walls, and therefore only displays one heat transfer coefficient in Fig. 5.10. It can be seen from the micro-scale model that the lack of distinction between the two walls and ground surface is far from valid, where differences between the windward wall (o), leeward wall (+) and ground surface (x) are significant. All surfaces do show a linear relation between the heat transfer coefficient and wind speed, where the gradient of the parametrisation scheme closely follows that of the leeward wall.

As a reference, the heat transfer coefficient for a flat terrain is computed by $\frac{1}{r_a}$, where r_a is the aerodynamic resistance. The aerodynamic resistance has a typical value of r_a=50ms^{-1} (depends on the roughness length and the monin-obukhov length) (van Heerwaarden et al., 2009), which gives a value for the heat transfer coefficient of C=0.02 and is in the same range as obtained here for H/W=0.5.

As was the case for the wind speed, it must be kept in mind that the SLUCM parametrisation scheme is developed for larger 3D environments, consisting of (at least) 500×500 meter (which is the typical grid resolution of WRF). Therefore, using a single 2D canyon with a fixed surface temperature

to evaluate the accuracy for the sensible heat flux might be misleading. Furthermore, compensating effects are not taken into account (such as a decreasing surface temperature as a result of a positive sensible heat flux), thereby magnifying the differences between the parametrisation scheme and micro-scale model further.

5.5 Concluding remarks and future work

First results are presented comparing the Single Layer Urban Canopy Model parametrisation scheme proposed by Kusaka et al. (2001) and the developed micro-scale model in this thesis. In general, radiation is well resolved by the parametrisation scheme. Although differences in absolute values are present (up to 50 Wm^{-2} for the absorbed direct shortwave radiation), trends in absorbed shortwave and longwave radiation as a function of H/W ratio are well captured.

Results for canyon wind speed and sensible heat flux deviated more in both models, which is most likely due to the 2D geometry that is tested. Although this 2D geometry is used in the SLUCM scheme, it represents a large 3D environment and the coefficients used in the SLUCM scheme are most likely altered to obtain realistic results for that 3D environment. The used micro-scale model uses the actual 2D geometry. In addition, a fixed surface temperature is used in the presented test case in URBSIM and the SLUCM computation, which does not allow for compensating mechanisms. Despite these simplifications, general trends of the wind speed and sensible heat flux are well captured between both models, although absolute numbers can differ by a large extent.

Some possible areas of improvement were found for the SLUCM scheme. The distinction between the two vertical walls might be worth while to include. Differences between the two walls are present in the absorbed direct shortwave radiation and in the sensible heat flux. By differentiating these two walls, more detailed results can be obtained, especially for lower H/W ratios where large effects of radiation were found. The distinction between the two walls has been explored by Marciotto et al. (2010), who found differences in absorbed shortwave radiation of 40 Wm^2 averaged over all canyon directions between the Town Energy Balance model (Masson, 2000) (which does not take make the distinction) and the modified Urban Canopy Model, where the Urban Canopy Model shows higher values (closer to the Monte-Carlo model). The formulation of the heat transfer coefficient is equal for both vertical walls in the modified model by Marciotto et al. (2010), but due to the different surface temperatures that are allowed between the two vertical

walls, different sensible heat fluxes are possible. As a further extension, the heat transfer coefficient could be differentiated between the two vertical walls and the ground surface.

The 3D environment is taken into account in the SLUCM parametrisation by only 2 parameters: building height (H) and street width (W). A third parameter is essential: building length (or more generic: plan area density, which is the percentage of build area in a grid box). The third parameter allows a more detailed description for the amount of 'blocking' in the urban environment, that can especially help computation of wind speeds and the sensible heat flux.

This preliminary study creates a first step towards more detailed coupling studies. Two next steps can be foreseen: test the coupled 2D SLUCM representation of the urban canyon and perform comparison between both models for a large 3D environment, similar to the study conducted here. One could also investigate direct coupling of both models. The coupling-approach of different models is explored by many people. A nice overview is given by Chen et al. (2011), where the integrated WRF/urban modelling system is discussed. The coupling often serves a two-fold goal 1) use of forecasts for initial and boundary conditions to improve micro-scale simulations through downscaling and 2) feedback, through up scaling, of explicitly resolved turbulence and wind fields from the micro-scale in order to improve forecasting in complex urban environments.

Chapter 6

Concluding remarks and future work

6.1 Concluding remarks

The goal of this thesis is to gain insight in the local urban climate and to identify processes that govern the surface heat budget. For this purpose, a building resolving model (URBSIM) has been developed that combines computation of radiative transfer, heat conduction and ventilation effects. Details of this model, including validation, are discussed in Chapter 2. The model is expanded by computing mean radiant temperature inside the urban canyon (Chapter 3). Computation of the Universal Temperature Climate Index (UTCI) is added in Chapter 4, which is an apparent temperature that relates local air temperature, mean radiant temperature and wind speed to the amount of heat stress of a standing human body inside a street canyon.

URBSIM is an advanced numerical model that includes most processes that are relevant to the urban environment. Despite the fact that the model is limited to 2D cases, the studies presented in this thesis have aided the understanding of the elementary processes that control urban air temperature, and the large amount of feedback processes and interactions between the different mechanisms in the surface energy balance.

Chapter 2

The study reported in Chapter 2 investigated the nighttime urban heat budget. It was shown that this budget is controlled by longwave radiation. For H/W=0.5, the longwave trapping effect (radiation emitted at one surface and absorbed at another) and the absorbed longwave radiation from the sky are of the same order of magnitude. With increasing H/W ratio, longwave trapping becomes the main source of energy to the urban energy budget. The contribution of conduction is fairly constant as a function of H/W ratio, and ranges from 15% of the absorbed radiation (H/W=0.0) to 10% (H/W=2.0). As a reference, for a flat terrain De Bruin and Holtslag (1982)

showed that the contribution of the conductive heat flux to the surface energy balance was about an order of magnitude smaller than that of the absorbed longwave radiation. The sensible heat flux results in a nearly uniform surface temperature over the canyon, but the magnitude of the sensible heat flux is small compared to the radiative contributions.

Chapter 3
If the daytime heat budget is considered, it was confirmed that the energy budget is controlled by solar radiation, where absorbed shortwave radiation is the main source of energy at the surface, followed by trapped longwave radiation. The radiative components are, however, decreasing with increasing building height, while the conductive heat flux is increasing.

The second objective of this study, was to investigate the relation between surface temperature, air temperature and mean radiant temperature. The link between surface temperature and mean radiant temperature can be made (at least from a quantitative point of view) relatively easy, since both are largely dependent on radiative fluxes. The link between surface temperature and air temperature is much harder to make. Air temperature inside the canyon is determined by a complex interplay between forced convection (which is a function of free stream wind speed) and natural convection (buoyancy forces).

Thirdly, the goal was to create insight in the processes that need to be taken into account in other simplified models. The used model takes all processes into account in high detail, where the influence of the user on the results has been minimised as much as possible. The down-side of this approach is that calculations are costly and time-consuming, and the same approach can't be extended to 3D environments due to the large computational requirements of the CFD model and the Monte-Carlo model, in which the number of emitted photons would increase drastically. For these simple building shapes, the Monte-Carlo model may be replaced by a much faster view-factor model.

Chapter 4
The effect of different albedo adaptation measures is studied in Chapter 4. Using a high albedo (white surface) is often advocated as a means of mitigating the urban heat island. This study showed that simply using a high albedo where possible might not lead to the desired results. Although air temperature is decreasing with increasing albedo, mean radiant temperature increases at a higher rate and therefore the apparent temperature (UTCI) increases. Different albedo adaptation measures were studied, where an albedo gradient on the vertical wall (high albedo at the bottom and low

albedo at the top) showed only a small increase in air temperature but the largest decrease in UTCI for an idealized 2D geometry. This adaptation measure outperforms a uniform low albedo when the UTCI is considered for H/W=1.0. However, the effect of changing the albedo on the UTCI remains small (up to 2°C) compared to shading effects (up to 12°C). It might therefore be more interesting to investigate artificial shading effects to reduce the pedestrian heat stress during the day.

Chapter 5

Comparisons between the large-scale urban parametrisation proposed by Kusaka et al. (2001), which is often used in the weather model WRF, and URBSIM showed that radiation is closely matched between the different models. The good agreement indicates that the actual 2D geometry is used in the computation of radiation within SLUCM, without 3D adaptations. The results for canyon wind speed and sensible heat flux deviated more in both models, which is most likely due to the 2D geometry that is applied in URBSIM. Although a 2D geometry is used in the parametrisation scheme (Kusaka et al., 2001), it represents a large 3D environment and the parametrisation scheme is tuned to obtain realistic results for such a 3D environment inside a single grid cell. The micro-scale model used the actual 2D geometry that is used in the parametrisation scheme. For the shortwave and longwave radiative components, the micro-scale model and parametrisation scheme agree well. For computation of the wind speed and the sensible heat flux, general trends are well captured although absolute values can differ by a large extent between both models. Future work could be the comparison of the fully coupled system, instead of the individual components in an idealized framework. A second step could be the direct coupling of the two models, in which URBSIM uses the large scale values from WRF as input, and provides detailed information on the urban geometry as output. This would remove the need of urban parametrisation schemes in WRF.

6.2 Future work

6.2.1 Numerical research

With URBSIM, many new research areas could be explored, either in 2D or 3D. Some possible studies are mentioned here.

When focussing on adaptation measures to counter the urban heat island, vegetation is often advocated. Steeneveld et al. (2011) showed that a large scale increase in vegetation of 10% inside the city can reduce the urban heat island effect by 0.6°C. However, the impact of vegetation on the urban microclimate is less often studied, where trees and bushes both affect air flow and

radiation. In addition to trees and bushes, the effect of green façades on the temperature in the city can be studied, which mainly influence the conductive heat flux and hence the indoor temperature.

The results in this thesis show that air temperature and pedestrian thermal comfort are only weakly related to one another. There is also the distinction between day & night and the indoor & outdoor environment. To study the influence of the outdoor environment on the indoor environment, it is recommended to implement a building energy model to the current model to 1) get accurate predictions for indoor temperatures and 2) to get a better representation of the conductive heat flux and heat storage in walls.

Using large H/W ratios in future city planning might be beneficial for reducing heat stress, but it can also trap exhaust gasses and deteriorate air quality. Therefore, the urban climate is a balance between heat stress and air quality. Recently, studies are performed which includes heating and pollutant dispersion for idealized 2D street canyons (Kang et al., 2008; Tong and Leung, 2012). These studies can be extended by considering reactive pollutants, where mainly the balance between NO-NO_2-O_3 is of interest, which is a photochemical process (Baker et al., 2004; Grawe et al., 2007; Kang et al., 2008; Kwak and Baik, 2012; Kwak et al., 2013). URBSIM can be used to couple the photovoltaic reactions to CFD including temperature effects. Currently, work is undergoing in this topic (Muilwijk et al., 2015, 2016)

6.2.2 Experimental research and observations

The importance of experimental research should not be underestimated. Despite the fact that this is recognized, detailed observational cases remain scarce for validating modelling results at urban micro-scales.

For air flow and pollutant concentrations, in-situ measurements (DePaul and Sheih, 1986; Biltoft, 2002) or wind tunnel measurements (Pavageau and Schatzmann, 1999; Hilderman and Chong, 2004) are available. A wide range of building geometries, inlet conditions and pollutant dispersion sources are used. Especially the MUST case from the Coanda Research and Development Corporation (Hilderman and Chong, 2004) is used to validate the current CFD model (ter Kuile, 2009; Chao, 2010; Busking, 2010; van der Houwen, 2012; de Wildt, 2012; Kenjeres and ter Kuile, 2013; Kenjeres et al., 2015). Inlet conditions are well defined and measurements of velocity and tracer gas concentrations are present for a wide range of building geometries in this data-set. These experiments allow detailed analysis on the accuracy of the CFD models and the different turbulence models that are used.

When heated surfaces are considered, there are measurements available for a single cube (Meinders et al., 1999; Richards et al., 2006), water tunnel experiments where heating is included by varying salinity (where salinity mimics the role of heat via its effect on the density) (Huizhi et al., 2003), wind tunnel experiments with a heated surface panel (Kovar-Panskus et al., 2002) or heated inlet air to create a stably stratified flow (Uehara et al., 2000). Although the aforementioned studies are very insightful, they are not ideal for validation purposes, since essential information is missing. For instance, inlet conditions are not exactly specified or measurement locations are not reported. This makes it difficult to validate a CFD model including buoyancy effects.

In addition to idealized experiments, measurements were conducted by Nunez and Oke (1977) on the urban micro-scale, where energy fluxes inside the urban canyon were measured. On the city scale, the Basel UrBan Boundary Layer Experiment BUBBLE (Rotach et al., 2005) is worth mentioning, which uses a year long observational network to study the urban environment. The BUCL (Burmingham Urban Climate Lab) experiment is ongoing at this moment (Chapman et al., 2014), in which temperature and rain are measured on a high spatial resolution. Besides these fixed point measurements, other measurement-strategies are possible. Steeneveld et al. (2011) used data from hobby meteorologists in the Netherlands to study the urban heat island effect in different cities of varying size. Heusinkveld et al. (2014) used bike traverse measurements to measure local air temperature, mean radiant temperature, humidity and wind speed in Rotterdam, and Overeem et al. (2013) are investigating the usage of cell-phone data (battery-temperature) to measure local air temperature. This would lead to an enormous data-set that could cover large parts of the country. Many new insights are gained from this data, and possible new research areas can be determined. The data can also be used to validate the conclusions from numerical models. However, it is impossible to control all parameters in a real life city, where changes are present due to for instance traffic flows inside the considered street canyon. To overcome these problems, one would like to control all environmental parameters, which can be done in (for instance) a heated wind-tunnel. By using a closed environment, all parameters are known and very detailed measurements can be conducted which allows validation of models on this scale.

6.2.3 Modelling

Lastly, there are numerical parts of URBSIM that can be improved, of which several are mentioned in each chapter. One important remark is

computational efficiency. With each additional physical mechanism added to URBSIM, computation time increases up to a point where it becomes an important issue. However, creating a program suited to run on a supercomputer takes time in itself. Since URBSIM was still in its developing stage, the main priority was to have a model that describes all relevant processes where long computation times are accepted. However, for future research it is highly recommended to develop a parallel version of the complete program. Work is currently ongoing to use multiple CPUs for the CFD calculation, and it can be worthwhile to use the GPU for the Monte-Carlo radiation model.

Bibliography

Aida, M., 1982: Urban albedo as a function of the urban structure — A model experiment. *Bound-Lay Meteorol*, **23**, 405–413.

Aida, M. and K. Gotoh, 1982: Urban albedo as a function of the urban structure — A two-dimensional numerical simulation. *Bound-Lay Meteorol*, **23**, 415–424.

Akbari, H., M. Pomerantz, and H. Taha, 2001: Cool surfaces and shade trees to reduce energy use and improve air quality in urban areas. *Sol Energy*, **70 (3)**, 295 – 310, urban Environment.

Albers, R. A. W., P. Bosch, B. Blocken, A. V. D. Dobbelsteen, L. V. Hove, and T. Spit, 2015: Overview of challenges and achievements in the Climate Proof Cities program. *Build Environ*, **83**, 1–10, Special Issue: Climate adaptation in cities.

Ali-Toudert, F. and H. Mayer, 2006: Numerical study on the effects of aspect ratio and orientation of an urban street canyon on outdoor thermal comfort in hot and dry climate. *Build Environ*, **41 (2)**, 94 – 108.

Arnfield, A. J., 2003: Two decades of urban climate research: a review of turbulence, exchanges of energy and water, and the urban heat island. *Int J Climatol*, **23 (1)**, 1–26.

Baccini, M., et al., 2008: Heat effects on Mortality in 15 European Cities. *Epidemiology*, **19 (5)**, 711–719.

Baik, J.-J., Y.-S. Kang, and J.-J. Kim, 2007: Modeling reactive pollutant dispersion in an urban street canyon. *Atmos Environ*, **41 (5)**, 934 – 949.

Baik, J.-J., Y.-H. Kim, and H.-Y. Chun, 2001: Dry and Moist Convection Forced by an Urban Heat Island. *J Appl Meteorol Climatol*, **40**, 1462–1475.

Baker, J., H. L. Walker, and X. Cai, 2004: A study of the dispersion and transport of reactive pollutants in and above street canyons-a large eddy simulation. *Atmos Environ*, **38 (39)**, 6883 – 6892.

Barlow, J., 2014: Progress in observing and modelling the urban boundary layer. *Urban Clim*, **10, Part 2 (0)**, 216 – 240, ICUC8: The 8th International Conference on Urban Climate and the 10th Symposium on

the Urban Environment.

Barlow, J., C. Hails, S. Lane, and C. Wood, 2015: Observations of urban boundary layer structure during a strong urban heat island event. *Environmental Fluid Mechanics*, **15 (2)**, 373–398.

Biltoft, C., 2002: Customer report for mock urban test setting test. Tech. rep., Meteorology and Obscurants division, West Desert Test Center, US. Army Dugway Proving Ground.

Bohnenstengel, S., K. Schlünzen, and D. Grawe, 2004: Influence of thermal effects on street canyon circulations. *Meteorol Z*, **13 (5)**, 381–386.

Bretz, S., H. Akbari, and A. Rosenfeld, 1998: Practical issues for using solar-reflective materials to mitigate urban heat islands. *Atmos Environ*, **32 (1)**, 95 – 101, conference on the Benefits of the Urban Forest.

Bröde, P., 2005: Universal temperature climate index documentation. www.utci.org/utci_doku.php.

Bröde, P., D. Fiala, K. Bazejczyk, I. Holmer, G. Jendritzky, B. Kampmann, B. Tinz, and G. Havenith, 2012: Deriving the operational procedure for the Universal Thermal Climate Index (UTCI). *Int J Biometeor*, **56 (3)**, 481–494.

Brown, G. and M. Delay, 2001: *Sun, Wind and Light: Architectural Design Strategies*. John Wiley and Sons, New York.

Bruse, M., 1999: Entwicklung des prognostischen numerischen Modells ENVI-met zur Simulation der Wind-, Temperatur- und Feuchteverteiling in Staddtischen Strukturen. Ph.D. thesis, University of Bochum.

Busking, T., 2010: Numerical Studies of Transient Effects in Turbulent Dispersion of Pollutants in Simplified Urban Areas at Laboratory Scale. M.S. thesis, Delft University of Technology.

Chao, C. L., 2010: Numerical Analysis of Turbulent Dispersion of Pollutants in Simplified Urban Areas at Laboratory Scale. M.S. thesis, Delft University of Technology.

Chapman, L., C. Muller, D. Young, E. Warren, C. Grimmond, X. Cai, and J. Ferranti, 2014: The Birmingham Urban Climate Laboratory: An open meteorological testbed and challenges of the smart city. *B Am Meteorol Soc*, under review.

Chen, F., et al., 2011: The integrated wrf/urban modelling system: development, evaluation, and applications to urban environmental problems. *Int J Climatol*, **31 (2)**, 273–288.

Cheng, V., E. Ng, and B. Givoni, 2005: Effect of envelope colour and thermal mass on indoor temperatures in hot humid climate. *Sol Energy*, **78 (4)**, 528 – 534.

Conrads, L., 1975: Observations of metereological urban effects. The heat

island of Utrecht. Ph.D. thesis, University of Utrecht.

Coronel, J. and S. Álvarez, 2001: Experimental work and analysis of confined urban spaces. *Sol Energy*, **70 (3)**, 263 – 273.

De Bruin, H. A. R. and A. A. M. Holtslag, 1982: A simple parameterization of the surface fluxes of sensible and latent heat during daytime compared with the Penman-Monteith concept. *J Appl Meteorol*, **21**, 1610–1621.

de Roode, S. R., H. J. J. Jonker, B. J. H. van de Wiel, V. Vertregt, and V. Perrin, 2017: A diagnosis of excessive mixing in smagorinsky subfilter-scale turbulent kinetic energy models. *Journal of the Atmospheric Sciences*, **74 (5)**, 1495–1511.

de Wildt, S., 2012: Capturing Transient Effects in Turbulent Flows with Passive Scalars over Urban Areas with Hybrid LES/T-RANS Approaches. M.S. thesis, Delft University of Technology.

DePaul, F. T. and C. M. Sheih, 1986: Measurements of wind velocities in a street canyon. *Atmos Environ*, **20 (3)**, 455 – 459.

Draxler, R. R., 1986: Simulated and observed influence of the nocturnal urban heat island on the local wind field. *J Appl Meteorol Climatol*, **25 (8)**, 1125–1133.

Durbin, P. A., 1996: On the k-ϵ stagnation point anomaly. *Int J Heat Fluid Fl*, **17**, 89–90.

Erell, E., D. Pearlmutter, D. Boneh, and P. B. Kutiel, 2014: Effect of high-albedo materials on pedestrian heat stress in urban street canyons. *Urban Climate*, **10, part 2**, 367–386, iCUC8: The 8th International Conference on Urban Climate and the 10th Symposium on the Urban Environment".

Erell, E. and T. Williamson, 2006: Simulating air temperature in an urban street canyon in all weather conditions using measured data at a reference meteorological station. *Int J Climatol*, **26 (12)**, 1671–1694.

European Environment Agency, 2008: *Heat and Health*.

Fiala, D., G. Havenith, P. Bröde, B. Kampmann, and G. Jendritzky, 2012: UTCI-Fiala multi-node model of human heat transfer and temperature regulation. *Int J Biometeor*, **56 (3)**, 429–441.

Fortuniak, K., 2008: Numerical estimation of the effective albedo of an urban canyon. *Theor Appl Climatol*, **91**, 245–258.

Garratt, J., 1992: *The atmospheric boundary layer*. Cambridge University Press.

Giovannini, L., D. Zardi, and M. de Franceschi, 2013: Characterization of the thermal structure inside an urban canyon: field measurements and validation of a simple model. *J Appl Meteorol Climatol*, **52**, 64–81.

Golden, J. S., 2004: The Built Environment Induced Urban Heat Island Effect in Rapidly Urbanizing Arid Regions - A Sustainable Urban

Engineering Complexity. *Environm Sci*, **1**, 321–349.

Grachev, A. A., E. L. Andreas, C. W. Fairall, P. S. Guest, and P. O. G. Persson, 2007: On the turbulent Prandtl number in the stable atmospheric boundary layer. *Bound-Lay Meteorol*, **125 (2)**, 329–341.

Grawe, D., X.-M. Cai, and R. M. Harrison, 2007: Large eddy simulation of shading effects on NO2 and O3 concentrations within an idealised street canyon. *Atmos Environ*, **41 (34)**, 7304 – 7314.

Grimmond, C. S. B., 2007: Urbanization and global environmental change: local effects of urban warming. *Geogr J*, **173 (1)**, 83–88.

Grimmond, C. S. B., et al., 2010: The International Urban Energy Balance Models Comparison Project: First Results from Phase 1. *J Appl Meteorol Climatol*, **49**, 1268–1292.

Grimmond, C. S. B., et al., 2011: Initial results from phase 2 of the international urban energy balance model comparison. *Int J Climatol*, **31 (2)**, 244–272.

Hertel, D. and U. Schlink, 2019: How to convert urban energy balance into contributions to urban excess temperatures? *MethodsX*, **6**, 132 – 142.

Heusinkveld, B. G., G. J. Steeneveld, L. W. A. van Hove, C. M. J. Jacobs, and A. A. M. Holtslag, 2014: Spatial variability of the rotterdam urban heat island as influenced by urban land use. *J Geophys Res-Atmos*, **119 (2)**, 677–692.

Hilderman, T. and R. Chong, 2004: A laboratory study of momentum and passive scalar transport and diffusion within and above a model urban canopy - final report. Tech. rep., Coanda Research and Development Corporation, Burnaby.

Höppe, P., 1999: The physiological equivalent temperature: a universal index for the biometeorological assessment of the thermal environment. *Int J Biometeor*, **43**, 71–75.

Howard, L., 1833: *The Climante Of London, Volume I-III*. London.

Huizhi, L., L. Bin, Z. Fengrong, Z. Boyin, and S. Jianguo, 2003: A Laboratory model for the flow in urban street canyons induced by bottom heating. *Adv Atmos Sci*, **20**, 554–564.

IPCC, 2013: *Summary for Policy makers. Climate Change 2013: The physical Science Basis. Contribution of Working Group 1 to the Firth Assessment Report on the Intergovernmental Panel on Climate Change*. Cambridge University Press, Cambridge, United Kingdom and New York, NY, USA.

Iqbal, M., 1983: *An Introduction To Solar Radiation*. Academic Press.

Jendritzky, G., R. de Dear, and G. Havenith, 2012: UTCI — Why another thermal index? *Int J Biometeor*, **56 (3)**, 421–428.

Kang, Y.-S., J.-J. Baik, and J.-J. Kim, 2008: Further studies of flow and reactive pollutant dispersion in a street canyon with bottom heating. *Atmos Environ*, **42 (20)**, 4964 – 4975.

Kasten, F., 1996: The Linke turbidity factor based on improved values of the integral Rayleigh optical thickness. *Sol Energy*, **56 (3)**, 239 – 244.

Kenjeres, S., S. de Wildt, and T. Busking, 2015: Capturing transient effects in turbulent flows over complex urban areas with passive pollutants. *Int J Heat Fluid Fl*, **51**, 120–137.

Kenjeres, S. and K. Hanjalic, 1999: Transient analysis of Rayleigh-Benard convection with a RANS model. *Int J Heat Fluid Fl*, **20 (3)**, 329 – 340.

Kenjeres, S. and K. Hanjalic, 2006: LES, T-RANS and hybrid simulations of thermal convection at high Ra numbers. *Int J Heat Fluid Fl*, **27 (5)**, 800 – 810.

Kenjeres, S. and K. Hanjalic, 2009: Tackling complex turbulent flows with transient RANS. *Fluid Dyn Res*, **41 (1)**, 1–32.

Kenjeres, S. and B. ter Kuile, 2013: Modelling and simulations of turbulent flows in urban areas with vegetation. *J Wind Eng Ind Aerod*, **123, Part A (0)**, 43 – 55.

Kim, J.-J. and J.-J. Baik, 2001: Urban street-canyon flows with bottom heating. *Atmos Environ*, **35 (20)**, 3395 – 3404.

Kim, Y.-H. and J.-J. Baik, 2004: Daily maximum urban heat island intensity in large cities of Korea. *Theor Appl Climatol*, **79 (3-4)**, 151–164.

Kleerekoper, L., A. van den Dobbelsteen, G. Hordijk, M. van Dorst, and C. Martin, 2015: Climate adaptation strategies: achieving insight in microclimate effects of redevelopment options. *Smart and Sustainable Built Environment*, **4 (1)**, 110–136.

Klysik, K. and K. Fortuniak, 1999: Temporal and spatial characteristics of the urban heat island of Lodz, Poland. *Atmos Environ*, **33 (24)**, 3885–3895.

Kovar-Panskus, A., L. Moulinneuf, E. Savory, A. Abdelqari, J.-F. Sini, J.-M. Rosant, A. Robins, and N. Toy, 2002: A Wind Tunnel Investigation of the Influence of Solar-Induced Wall-Heating on the Flow Regime within a Simulated Urban Street Canyon. *Water, Air, & Soil Pollution: Focus*, **2**, 555–571.

Krayenhoff, E. and J. Voogt, 2007: A microscale three-dimensional urban energy balance model for studying surface temperatures. *Bound-Lay Meteorol*, **123**, 433–461.

Krayenhoff, J. A. V., E. Scott, 2010: Impacts of urban albedo increase on local air temperature at daily–annual time scales: model results and synthesis of previous work. *J Appl Meteorol Climatol*, **49**, 1634–1648.

Kusaka, H., H. Kondo, Y. Kikegawa, and F. Kimura, 2001: A simple single-layer urban canopy model for atmospheric models: Comparison with multi-layer and slab models. *Bound-Lay Meteorol*, **101 (3)**, 329–358.

Kwak, K.-H. and J.-J. Baik, 2012: A CFD modeling study of the impacts of NOx and VOC emissions on reactive pollutant dispersion in and above a street canyon. *Atmos Environ*, **46 (0)**, 71 – 80.

Kwak, K.-H., J.-J. Baik, and K.-Y. Lee, 2013: Dispersion and photochemical evolution of reactive pollutants in street canyons. *Atmos Environ*, **70 (0)**, 98 – 107.

Launder, B. and D. Spalding, 1974: The numerical computation of turbulent flows. *Comput Method Appl M*, **3 (2)**, 269 – 289.

Li, D., 2019: Turbulent prandtl number in the atmospheric boundary layer - where are we now? *Atmospheric Research*, **216**, 86 – 105.

Lindberg, F., B. Holmer, and S. Thorsson, 2008: SOLWEIG 1.0 – Modelling spatial variations of 3D radiant fluxes and mean radiant temperature in complex urban settings. *Int J Biometeor*, **52**, 697–713.

Liu, Y., F. Chen, T. Warner, and J. Basara, 2006: Verification of a mesoscale data-assimilation and forecasting system for the Oklahoma city area during the Joint Urban 2003 Field Project. *J Appl Meteorol*, **45**, 912–929.

Madronich, S., 1987: Photodissociation in the atmosphere: 1. Actinic flux and the effects of ground reflections and clouds. *J Geophys Res-Atmos*, **92 (D8)**, 9740–9752.

Magnusson, S., A. Dallman, D. Entekhabi, R. Britter, H. Fernando, and L. Norford, 2014: On thermally forced flows in urban street canyons. *Env Fluid Mech*, **14**, 1–15.

Marciotto, E. R., A. P. Oliveira, and S. R. Hanna, 2010: Modeling study of the aspect ratio influence on urban canopy energy fluxes with a modified wall-canyon energy budget scheme. *Build Environ*, **45 (11)**, 2497 – 2505.

Maronga, B., et al., 2019: Development of a new urban climate model based on the model palm – project overview, planned work, and first achievements. *Meteorologische Zeitschrift*.

Martilli, A., A. Clappier, and M. Rotach, 2002: An urban surface exchange parameterisation for mesoscale models. *Bound-Lay Meteorol*, **104 (2)**, 261–304.

Masson, V., 2000: A physically-based scheme for the urban energy budget in atmospheric models. *Bound-Lay Meteorol*, **94**, 357–397.

Masson, V., 2006: Urban surface modeling and the meso-scale impact of cities. *Theor Appl Climatol*, **84 (1-3)**, 35–45.

Matzarakis, A., 2000: *Estimation and calculation of the mean radiant temperature within the urban structure. Manual to RayMan.* University

of Freiburg, Germany.

McMichael, A., R. Woodruff, and S. Hales, 2006: Climate change and human health: present and future risks. *Lancet*, **368**, 859–869.

Meinders, E. R., K. Hanjalic, and R. J. Martinuzzi, 1999: Experimental Study of the Local Convection Heat Transfer From a Wall-Mounted Cube in Turbulent Channel Flow. *J Heat Tranf*, **121 (3)**, 564–573.

Memon, R. A., D. Y. Leung, and C.-H. Liu, 2010: Effects of building aspect ratio and wind speed on air temperatures in urban-like street canyons. *Build Environ*, **45 (1)**, 176 – 188, international Symposium on the Interaction between Human and Building Environment Special Issue Section.

Mills, A., 1999: *Basic Heat & Mass Transfer, 2nd edition*. Prentice Hall, Inc.

Monteiro, A., V. Carvalho, and C. Sousa, 2012: Excess mortality and morbidity during July 2006 heat wave in Porto, Portugal - T mrt efficiency to anticipate negative effects on health. *Proceedings of the 8th international conference on urban climates, Dublin, Ireland, 6–10 August*.

Muilwijk, C., P. Schrijvers, and S. Kenjeres, 2015: On modelling and simulations of photochemical smog formation in simplified and complex urban areas. *Proceedings of 8th International Symposium on Turbulence, Heat and Mass*, 727–730.

Muilwijk, C., P. Schrijvers, S. Wuerz, and S. Kenjereš, 2016: Simulations of photochemical smog formation in complex urban areas. *Atmospheric Environment*, **147**, 470 – 484.

New York High Performance Infrastructure Guidelines, 2005: Http://www.nyc.gov/html/ddc/downloads/pdf/hpig.pdf.

Nunez, M. and T. R. Oke, 1977: Energy Balance of an Urban Canyon. *J Appl Meteorol*, **16 (1)**, 11 – 19.

Offerle, B., I. Eliasson, C. S. B. Grimmond, and B. Holmer, 2007: Surface heating in relation to air temperature, wind and turbulence in an urban street canyon. *Bound-Lay Meteorol*, **122 (2)**, 273–292.

Oke, T., 1995: The heat island of the urban boundary layer: Characteristics, causes and effects. *NATO ASI Series e Applied Sciences-Advanced Study Institute*, **277**, 81–108.

Oke, T. R., 1981: Canyon geometry and the nocturnal urban heat island: Comparison of scale model and field observations. *J Climatol*, **1 (3)**, 237–254.

Oke, T. R., 1982: The energetic basis of the urban heat island. *Q J Roy Meteorol Soc*, **108 (455)**, 1–24.

Oke, T. R., 1988: Street design and urban canopy layer climate. *Energ Buildings*, **11 (1-3)**, 103 – 113.

Overeem, A., J. C. R. Robinson, H. Leijnse, G. J. Steeneveld, B. K. P. Horn, and R. Uijlenhoet, 2013: Crowdsourcing urban air temperatures from smartphone batterytemperatures. *Geophys Res Lett*, **40 (15)**, 4081–4085.

Pavageau, M. and M. Schatzmann, 1999: Wind tunnel measurements of concentration fluctuations in an urban street canyon. *Atmos Environ*, **33 (24-25)**, 3961 – 3971.

Pearlmutter, D., P. Berliner, and E. Shaviv, 2007: Integrated modeling of pedestrian energy exchange and thermal comfort in urban street canyons. *Build Environ*, **42 (6)**, 2396 – 2409.

Philadelphia High Performance Building Renovation Guidelines, 2004: Http://www.phila.gov/pdfs/PhiladelphiaGreenGuidelines.pdf.

Prata, A. J., 1996: A new long-wave formula for estimating downward clear-sky radiation at the surface. *Q J Roy Meteorol Soc*, **122 (533)**, 1127–1151.

Richards, K., M. Schatzmann, and B. Leitl, 2006: Wind tunnel experiments modelling the thermal effects within the vicinity of a single block building with leeward wall heating. *J Wind Eng Ind Aerod*, **94 (8)**, 621 – 636.

Rizwam, A. M., L. Y. Dennis, and C. Liu, 2008: A review on the generation, determination and mitigation of urban heat island. *J Environ Sci*, **20 (1)**, 120 – 128.

Robine, J., S. Cheung, S. L. Roy, H. V. Oyen, C. Griffiths, J. Michel, and F. Hermann, 2008: Deat toll exceeded 70,000 in Europe during the summer in 2003. *Comptes Rendus Biologies*, **331**, 171–178.

Robitu, M., M. Musy, C. Inard, and D. Groleau, 2006: Modeling the influence of vegetation and water pond on urban microclimate. *Sol Energy*, **80 (4)**, 435 – 447.

Ronda, R., G. Steeneveld, L. van Hove, and A. Holtslag, 2012: Anthropogenic heat release and Urban Heat Island effects in Rotterdam. *Proceedings of the ICUC8: The 8th International Conference on Urban Climate and the 10th Symposium on the Urban Environment.*

Roodenburg, J., 1983: Adaptation of rural minimum temperature forecasts to an urban environment. *Arch Meteor Geophy B*, **32 (4)**, 395–401.

Rotach, M. W., et al., 2005: BUBBLE: an urban boundary layer meteorology project. *Theor Appl Climatol*, **81 (3-4)**, 231–261.

Ryu, Y.-H. and J.-J. Baik, 2012: Quantitative analysis of factors contributing to urban heat island intensity. *J Appl Meteorol Climatol*, **51**, 842 – 854.

Sakakibara, Y., 1996: A numerical study of the effect of urban geometry upon the surface energy budget. *Atmos Environ*, **30 (3)**, 487 – 496, conference on the Urban Thermal Environment Studies in Tohwa.

Santamouris, M., N. Gaitani, A. Spanou, M. Saliari, K. Giannopoulou, K. Vasilakopoulou, and T. Kardomateas, 2012: Using cool paving materials

to improve microclimate of urban areas – design realization and results of the flisvos project. *Build Environ*, **53 (0)**, 128 – 136.

Santamouris, M., N. Papanikolaou, I. Koronakis, I. Livada, and D. Asimakopoulos, 1999: Thermal and air flow characteristics in a deep pedestrian canyon under hot weather conditions. *Atmos Environ*, **33 (27)**, 4503 – 4521.

Santiago, J., A. Martilli, and F. Martín, 2007: CFD simulation of airflow over a regular array of cubes. Part I: Three-dimensional simulation of the flow and validation with wind-tunnel measurements. *Bound-Lay Meteorol*, **122 (3)**, 609–634.

Schrijvers, P., H. Jonker, S. de Roode, and S. Kenjeres, 2020a: On the daytime micro-climatic conditions inside an idealized 2d urban canyon. *Build Environ*, **167**, 106 427.

Schrijvers, P., H. Jonker, S. Roode, and S. Kenjeres, 2020b: Corrigendum to "breakdown of the night time urban heat island energy budget" [build. environ. 83 (2015) 50–64]. *Build Environ*, **174**, 106 767.

Schrijvers, P. J. C., H. J. J. Jonker, S. Kenjeres, and S. R. de Roode, 2015: Breakdown of the night time urban heat island energy budget. *Build Environ*, **83**, 50–64, Special Issue: Climate adaptation in cities.

Schrijvers, P. J. C., H. J. J. Jonker, S. Kenjeres, and S. R. de Roode, 2016: The effect of using a high-albedo material on the Universal Temperature Climate Index within a street canyon. *Urban Climate*, **17**, 284–303.

Silva, H. R., R. Bhardwaj, P. E. Phelan, J. S. Golden, and S. Grossman-Clarke, 2009: Development of a zero-dimensional mesoscale thermal model for urban climate. *J Appl Meteorol Climatol*, **48**, 567–668.

Simpson, J. and E. McPherson, 1997: The effects of roof albedo modification on cooling loads of scale model residences in tucson, arizona. *Energ Buildings*, **25 (2)**, 127 – 137.

Sini, J.-F., S. Anquetin, and P. G. Mestayer, 1996: Pollutant dispersion and thermal effects in urban street canyons. *Atmos Environ*, **30 (15)**, 2659 – 2677.

Skamarock, W. C., et al., 2005: A description of the advanced research wrf vesion 3. Tech. rep., National Center For Atmospheric Research, Boulder.

Skartveit, A., J. A. Olseth, and M. E. Tuft, 1998: An hourly diffuse fraction model with correction for variability and surface albedo. *Sol Energy*, **63 (3)**, 173 – 183.

Soltani, A. and E. Sharifi, 2017: Daily variation of urban heat island effect and its correlations to urban greenery: A case study of Adelaide. *Frontiers of Architectural Research*, **6 (4)**, 529–538.

Steeneveld, G. J., S. Koopmans, B. G. Heusinkveld, L. W. A. van Hove, and

A. A. M. Holtslag, 2011: Quantifying urban heat island effects and human comfort for cities of variable size and urban morphology in the netherlands. *J Geophys Res-Atmos*, **116 (D20)**.

Suter, I. L., 2019: Simulating the impact of blue-green infrastructure on the microclimate of urban areas. Ph.D. thesis, Imperial College London.

Swaid, H., 1993: The role of radiative-convective interaction in creating the microclimate of urban street canyons. *Bound-Lay Meteorol*, **64 (3)**, 231–259.

Synnefa, A., A. Dandou, M. Santamouris, M. Tombrou, and N. Soulakellis, 2008: On the use of cool materials as a heat island mitigation strategy. *J Appl Meteorol Climatol*, **47**, 2846–2856.

Taha, H., 1997: Urban climates and heat islands: albedo, evapotranspiration, and anthropogenic heat. *Energ Buildings*, **25 (2)**, 99 – 103.

Taha, H., H. Akbari, A. Rosenfeld, and J. Huang, 1988: Residential cooling loads and the urban heat island—the effects of albedo. *Build Environ*, **23 (4)**, 271 – 283.

Taha, H., S. Konopacki, and S. Gabersek, 1999: Impacts of large-scale surface modifications on meteorological conditions and energy use: A 10-region modeling study. *Theor Appl Climatol*, **62 (3-4)**, 175–185.

Taleghani, M., L. Kleerekoper, M. Tenpierik, and A. van den Dobbelsteen, 2015: Outdoor thermal comfort within five different urban forms in the Netherlands. *Build Environ*, **83**, 65 – 78, special Issue: Climate adaptation in cities.

ter Kuile, B., 2009: Numerical simulations of pollutants in urban areas with vegetation using a modified k-ϵ model. M.S. thesis, Delft University of Technology.

Theeuwes, N. E., G. J. Steeneveld, R. J. Ronda, B. G. Heusinkveld, L. W. A. van Hove, and A. A. M. Holtslag, 2014: Seasonal dependence of the urban heat island on the street canyon aspect ratio. *Q J Roy Meteorol Soc*, **140**, 2197–2210.

Theeuwes, N. E., G.-J. Steeneveld, R. J. Ronda, and A. A. M. Holtslag, 2017: A diagnostic equation for the daily maximum urban heat island effect for cities in northwestern europe. *Int J Climatol*, **47 (1)**, 443–454.

Thorsson, S., F. Lindberg, I. Eliasson, and B. Holmer, 2007: Different methods for estimating the mean radiant temperature in an outdoor urban setting. *Int J Climatol*, **27 (14)**, 1983–1993.

Thorsson, S., J. Rocklöv, J. Konarska, F. Lindberg, B. Holmer, B. Dousset, and D. Rayner, 2014: Mean radiant temperature – a predictor of heat related mortality. *Urban Clim*, **10, Part 2 (0)**, 332 – 345, iCUC8: The 8th International Conference on Urban Climate and the 10th Symposium

on the Urban Environment.

Tomas, J., M. Pourquie, and H. Jonker, 2015: The influence of an obstacle on flow and pollutant dispersion in neutral and stable boundary layers. *Atmos Environ*, **113 (0)**, 236 – 246.

Tomas, J. M., M. J. B. M. Pourquie, and H. J. J. Jonker, 2016: Stable stratification effects on flow and pollutant dispersion in boundary layers entering a generic urban environment. *Bound-Lay Meteorol*, **159 (2)**, 221–239.

Tominaga, Y., R. Yoshie, A. Mochida, H. Kataoka, K. Haricot, and T. Nozu, 2005: Cross comparison of CFD prediction for wind environment at pedestrian level around buildings (Part 2). *Proceedings of the Sixth Asia-Pacific Conference on Wind Engineering (APCWE-VI)*, 2661–2670.

Tong, N. Y. and D. Y. Leung, 2012: Effects of building aspect ratio, diurnal heating scenario, and wind speed on reactive pollutant dispersion in urban street canyons. *J Environ Sci*, **24 (12)**, 2091 – 2103.

Toparlar, Y., B. Blocken, B. Maiheu, and G. van Heijst, 2017: A review on the cfd analysis of urban microclimate. *Renewable and Sustainable Energy Reviews*, **80**, 1613 – 1640.

Uehara, K., S. Murakami, S. Oikawa, and S. Wakamatsu, 2000: Wind tunnel experiments on how thermal stratification affects flow in and above urban street canyons. *Atmos Environ*, **34 (10)**, 1553 – 1562.

van der Houwen, M., 2012: Numerical Analysis of Turbulent Dispersion of Reactive Pollutants in Simplified Urban Areas. M.S. thesis, Delft University of Technology.

van Heerwaarden, C. C., J. Vilà-Guerau de Arellano, A. F. Moene, and A. A. M. Holtslag, 2009: Interactions between dry-air entrainment, surface evaporation and convective boundary-layer development. *Q J Roy Meteorol Soc*, **135 (642)**, 1277–1291.

Vandentorren, S., F. Suzan, S. Medina, M. Pascal, A. Maulpoix, J.-C. Cohen, and M. Ledrans, 2001: Mortality in 13 French cities during the August 2003 heat wave. *Am J Public Health*, **94 (9)**, 1518–1520.

Versteeg, H. and W. Malalasekera, 1995: *An Introduction to computational fluid dynamics*. Harlow: Pearson Education Limited.

Wallace, J. M. and P. V. Hobbs, 2006: *Atmospheric Science, an Introduction Survey*. Academic Press.

Whitman, S., G. Good, E. Donoghue, N. Benbow, W. Shou, and S. Mou, 1997: Mortality in Chicago attributed to the July 1995 heat wave. *Am J Public Health*, **87 (9)**, 1515–1518.

World Health Organisation, 2014: .

Xie, X., Z. Huang, J. Wang, and Z. Xie, 2005: Thermal effects on vehicle

emission dispersion in an urban street canyon. *Transport Res D-Tr E*, **10 (3)**, 197 – 212.

Yaghoobian, N. and J. Kleissl, 2012: Effect of reflective pavements on building energy use. *Urban Climate*, **2 (0)**, 25 – 42.

Acknowledgements

After nearly 10 years, I can safely state that my time as a PhD student was quite a roller-coaster. I remember my first thought when starting with this (supposedly) four-year project: that is a lot of time for just one topic. As it turns out, it isn't, it really isn't. My time as a PhD in Delft flew by more quickly than I could ever imagine, and the combination of working at MARIN and finishing my PhD pushed me to my limits. But as my proposition states: finishing a PhD is about perseverance and if you are to stubborn to stop, you will reach the finish at some point. This has not been the easiest task, but I am grateful for the opportunity and learned a great deal. Not only on a complex topic, but also about myself.

This book would not have been possible without a lot of people.

First of all, my supervisors. Harm has a 'magic touch' where he is able to find the weak spot in your argumentation in a second. Annoyingly enough, that always seems to be a rather essential point. He loves the whiteboard, where for some reason every discussion ends. A habit that I have taken over. Next to that, he has the ability to dig into the details when needed, but without losing sight of the overall picture.

Next up is Sasa, my hero of CFD modelling. When finishing my masters project, I wanted to learn more on CFD models. With Sasa, you can't think of a better person to do so. We have worked on RANS models, hybrid RANS-LES models, buoyancy forces and chemical reactions together and with a lot of students, which was always inspiring.

Stephan is probably one of the most enthusiastic persons I know, where his passion for physics is only matched by his passion for cycling. His drive always pushed me forward. He is also the person who provided me with the majority of the feedback on my papers, for which I cannot thank him enough. Although it can be annoying to get a red piece of paper back with comments, they always make sense and help the paper and this thesis forward.

These three people where my daily supervisors. Without them, I would probably still be in the recognizing phases of my PhD. They helped me where ever possible, provided positive feedback when possible and kicked my butt when needed. I cannot thank them enough.

Then we go down the hierarchical line and come to my fellow PhD students in Delft. Steef, Johan, Jerome & Vincent, I really enjoyed working with you. I have learned many new things on programming, science and off course bad jokes. I liked all our 'discussions' on the French, running, (bad taste in) music or stupid science stuff. It was a great pleasure to work with you. The same holds for all other PhD's and master students in the Atmospheric Physics group.

Than a couple off words on the people from the Climate Proof Cities project. Although the consortium sometimes felt like an obligatory party that you have to attend, but at the end of the party it turned our I really enjoyed myself. The meetings at city councils, the yearly event where you had the change to discuss and catch up with everybody or the summer schools in Manchester and Utrecht; I enjoyed them all.

Off course I have to thank Rob, Tim & Bart, who helped me get rid of some (or at times the majority) of my spare time by taking golf lessons, go to the Arden forest for mountain bike weekends or just have drinks, dinners and hang out. Thanks to you, work issues where easily forgotten (at least for that night/weekend).

Thanks to Sander and Melchior, my concert buddies, I was able to visit a lot of good concerts and some really crappy ones. Our discussions on music, albums and concerts really helped my put my mind to other things than my PhD.

Then I simply put the rest of the people on a large pile: all my friends and family, who have helped me tremendously throughout this project. My attempts to explain to you what I was doing created new insights and helped me move forward.

And last but not least, I have to thank Jenny. This has not been the easiest of things, but while we were in Delft, you kept me motivated and kicked my butt when needed. While working at MARIN, you made sure that I would not bury myself in work. I could not have done this without you.

About the author

September 21, 1985	Born in Buren
1997-2002	R.K. Marianum, Groenlo
2002-2006	BSc Automotive Engineering HAN University of Automotive Engineering
2006	BSc thesis "Onderzoek naar het weggedrag van een Donkervoort" in cooperation with Donkervoort Automobielen BV
2006-2010	MSc Mechanical Engineering Delft University of Technology
2009-2010	MSc thesis "Optizizing towards minimal drag of the aerodynamic package of a truck" in cooperation with Ephicas
2010-2014	PhD project, "Urban climate at street scale: analysis and adaptation", Delft University of Technology
2014-present	Project Manager at MARIN

List of publications

Schrijvers P.J.C., H.J.J. Jonker, S. Kenjereš & S.R. de Roode, 2012: "Simulations of the urban climate at micro-scale". *Proceedings of 8th International Conference on Urban Climates*

Schrijvers P.J.C., H.J.J. Jonker, S. Kenjereš & S.R. de Roode, 2015: "Breakdown of the night time urban heat island energy budget". *Building and Environment* **83** 50-64, Special issue: Climate adaptation in cities

Muilwijk C., P.J.C. Schrijvers & S. Kenjereš 2015: "On modelling and simulations of photochemical smog formation in simplified and complex urban areas. *Proceedings of 8th International Symposium on Turbulence, Heat and Mass*

Schrijvers P.J.C., H.J.J. Jonker, S. Kenjereš & S.R. de Roode, 2016: "The effect of using a high-albedo material on the Universal Temperature Climate Index". *Urban Climate* **17** 284-303

Muilwijk C., P.J.C. Schrijvers, S. Wuerz & S. Kenjereš 2016: "Simulations of photochemical smog formation in complex urban areas. *Atmospheric Environment* **147** 470-484

Schrijvers P.J.C., H.J.J. Jonker, S. Kenjereš & S.R. de Roode, 2019: "On the daytime micro-climatic conditions inside an idealized 2D urban canyon". *Building and Environment* **167**